



# THÈSE

En vue de l'obtention du

## DOCTORAT DE L'UNIVERSITÉ DE TOULOUSE

Délivré par : *l'Institut National Polytechnique de Toulouse (INP Toulouse)*

---

---

Présentée et soutenue le 05/11/2018 par :

**ROMAIN BIZZARI**

### Modélisation aérodynamique et thermique des plaques multiperforées en LES

---

---

#### JURY

MME F. BATAILLE	Professeur (PROMES)	Rapporteur
M. T. ARTS	Professeur (VKI)	Rapporteur
MME E. DORIGNAC	Professeur (Pprime)	Examineur
M. P. BRUEL	CR (CNRS)	Examineur
MME M. BRAZA	DR (IMFT)	Examineur
M. F. NICOUD	Professeur (IMAG)	Examineur
M. T. POINSOT	DR (IMFT)	Directeur
M. A. DAUPTAIN	Dr. Ing. (CERFACS)	Co-directeur
M. S. RICHARD	Dr. Ing. (SHE)	Invité

---

**École doctorale et spécialité :**

*MEGEP : Dynamique des fluides*

**Unité de Recherche :**

*CERFACS (UMR 5318)*

**Directeur(s) de Thèse :**

*T. Poinsot et A. Dauplain*

**Rapporteurs :**

*Mme BATAILLE Françoise et M. ARTS Tony*



# Abstract

Numerical simulation is progressively taking importance in the design of an aeronautical engine. However, concerning the particular case of cooling devices, the high number of sub-millimetric cooling holes is an obstacle for computational simulations. A classical approach goes through the modelling of the effusion cooling by homogenisation. It allows to simulate a full combustor but fails in representing the jet penetration and mixing. A new approach named thickened-hole model was developed during this thesis to overcome this issue. A work on improving the mesh resolution on key areas thanks to an automatic adaptive method is also presented, leading to a clear breakthrough.

In parallel, as the flame tube temperature is a cornerstone for the combustor durability, a low-cost approach is proposed to predict it. To meet the time-constraints of design, it is based on thermal modelling instead of a direct thermal resolution.

**Keywords :** Effusion cooling, Conjugate Heat Transfer, Aerodynamics, Large Eddy Simulation

# Résumé

Dans les chambres de combustion aéronautiques, le refroidissement par micro-perçage est la technique privilégiée pour protéger les parois contre les gaz chauds. L'air frais provenant du contournement traverse des milliers de perforations inclinées et forme des micro-jets. Ces derniers coalescent en un film qui protège les parois du tube à flamme. Avec les moyens informatiques actuels, effectuer une simulation aux grandes échelles d'un moteur réel est impossible. En effet, le nombre de micro-trous est beaucoup trop important pour permettre une résolution détaillée de chacun. Des modèles numériques sont donc nécessaires. Le modèle homogène, développé en 2008, permet de simuler des plaques multiperforées avec des maillages dont la résolution est supérieure à celle du trou. Il ne permet cependant pas de représenter la pénétration ni le mélange des jets avec les gaz chauds. Pour remédier à cela, une approche hétérogène, appelée modèle à trou épaissi, a été développée au cours de cette thèse. La précision étant toujours relative au maillage, une méthode de maillage adaptatif augmentant automatiquement la résolution dans les zones clés a été proposée afin d'obtenir de meilleurs résultats pour un faible surcoût. Prédire la température des parois du tube à flamme est l'objectif final des ingénieurs. A cet effet, une méthodologie appelée Adiab2colo, permettant d'évaluer la température de paroi à partir d'un calcul adiabatique non résolu, a également été développée. Ces trois techniques sont maintenant couramment utilisées par Safran Helicopter Engine pour la conception des moteurs de demain.

**Mots clés :** Multiperforation, Couplage thermique, Aérodynamique, Simulation au grandes échelles.



# Contents

<b>I</b>	<b>General context</b>	<b>1</b>
	Motivation . . . . .	2
<b>1</b>	<b>What is a multiperforated plate and where it is needed</b>	<b>4</b>
1.1	Main parts of an engine . . . . .	5
1.2	Type of cooling devices . . . . .	6
1.3	Fluid mechanics equations . . . . .	8
1.4	Numerical method available . . . . .	11
1.5	Available studies of multiperforated holes . . . . .	15
<b>2</b>	<b>Numerical methods for effusion cooling</b>	<b>31</b>
2.1	Modeling strategies for aerodynamics . . . . .	32
2.2	Modelling strategies accounting for thermal evolution into the solid	37
2.3	Thesis objectives and organisation . . . . .	44
<b>II</b>	<b>Aerodynamic modelling</b>	<b>45</b>
<b>3</b>	<b>The thickened-hole model</b>	<b>46</b>
3.1	Hole resolution . . . . .	47
3.2	Presentation of the thickened-hole model [29] . . . . .	48
<b>4</b>	<b>Thickened-hole model applied on four academic cases</b>	<b>51</b>
4.1	Maveric test case . . . . .	52

4.2	Michel tube test case . . . . .	70
4.3	Thickened-hole model capabilities . . . . .	80
<b>5</b>	<b>Application to a Safran’s combustion chamber, an academic combustor and a turbine blade</b>	<b>81</b>
5.1	Presentation of the test case . . . . .	82
5.2	Comparison between homogeneous and thickened-hole models on real combustor . . . . .	83
5.3	FACTOR Combustor test case . . . . .	84
5.4	Cooled Nozzle Guide Vanes (NGV) . . . . .	86
<b>III</b>	<b>Thermal modelling</b>	<b>89</b>
<b>6</b>	<b>Conjugate heat transfer on a reference Maveric plate simulation</b>	<b>90</b>
6.1	Description of the numerical softwares . . . . .	91
6.2	The fully resolved conjugate heat transfer simulation . . . . .	93
6.3	Comparison between conjugate heat transfer and the adiabatic simulations . . . . .	94
6.4	Low order modeling of the plate temperature . . . . .	100
6.5	Estimation of the adiabatic temperature of the boundary layer . . .	103
6.6	Comparison of heat transfer modelling strategies . . . . .	105
6.7	A low-cost heat transfer modelling . . . . .	107
<b>7</b>	<b>Application to a Safran’s combustion chamber</b>	<b>108</b>
7.1	Application of the low-order model to a helicopter combustor . . . .	109
<b>IV</b>	<b>Toward high resolution LES of effusion cooling</b>	<b>113</b>
<b>8</b>	<b>Mesh local refinement to enhance effusion cooling models</b>	<b>114</b>
8.1	Motivation . . . . .	115
8.2	Aerodynamic prediction improvement: adaptive mesh refinement criterion . . . . .	115
8.3	Relevance of the mesh adaption . . . . .	122
8.4	An affordable LES including the meshing of effusion holes. . . . .	123

**9 Combination between thickened-hole model and heat transfer method** **125**

    9.1 Thermal prediction improvement . . . . . 126

**V Final conclusions and perspectives** **130**

**Appendices** **133**

**Bibliographie** **141**



# Part I

## General context

# Motivation

Aeronautical vehicles must prove various qualities: durability, robustness, easy maintenance, low fuel consumption, low noise levels and low pollution. The key ingredient here is the engine. Main manufacturers are Safran, General Electric, Pratt & Whitney and Rolls-Royce. These companies weight about 80 billion euros of annual turnover.



Figure 1: Typical aeronautical vehicles : an A380, a Rafale, a Tiger and a rocket (powered by a ramjet).

In this high technology market, showing innovation on a yearly basis is critical. However a particular trait of aeronautical business is the high level of regulation and certification. A single failure on one unit is often the trigger of economical setbacks. For example, on April 29, 2016, the crash of one Airbus's Helicopter EC225 grounded the worldwide EC225 fleet for months. To avoid these issues, Safran invests in laboratories like CERFACS (European Center for Research and Advanced Training in Scientific Computation). The goal of theses laboratories is

---

to propose, through the knowledge in fundamental physics, improvements or new processes such as Rotative Detonative Engine [26] or Constant Volume Combustion chamber [99, 98].

Playing a key role in the combustors' durability, effusion cooling is a very active field of research. Like many engineering fields, the design initially relied on experiments and real size tests. It gradually added smaller steps of computer-aided optimisation. Among these recent techniques, the numerical simulation of the components is now a new way of design. This work is therefore seeking improvements for the high fidelity simulations of effusion devices. It was financed by the CERFACS and supported by Genci allocation to tackle both scientific and industrial concerns.

## Chapter 1

# What is a multiperforated plate and where it is needed

In order to understand the importance of the effusion cooling, the first chapter presents a typical aircraft engine. For this purpose, existing cooling technologies including effusion cooling are introduced. Physical governing equations and the numerical methods needed to solve them are presented. This is followed by the definition of main parameters, geometrical and physical, that control the cooling efficiency. Finally, based on previous fundamental studies, the dynamic of the flow close to a jet's aperture is introduced.

<b>1.1</b>	<b>Main parts of an engine</b>	<b>5</b>
<b>1.2</b>	<b>Type of cooling devices</b>	<b>6</b>
1.2.1	Film cooling	7
1.2.2	Multijet impingement	7
1.2.3	Transpiration	7
1.2.4	Effusion cooling	8
1.2.5	Effusion cooling deserved specific effort	8
<b>1.3</b>	<b>Fluid mechanics equations</b>	<b>8</b>
1.3.1	Mass balance equation	8
1.3.2	Momentum balance equation	9
1.3.3	Energy balance equation	9
1.3.4	Concerning the solid	10
<b>1.4</b>	<b>Numerical method available</b>	<b>11</b>
1.4.1	RANS	11
1.4.2	LES	11
1.4.3	DNS	12
1.4.4	Law of the wall	13
<b>1.5</b>	<b>Available studies of multiperforated holes</b>	<b>15</b>
1.5.1	Geometrical parameters for effusion cooling	15
1.5.2	The deviation angle:	16
1.5.3	Physical parameters relevant to effusion cooling	17
1.5.4	Dynamic structure of the flow	21

## 1.1 Main parts of an engine

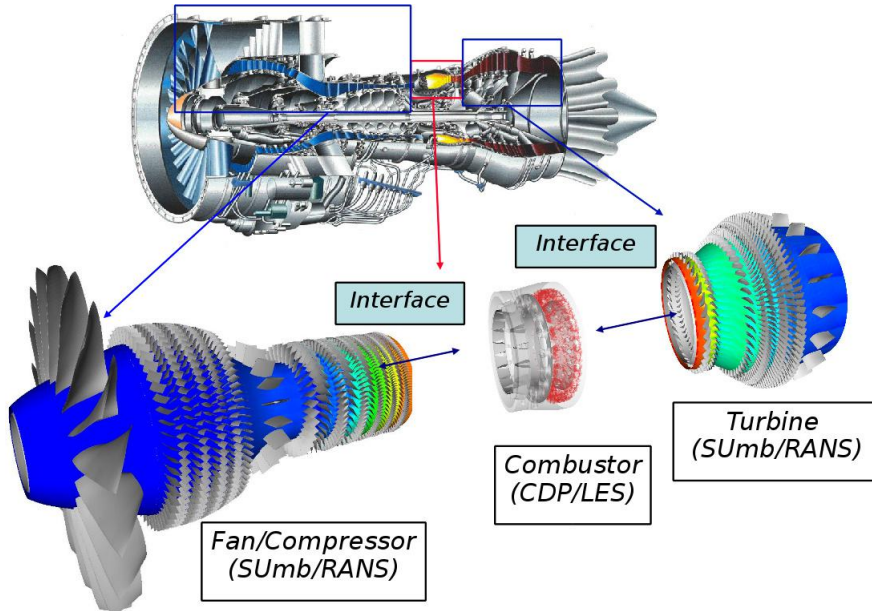


Figure 1.1: Visualisation of the three main parts of an aeronautic engine. (Pratt & Whitney engine, from Stanford University [3]).

Aircraft engines rely on a Brayton thermodynamic cycle where four distinct zones can be identified (Fig.1.2). Based on these zones, engines can be split into three parts which can be then separately studied Fig. 1.1. The first step consists in the compression of the air through a multi stage compressor. Then an isobaric combustion occurs in the combustor and gives energy to the fluid. The fluid goes then in the turbine which permits to drive the compressor. In the case of a turboprop, the turbine also drives a propeller, while in the case of a turboreactor, the remaining power is accelerated prior the exhaust by a nozzle to provide thrust. These three phases are classically represented on a P-v and T-s diagram (see Fig.1.2).

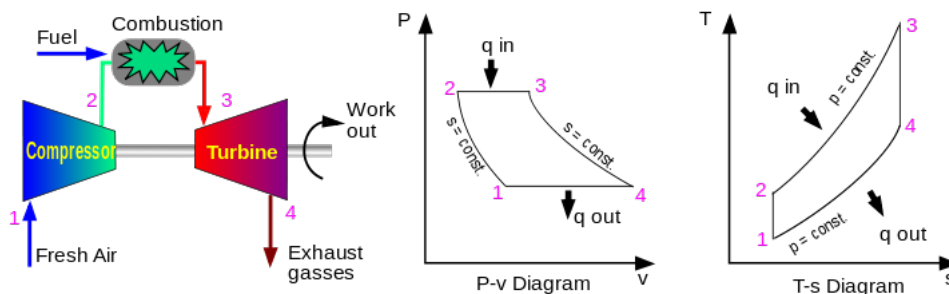


Figure 1.2: Schematical Brayton cycle, evolution on a P-v and on a T-s diagram.

In the combustor, fuel is burned to create hot gases. They can reach up to 2400K when the steel melts around 1200K. For this reason, the liner needs to be cooled. To that purpose, a space between the liner and the carter named casing is needed as presented on Fig. 1.3. More than half of the fresh air is injected progressively from the casing through the liner, enabling cooling devices. The following section presents some of the cooling strategies available.

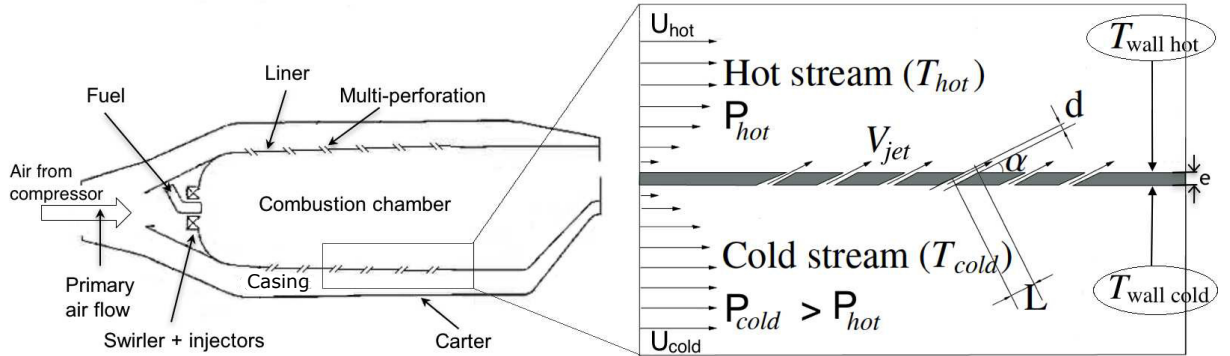


Figure 1.3: Localisation of a multiperforated plate on an aircraft combustor.

The air used to cool down the liner comes from the compressor at high pressure and high temperature, between 600 and 900K depending on the engine and the operating point. According to [102], the air cooling techniques can be classified as follows:

- Internal cooling for external stream temperature between 1300K and 1600K: convection cooling, impingement cooling, internal air-cooled thermal barrier.
- External cooling for external stream temperature over than 1600K: local film cooling, full-coverage film cooling, transpiration cooling.

Frequently, several devices are used on the same engine. One key point is to reduce the amount of air used for cooling. Indeed, this cold air cannot be used elsewhere, such as for the combustion [109] penalising the combustor's efficiency. In the following section, the most common devices are presented.

## 1.2 Type of cooling devices

In this document, jet in cross-flow stands for one jet, film cooling stands for one or two rows of holes, effusion cooling stands for many rows.

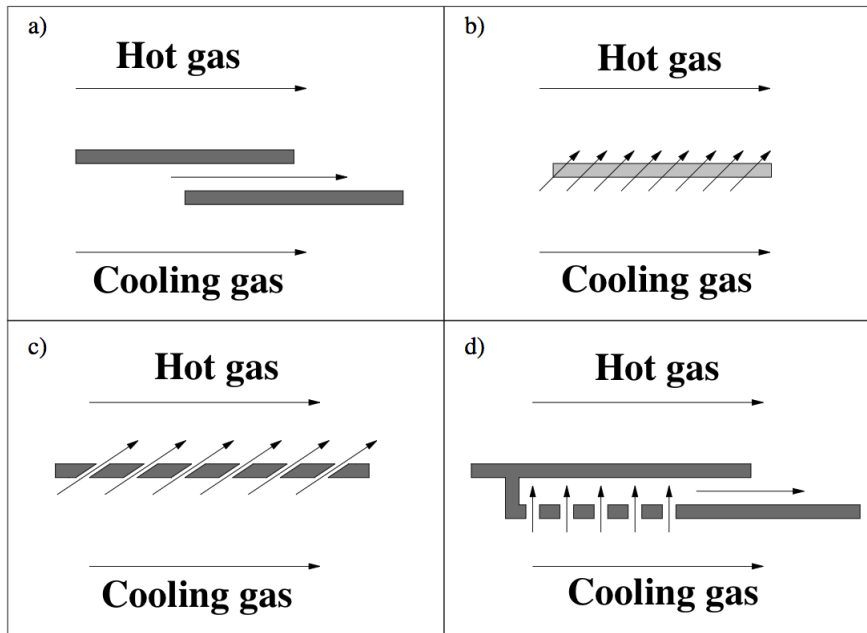


Figure 1.4: Alternative types of wall cooling. a) Film cooling. b) Transpiration cooling. c) Effusion cooling. d) Multijet impingement combined with a film cooling.

### 1.2.1 Film cooling

The film cooling (Fig. 1.4 a) is one of the most simple technique. By injecting air through a slot, it creates a very homogeneous cold layer of air. However, it needs a high mass flow rate and the protection is not efficient far from the slot. This technique is used on zones with high thermal stress.

### 1.2.2 Multijet impingement

Multijet impingement consists in blowing cold air on one side. Since the blowing is higher than natural convection, it increases the heat transfer. Even if it needs additional liners, which increase the weight, it is commonly used near high curvatures where films are difficult to maintain. A specific literature, for example [6, 5], is dedicated to this technology.

### 1.2.3 Transpiration

The transpiration is theoretically the most efficient system [110]. Liner is porous and the air perspire through micro-apertures. As holes are very small and very close, the jets coalesce to a homogeneous layer and stay close to the wall. However, this system has two drawbacks: small particles can plug the holes, and porous materials

show low mechanical resistance. For these two reasons this system is not used in aeronautical combustors.

### 1.2.4 Effusion cooling

In modern combustors, effusion cooling [110], Fig. 1.3, is often used for its efficiency, compactness and lightness with advantages similar to the porous materials. Thousands of holes are laser-drilled in the liner with a diameter lower than 0.5 mm [152]. Due to the pressure difference between the casing and the combustor chamber, a micro-jet is formed at each aperture of the perforated plate. These micro-jets interact and form a consistent film which mixes with the hot gases from the combustion chamber. This method cools down the liner through the hole (internal cooling) and it also creates a cold film which protect the wall (external cooling).

### 1.2.5 Effusion cooling deserved specific effort

By increasing the compressor pressure ratio, manufacturers have successfully improved the efficiency of the thermodynamic cycle used in aeronautical gas turbines [163]. In parallel, new techniques used to reduce pollutants like the Rich-Burn, Quick-Mix, Lean-Burn (RQL [156]) imposed a drastic reduction of the amount of air available for the cooling of the combustor. The price to pay for these improvements is a higher thermal stress on the walls of the combustion chamber. In this context, optimizing the cooling devices becomes a priority [71]. Among the existing methods, most of the cooling air is taken by effusion cooling. Since the number of degree of freedom is huge, it leads to a high number of parameter to optimize. Another advantage of the effusion cooling is to enable additional flow control, such as inducing rotating combustion.

## 1.3 Fluid mechanics equations

Computational Fluid Dynamic (CFD) is a powerful method to study the aerodynamics and the thermodynamics of a flow. It consists in solving fluid mechanics equations from Navier-Stokes which are expressed, for mono-species, in the following section.

### 1.3.1 Mass balance equation

The mass equation [150] comes from a balance inside a fluid volume. The mass variation contained in this volume changes as a function of the mass flux going through it; and can be mathematically written:

$$\frac{\partial}{\partial t} \int_A \rho dx^3 = - \int_{\partial A} \rho \vec{u} \cdot \vec{n} dx^2, \quad (1.1)$$

with  $\rho$  the fluid density,  $\vec{u}$  the fluid velocity,  $dx^3$  the control volume and  $dx^2$  the surface which delimits the control volume. Using the Green-Ostrogradski theorem to convert an integral over a surface to a volume, it becomes :

$$\frac{\partial}{\partial t} \int_A \rho dx^3 + \int_{\partial A} \nabla \cdot (\rho \vec{u}) dx^2 = 0. \quad (1.2)$$

Then integrated over the volume, because the volume is not a function of the time, it becomes the mass continuity equation:

$$\frac{\partial \rho}{\partial t} + \nabla \cdot (\rho \vec{u}) = 0. \quad (1.3)$$

### 1.3.2 Momentum balance equation

The second equation of Navier-Stokes comes from the second law of Newton;  $m\vec{a} = \sum_i F_i$ , where  $\vec{a}$  is the acceleration and can be expressed as a function of the velocity as follows:  $\vec{a} = \frac{D\vec{u}}{Dt} = \frac{\partial \vec{u}}{\partial t} + \vec{u} \cdot \nabla \vec{u}$

Adding the gravity as an external force, the pressure and the velocity (with  $\tau$  the viscous tensor), the momentum balance equation can be written as follows :

$$\int_A \rho \left( \frac{\partial \vec{u}}{\partial t} + \vec{u} \cdot \nabla \vec{u} \right) dx^3 = \int_A \left( \nabla \cdot \tau - \nabla p + \rho g \right) dx^3 \quad (1.4)$$

When integrated over a control volume it becomes the momentum Navier-Stokes equation:

$$\frac{\partial}{\partial t} (\rho \vec{u}) + \nabla \cdot (\rho \vec{u} \otimes \vec{u}) = -\nabla p \mathbb{I} + \nabla \cdot \tau + \rho g \quad (1.5)$$

### 1.3.3 Energy balance equation

The first law of thermodynamics allows to write the following equation:

$$\int \frac{D}{Dt} \rho E dx^3 = W + Q, \quad (1.6)$$

With  $E$ , the total energy which is the sum of the internal energy ( $e$ ) and the kinetic one ( $\|\vec{u}\|^2 / 2$ ).  $W$  and  $Q$  are the work and the heat added to the control volume and expresses as follows:

$$W = \int_{\partial A} \vec{u} \cdot (-\tau + p\mathbb{I})\vec{n} dx^2 + \int_A \vec{u} \cdot \vec{f}_e dx^3 = \int_A (\nabla \cdot (\vec{u} \cdot \tau - \vec{u}p) + \vec{u} \cdot \vec{f}_e) dx^3 \quad (1.7)$$

$$Q = \int_{\partial A} \vec{q}\vec{n} dx^2 = \int_A \nabla \cdot \vec{q} dx^3 \quad (1.8)$$

It leads to the energy equation:

$$\frac{\partial}{\partial t}(\rho E) + \nabla \cdot (\vec{u}(\rho E + p)) = \nabla \cdot (\vec{u}\tau - \vec{q}) + \vec{u} \cdot \vec{f} \quad (1.9)$$

To solve the Navier-Stokes equations, additional equations are required, such as the constitutive equation for the viscous stress which can be written, with the approximation of Newtonian fluids, as follows:

$$\tau = \mu(2S_{ij} - \frac{2}{3}\nabla \cdot \vec{u}\mathbb{I}) \quad (1.10)$$

With  $S_{ij}$  the strain tensor. The thermal flux is also needed and can be modeled by a Fourier law:

$$\vec{q} = -\lambda\nabla T \quad (1.11)$$

The last approximation usually admitted is the perfect gas equation of state:

$$P = \rho r T \quad (1.12)$$

### 1.3.4 Concerning the solid

In the solid, there is no motion, however, heat can be transferred by conduction. The efficiency of this process depends on the heat conduction coefficient  $\lambda_s$  (conductivity) ( $W m^{-1} K^{-1}$ ) and the heat capacity  $C_p$  ( $J K^{-1} Kg^{-1}$ ). The following equation can be written:

$$\rho_s C_p \frac{\partial T_s}{\partial t} + \frac{\partial}{\partial x_i} \left( -\lambda_s \frac{\partial T_s}{\partial x_i} \right) = Q, \quad (1.13)$$

with  $Q$  the heat source and  $\rho_s$  the density of the solid. Note that  $\lambda_s, \rho, C_p$  depend on the material used and the local temperature. Heat conduction involves the resolution of a Poisson problem. To solve it, many numerical approaches can be found in the linear algebra of sparse matrices.

## 1.4 Numerical method available

To solve the Navier-Stokes equations, the main numerical methods are RANS, LES, DNS, from the more affordable to the most expensive.

### 1.4.1 RANS

In Reynolds Average Navier Stokes Simulation (RANS), all the turbulent energy scales are modelled (see Fig. 1.5). Closure is generally allowed by a turbulence model ( $k - \epsilon$ ,  $k - \omega$ , Reynolds stress ...) which approximates the  $(-\rho \overline{u'_i u'_j})$  term. It arises from the non-linear convective terms when the average operator is applied to the Navier-Stokes equations to derive the Reynolds equations. The result is an average of the possible states and not a specific realisation.

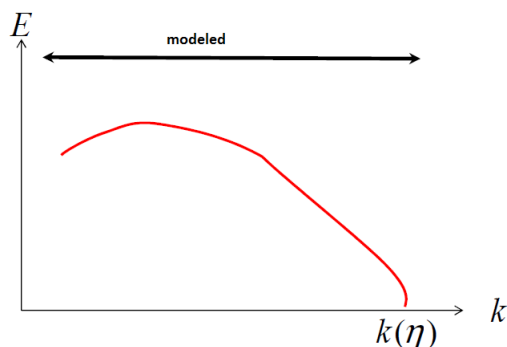


Figure 1.5: Kolmogorov energy cascade, RANS modelling, adapted from [150]

The method was extended to harmonic (*i.e.* cyclic) flow, denoted as URANS allowing their use in turbomachinery (see [150]).

### 1.4.2 LES

Another method to solve the Navier-Stokes equations is the Large Eddy Simulation (LES) [151, 161, 112]. LES has been proved to provide accurate predictions in industrial propulsion systems without a priori knowledge of the flow [32, 175, 115, 64]. Balance equations are obtained by filtering instantaneous Navier-Stokes equations. Low frequency variations are captured (big structures with high energy, see Fig. 1.6), whereas frequencies higher than the cut off wave number  $K_c$  are not solved and thus their effects are modeled thanks to a subgrid model (Smagorinsky, Wale,  $\sigma$  ...).

This method is more expensive than a RANS/URANS simulation (see Fig. 1.8). The near wall region is an active research field by itself. Another method to handle this issue and to avoid the difficult issue of wall modeling in the LES context, is to

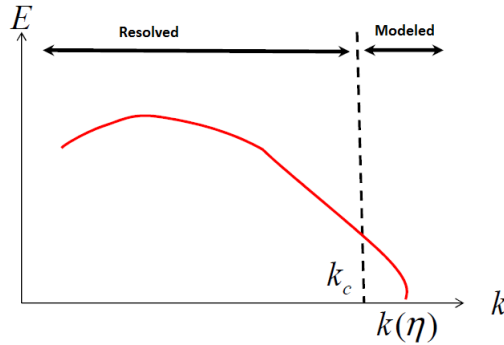


Figure 1.6: Kolmogorov energy cascade highlighting LES method, adapted from [150]

combine the good effectiveness of the LES far from the wall to a RANS method. These methods are called Hybrid methods.

Hybrid methods ([68, 69, 51, 168, 167, 73, 33]) have a crucial junction point which led to many methods such as:

- Detached Eddy Simulation (DES)
- Delayed Detached Eddy Simulation (DDES)
- Zonal Detached Eddy Simulation (ZDES)
- Improved Delayed Detached Eddy Simulation (IDDES)

### 1.4.3 DNS

The third method is the Direct Numerical Simulation (DNS), full instantaneous Navier-Stokes equations are solved without any turbulence model. The principle of the DNS is to solve all the energy spectrum which this leads to a mesh size of the order of the Kolmogorov scale ( $\eta = \left(\frac{\nu^3}{\epsilon}\right)^{1/4}$ ) considered as the smallest turbulence size before dissipation by the viscosity. Temporal scales of the turbulence must be resolved too, leading to a small time step (explicit numerical strategies).

To summarize, on Fig. 1.7 the evolution of the local velocity is presented for the four numerical methods presented; results from DNS are usually used for reference. However, due to its very important cost this method is only suitable for low Reynolds number. Indeed the ratio of the largest and smallest eddies is a function of the Reynolds number ( $\frac{L}{\eta} \sim Re^{3/4}$ ). On Fig. 1.8, numerical methods are represented as a function of the resolved scales; which is directly linked with the computational cost.

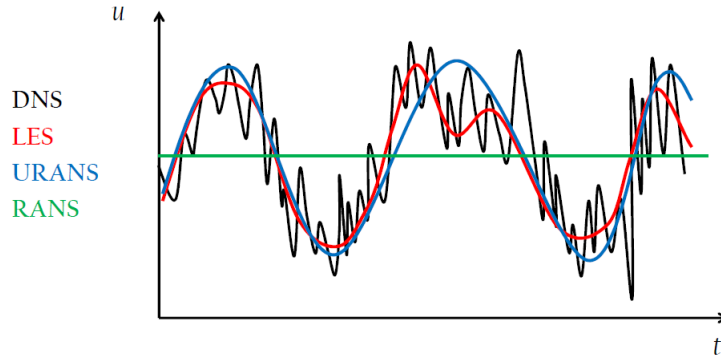


Figure 1.7: Comparison of the time evolution of the local velocity computed with the four numerical methods, in the case of a cyclic flow.

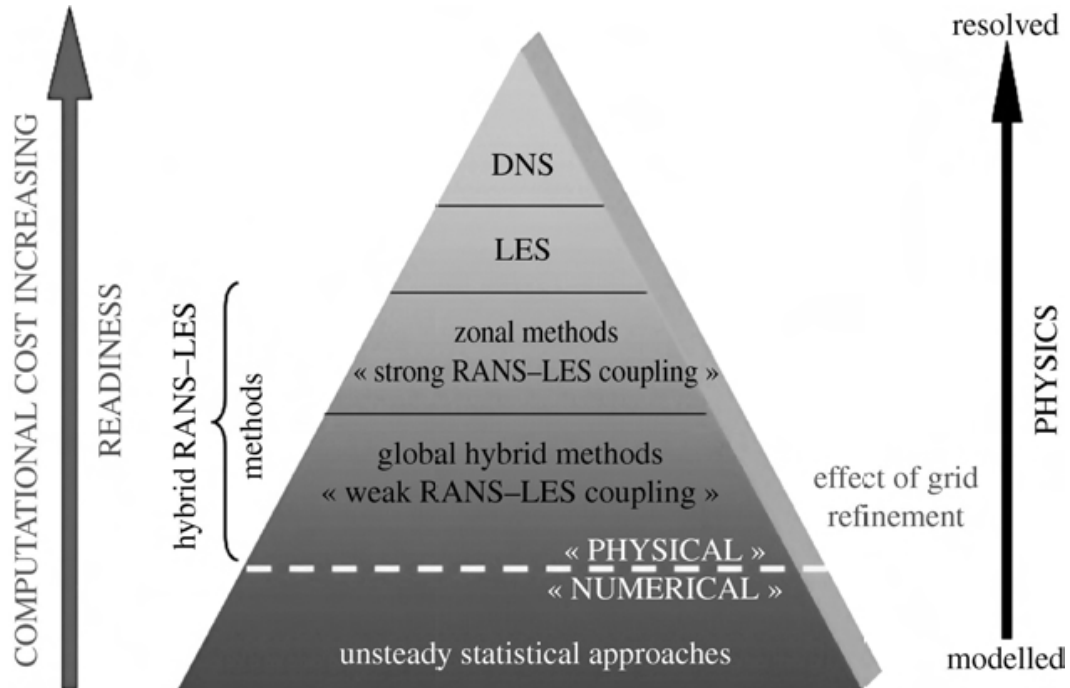


Figure 1.8: Scheme representing the main turbulence modeling methods as a function of the computational cost and the resolved scales. From Sagaut *et al.* [160]

#### 1.4.4 Law of the wall

In solver, the most difficult and expensive parts are the boundaries, especially the walls. Indeed, to accurately compute the wall shear stress and heat fluxes, high resolution meshes are needed. To stay affordable, models which allow the use of lower grid resolution have been proposed.

The first step consists in the definition of the wall units as a function of the wall shear stress and the density. The friction velocity can be written:

$$u_\tau = \sqrt{\frac{\tau_w}{\rho}} \quad (1.14)$$

The non-dimensional wall distance ( $y^+$ ) which characterizes the grid resolution can now be defined:

$$y^+ = \frac{y u_\tau}{\nu} \quad (1.15)$$

Followed by the non-dimensional velocity  $u^+$ :

$$u^+ = \frac{u}{u_\tau} \quad (1.16)$$

The non dimensional temperature  $T^+$  can also be expressed as:

$$T^+ = (T - T_w) \frac{\rho_w C P_w U_\tau}{q_w} \quad (1.17)$$

$y^+$  and  $u^+$  are linked, the relation is shown on Fig. 1.9.

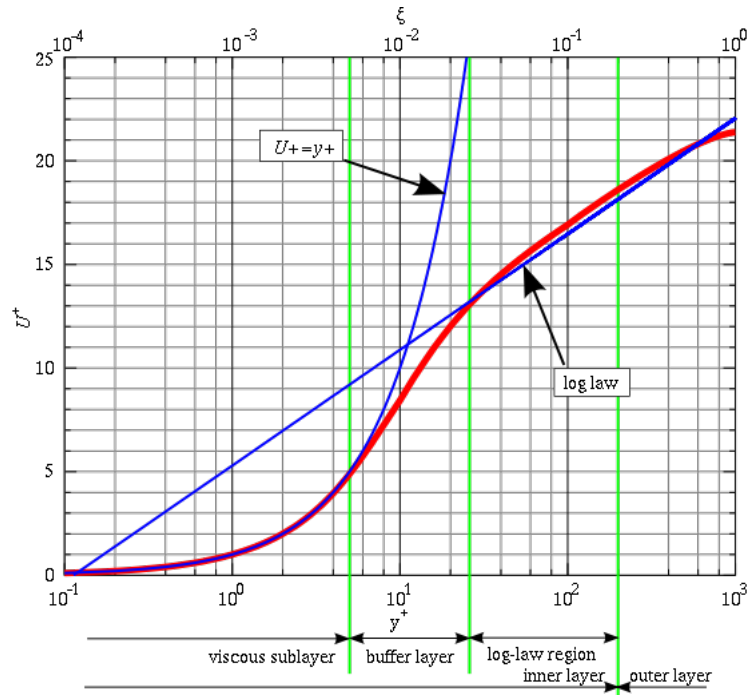


Figure 1.9: Representation of the evolution of  $y^+$  as a function of  $u^+$  using logarithmic scale. [140]

This figure highlights three parts. In the viscous sub-layer or laminar zone,  $y^+ < 7$ , where the viscous forces are the strongest; the following relation can be

written:

$$u^+ = y^+ \quad (1.18)$$

$$T^+ = Pr_t y^+ \quad (1.19)$$

The log law-layer,  $y^+ > 30$ , where turbulence has a high impact. In this part the relation becomes:

$$u^+ = \frac{1}{k} \ln(y^+) + C_U \quad (1.20)$$

$$T^+ = \frac{Pr_t}{k} \ln(y^+) + C_T \quad (1.21)$$

The part in between called buffer layer,  $7 < y^+ < 30$ , is a zone where molecular and turbulence viscosity are of the same order. None of the previous laws can be applied.

## 1.5 Available studies of multiperforated holes

### 1.5.1 Geometrical parameters for effusion cooling

The efficiency of a cooling system is driven essentially by jet-to-jet distance, perforation arrangement, hole shape, size and inclination. Typical values are given in Table 1.1.

Parameter	nomenclature	value
Diameter	$d$	0.3 to 1 mm
spanwise distance	$\Delta z$	$4d$ to $8d$
stremwise distance	$\Delta x$	$4d$ to $8d$
liner's thickness	$e$	$1d$ to $3d$
length of the hole	$L$	$1d$ to $6d$
injection angle	$\alpha$	$15^\circ$ to $90^\circ$
deviation angle	$\beta$	$0^\circ$ to $90^\circ$
porosity	$\sigma$	1% to 19%

Table 1.1: General geometrical parameters for effusion cooling.

In order to quantify the effect of these parameters, many arrangements have been studied in the literature. For example, it has been shown that staggered inclined perforations offer a better protection than in line inclined perforations (Metzger *et al.* [127], LeBrocq *et al.* [109], Crawford *et al.* [46] and Hale *et al.* [76]). Also the optimal lateral and spanwise hole distances have been found in the range  $4d - 8d$ ,

where  $d$  is the hole diameter (Mayle and Camarata [121], Sinha *et al.* [165] and Pietrzyk *et al.* [149]).

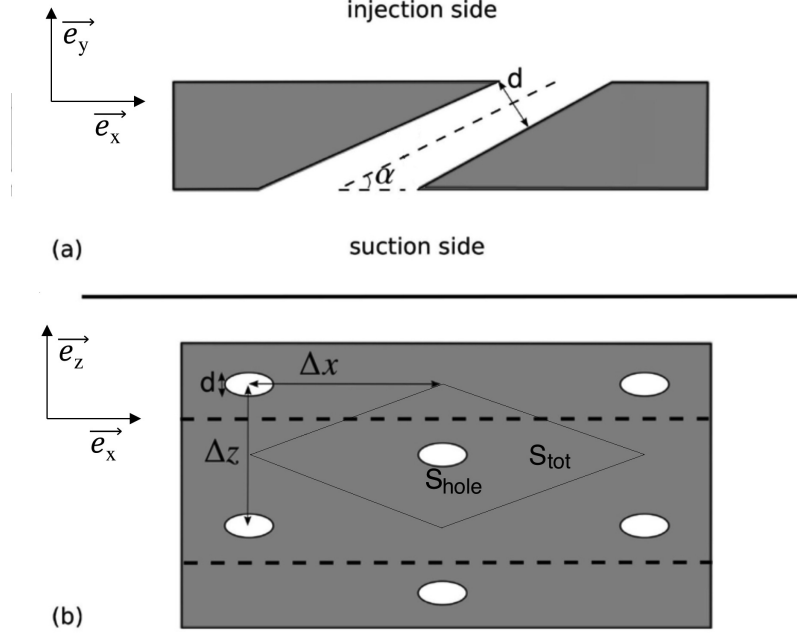


Figure 1.10: (a) cut of a hole. (b) upside view of the plate.

The distances between holes ( $\Delta x, \Delta z$ ) and the diameter of the aperture ( $d$ ) reported in Fig. 1.10 allow to compute the plate porosity  $\sigma$  which stands for the ratio between the drilled surface ( $S_{hole}$ ) compared to the total surface ( $S_{tot}$ ) delimited by the diamond pattern visible on Fig. 1.10. A typical value of porosity found in aircraft combustor covers the range [0.02;0.05].

$$\sigma = \frac{S_{hole}}{S_{tot}} = \frac{\pi d^2}{4 \sin(\alpha)} \frac{1}{\Delta x \Delta z}, \quad (1.22)$$

where  $\alpha$ , shown in Figs. 1.3 and 1.10, is the angle between the streamwise and the perforation directions.

### 1.5.2 The deviation angle:

The deviation angle ( $\beta$ ) between the jet and the flow is presented on Fig. 1.11. Very few studies have been performed with a deviation angle. To the author's knowledge, it has been experimentally studied by Kaszeta *et al.* [93, 92], numerically and experimentally by Michel *et al.* [128]. More recently it has also been studied by Arroyo *et al.* [20, 39, 21] thanks to RANS simulation. The only study using LES comes from Lahbib *et al.* [101] who pointed out its influence on the adiabatic effectiveness.

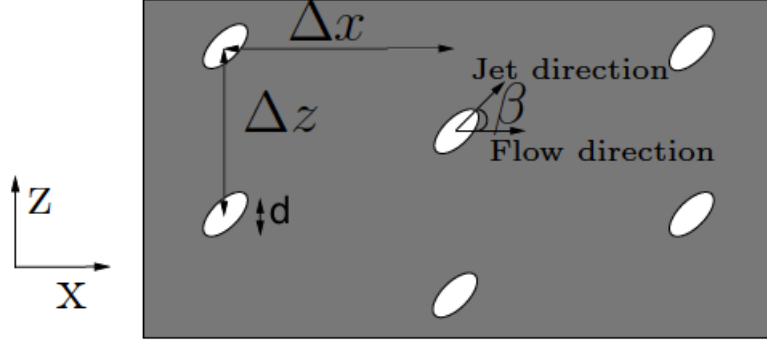


Figure 1.11: Top view of a multiperforated plate with deviation angle  $\beta$ .

From these results, it has been shown that the deviation angle increases the efficiency of the wall cooling. That is why, effusion with deviation is more and more used by manufacturers [2].

### 1.5.3 Physical parameters relevant to effusion cooling

Similarly to single jet-in-cross flow configurations [153], the flow regime around a multi-perforated plate is piloted by the blowing ( $M$ ) and the momentum ( $J$ ) ratios defined as:

$$M = \frac{\rho_{jet} V_{jet}}{\rho_{hot} U_{hot}}, \quad (1.23)$$

$$J = \frac{\rho_{jet} V_{jet}^2}{\rho_{hot} U_{hot}^2}, \quad (1.24)$$

where  $\rho_{jet}$  and  $V_{jet}$  denote the jet density and the jet velocity respectively while  $\rho_{hot}$  is the density and  $U_{hot}$  is the streamwise velocity of the hot gases (see Fig. 1.3). With this, the velocity ratio is  $V_r = J/M$ .

Figure 1.12 from Fric and Roshko [67] shows jet trajectories at three values of the velocity ratio, determined from smoke visualisations. At a velocity ratio near 2, jet remains very close to the wall. Near  $V_r=4$ , the jet is far enough from the wall to be separated from the boundary layer. At a higher velocity ratio, Fig. 1.12 (c), the jet penetrates deeper and the jet plume is only deviated.

Petre [146] experimentally visualised jets with various  $M$  ratios for different row numbers. It shows that both position and  $M$  ratio influence the structure of the jet (see Fig. 1.13) and specifically the penetration. For the first rows, a small momentum ratio leads to a crawling jet, very close to the wall; On the contrary with a high momentum ratio, jet goes deeper. When the flow is established, after the ninth row say, small blowing ratio leads to a higher penetration compared than on

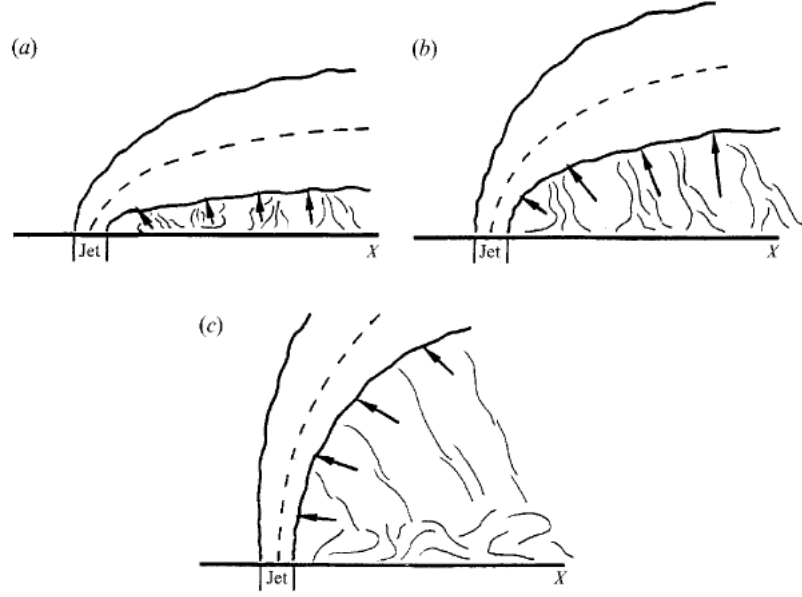


Figure 1.12: Trajectories of jets and their entrainment patterns at different velocity ratios.  $V_r = 2$ ;  $V_r = 4$ ;  $V_r = 8$ . From [67].

the first row. Whereas, with high blowing,  $M=5$  say, the penetration is smaller on established zone than on the first row. Note however than the higher is the blowing ratio the better is the wall protection.

Ammari *et al.* [8] underline that  $M$  and  $J$  also impact the heat fluxes through the density ratio  $D_R$  defined as:

$$D_R = M^2/J = \frac{\rho_{jet}}{\rho_{hot}} . \quad (1.25)$$

Gustafsson [74] showed that the Mach number does not play a significant role on the cooling effectiveness at least in the flow regimes characteristic of typical industrial applications. Eriksen and Goldstein [58] and Champion [40] drew the same conclusion for the Reynolds number of the injection flow. Therefore, when comparing the efficiency of multi-perforated cooling strategies, the operating point is suitably defined once  $M$  and  $J$  have been selected.

The cooling effectiveness  $\eta$  is a non-dimensional quantity usually introduced to characterize the thermal efficiency of effusion [120]; it is defined as:

$$\eta = \frac{T_{hot} - T_{wall\ hot}}{T_{hot} - T_{cold}} , \quad (1.26)$$

where  $T_{hot}$ ,  $T_{cold}$  and  $T_{wall\ hot}$  stand for the temperature of the fluid at the injection side (combustion chamber), at the suction side (casing) and of the plate on the hot side, respectively (Fig. 1.3). To characterize the mixing phenomenon in the

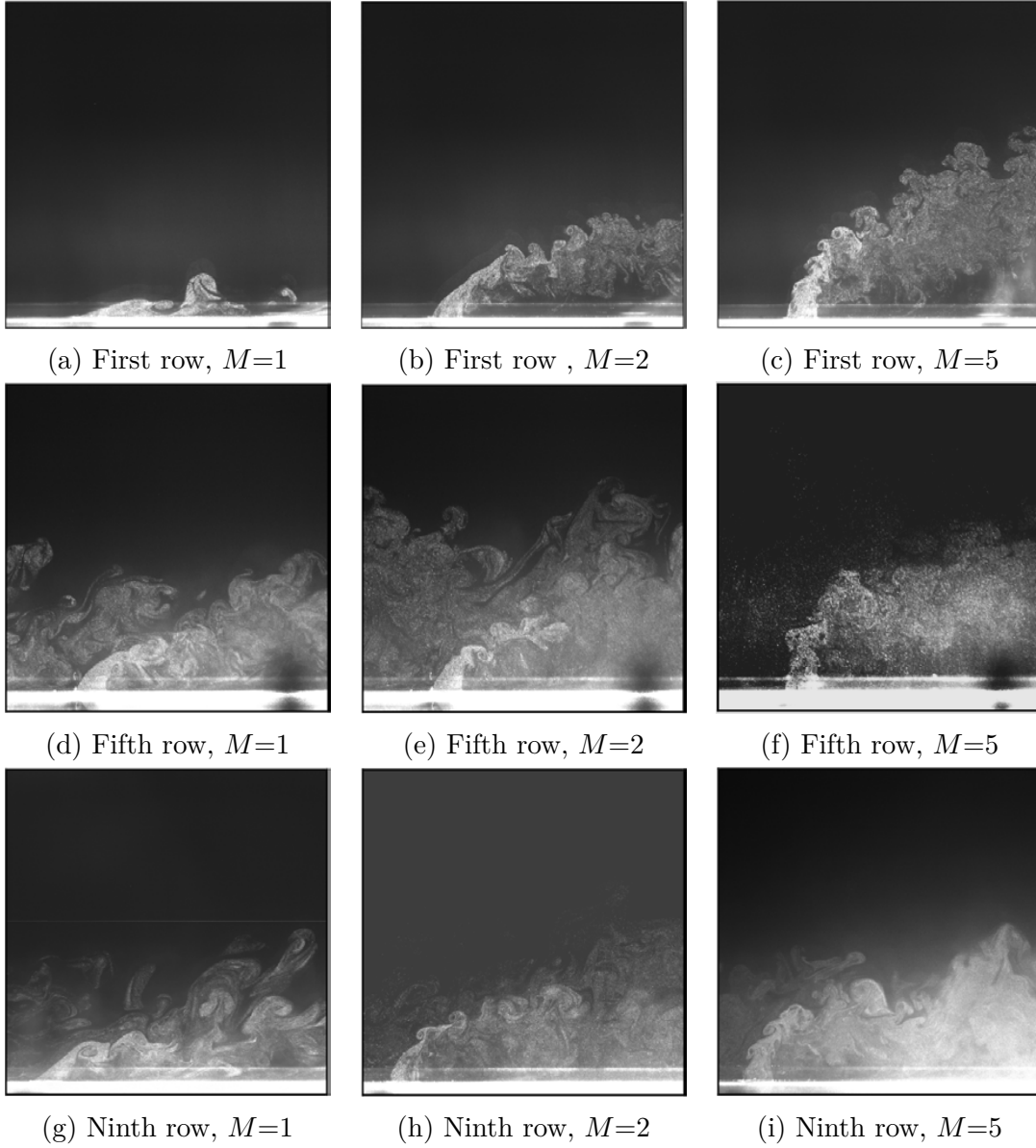


Figure 1.13: Visualisation of perforations at  $\alpha = 90$  and  $\beta = 0$  from Petre [146].

fluid domain without the effect of conjugate heat transfer which modifies  $T_{wall\ hot}$ , the adiabatic cooling effectiveness  $\eta_{ad}$  is also often introduced:

$$\eta_{ad} = \frac{T_{hot} - T_{ad\ hot}}{T_{hot} - T_{cold}}, \quad (1.27)$$

where  $T_{ad\ hot}$  is the wall temperature on the injection side for a non-conducting plate. From a practical point of view,  $\eta_{ad}$  can be assessed numerically by using adiabatic thermal condition on the solid boundary and experimentally by using either a low conductivity plate (in order to minimize the heat exchange between the fluid and solid domains) or by measuring the concentration of a passive scalar

Experimental setup					
Reference	M/J	Rows	$\alpha$	Regions	Data
Leger <i>et al.</i> [111]	1-3 / 7-12	9-35	60	Injection	T, $\eta$
Andreini <i>et al.</i> [14]	7.2 / 16	21	60	Injection	$\vec{V}$ , T, $\eta$
Miron <i>et al.</i> [132]	3.6 / 13	12	30	Injection	$\vec{V}$
Michel <i>et al.</i> [128]	8.8 / 77.4	9	60	Injection	$\vec{V}$
Scrittore <i>et al.</i> [164]	3.2-5 / 12-27	30	60	Injection	$\vec{V}$ , $\eta_{ad}$
Zhong and Brown [176]	0.4 / 0.1	12	90	All	$\vec{V}$ , T, $\eta$ , $\eta_{ad}$
Andreini <i>et al.</i> [18]	0.5-5 / 0.2-25	14-22	30,90	Injection	$\eta_{ad}$ , $\eta$
Jonhson <i>et al.</i> [89]	0.4-1.7 / 0.2-0.9	3	30	Injection	$\eta_{ad}$ , $\eta$
Kakade <i>et al.</i> [91]	0.5-2 / 0.15-4.1	6	20	Injection	$U$ , $\eta_{ad}$ , $\eta$
Martiny <i>et al.</i> [118]	0.5-3 / 0.14-5.3	8	17	Injection	$\eta_{ad}$ , $\eta$
Andreini <i>et al.</i> [12]	0.8-4.5 / 0.6-20	23	20, 30, 90	Injection	$\eta_{ad}$
Andreini <i>et al.</i> [13]	1.5-7 / 1.3-49	29	30	Injection	$\eta_{ad}, \eta$
Numerical setup					
Reference	M/J	Rows	$\alpha$	Regions	Data
Most [133]	1.3-2.3 / 1.8-4.6	12	60	Injection	$\vec{V}$
Harrington <i>et al.</i> [80]	0.4 / 0.8	10	90	Injection	$T_{ad}$ , $\vec{V}$ , $\eta_{ad}$
Errera and S. chemin [59]	1.2 / 0.5	12	45	All	T
Mendez and Nicoud [126]	1.5 / 2.25	$\infty$	30	All	$\vec{V}$
Zhong and Brown [177]	0.4 / 0.1	12	90	All	T, $\eta$ , $\eta_{ad}$
Cottin [45]	3.2-8.5 / 3-21	15	30	All	T, $\eta$
Florenciano [60]	8.4 / 31	12	28	All	T
Florenciano and Bruel [61]	8.0 / 29	12	30	All	T, $\eta$ , $\eta_{ad}$
Andrei <i>et al.</i> [10]	1-3 / 0.6-9	18	30, 90	Injection	$\eta_{ad}$

Table 1.2: Review of the experimental and numerical multi-perforated plate setup. The quantities reported in the last column "Data" have been either measured or computed in either the injection side or the whole fluid domain as depicted in column "Regions". The subscript "ad" refers to adiabatic values.

introduced from the casing side [78].

Table 1.2 gathers the dynamic and geometrical parameters relative to the main experimental and numerical studies relevant to effusion; the type of variable investigated are also reported. Most of the previous studies have been performed at low to moderate blowing and momentum ratios. It should be noted, however, that multiperforated plates in real combustion chambers operate at larger injection rate, with  $M$  and  $J$  of order 5-20 and 30-90, respectively. One reason for this mismatch is that many studies rely on upscaled geometries to ease measurements. Operating at lower injection rate obviously modifies the characteristics of the effusion flow, especially in the injection region. It may also have consequences regarding the thermal equilibrium of the plate by modifying the mixing between cold and hot gas as well as the relative strengths of the conduction (exchange through the solid plate) and the convection (fluid going through the holes) heat transfers. According to Cottin [45], the heat flux transmitted by conduction within the hole is as large as 37% of the total heat flux (convection and conduction) in the case of the LARA experiment of Miron [132] where  $M=3.6$  and  $J=13$ ; on the contrary, Florenciano [60] found that it was only 8% of the total heat flux in a flow regime corresponding to  $M=8.4$  and  $J=31$ .

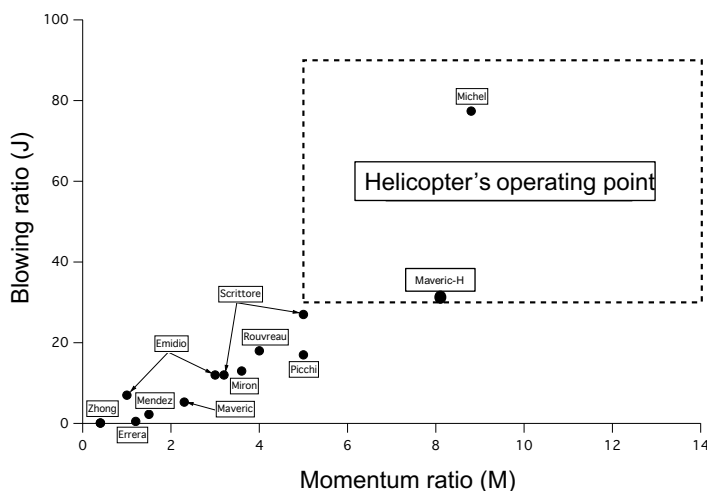


Figure 1.14: Helicopter's operating point (adapted from [100])

Lahbib [100] showed that for aeronautical applications,  $M$  and  $J$  ratio are much higher than the ones commonly found in the literature (see Fig. 1.14) highlighting a lack of tests and knowledge for high momentum ( $M$ ) and blowing ( $J$ ) ratios.

#### 1.5.4 Dynamic structure of the flow

Three parts can be distinguished: The flow at the suction side, the global structure into the aperture and the jet which emerges in the injection side.

**Suction side:**

MacManus and Eaton [114] were the firsts to investigate experimentally the structure of the flow on the suction side. It was then studied by [20, 177, 176]. As presented on Fig. 1.15, air from the main flow is sucked into the hole. A deformation of the flow occurs, called mean distortion flow due to the pressure gradient: the normal velocity increases near the perforation as well as the longitudinal velocity. This leads to a suction envelope, where all the air present goes into the aperture. The size depends on the suction ratio  $SR = V_{jet}/U_{cold}$  [38]. Macmanus and Eaton [114] also highlighted longitudinal vortices due to the velocity gradients downstream the hole, as presented on Fig. 1.15.

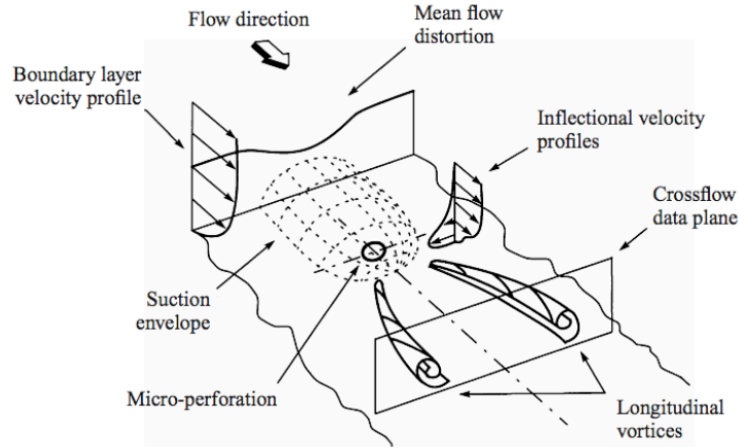


Figure 1.15: Flow structure of laminar boundary layer suction around a perforation from MacManus and Eaton [114]

Peet [143] presented with more precision the evolution of the velocity close to the hole thanks to a resolved LES. More details can be seen in the corresponding PhD thesis [143], with an experimental setup taken from [149] and [148]. Both sides (injection and suction) are computed including the inner hole's region. Normal velocity measurements are displayed on Fig. 1.16. The curves show that two diameters upstream of the perforation, the flow is still undisturbed by the strong pressure gradient. Closer to the perforation, the normal velocity increases and the maximum is found at the downstream of the perforation. The influence of the pressure gradient in the normal direction is also visible two diameter below the perforation, the vertical velocity increases, its amplitude is small but the flow is disturbed on a longitudinal length of the size of the perforation.

Fig. 1.17 from [125] presents the structure of the flow on the suction side by displaying, in a horizontal plane located  $0.5d$  under the suction wall, contours and isolines of the three components of the time-averaged velocity in Figs. 1.17 (a-c)

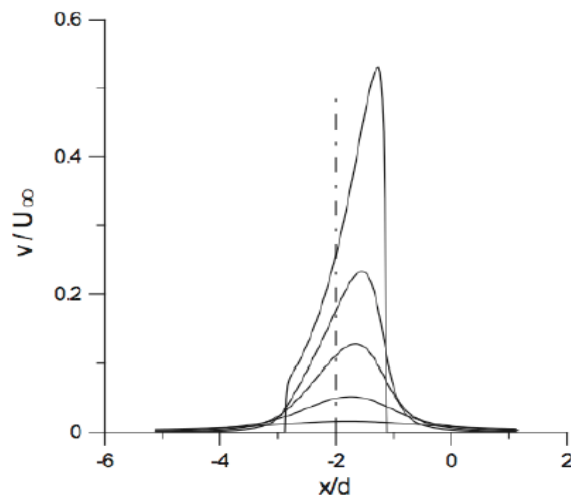


Figure 1.16: Dimensionless mean normal velocity profiles on the suction side on the symmetry plane ( $z=0$ ) from Peet (2006) [143]. Distance from the wall (from top to bottom) :  $y= 0, 0.25d, 0.5d, d, 2d$ . The dashed line locates the center of the perforation.

and contours of the  $Q$  criterion [82] calculated from the time-averaged velocity in Fig. 1.17 (d). The acceleration of fluid entering the hole can be seen in Fig. 1.17(b), on the time averaged vertical velocity field. The spatial-averaged vertical velocity over the horizontal plane is  $0.02 V_j$  but locally in the cutting plane, it reaches  $0.3 V_j$ . Note also that the maximum of the vertical velocity is not centred under the hole inlet but located downstream from the center as already concluded by [143]. According to [125], the suction through the hole influences the three components of the velocity. Figure. 1.17(a) shows its effect on the streamwise velocity: under the upstream edge of the hole, the aspiration induces a small acceleration and under the downstream edge of the hole, a deceleration. Near the plate, negative values of the streamwise velocity have even been observed, showing that the fluid turns back to enter the hole. Time-averaged spanwise velocity field (Fig. 1.17 c) shows how the fluid comes from lateral sides. The streamwise velocity field also shows the presence of two bands of low velocity on each side of the hole. The lateral aspiration visualised in Fig. 1.17 (c) creates a velocity deficit on both sides of the hole. Fig. 1.17(d) presents isocontours of  $Q$  criteria (Hunt *et al.* [82]). These criteria, based on the second invariant of the velocity gradient tensor, are used to locate vortices structures: when the  $Q$  criterion is positive, the rotation rate is superior to the strain rate. In Fig. 1.17(d), positive values of the  $Q$  criterion are observed downstream of the hole. Two counter-rotating streamwise vortices are created at the lateral edges of the hole: half diameter away from the suction wall.

A sketch in the middle of Fig. 1.17 shows the direction of rotation of the vortices. Downstream of the perforation, the spanwise spacing between the vortices increases

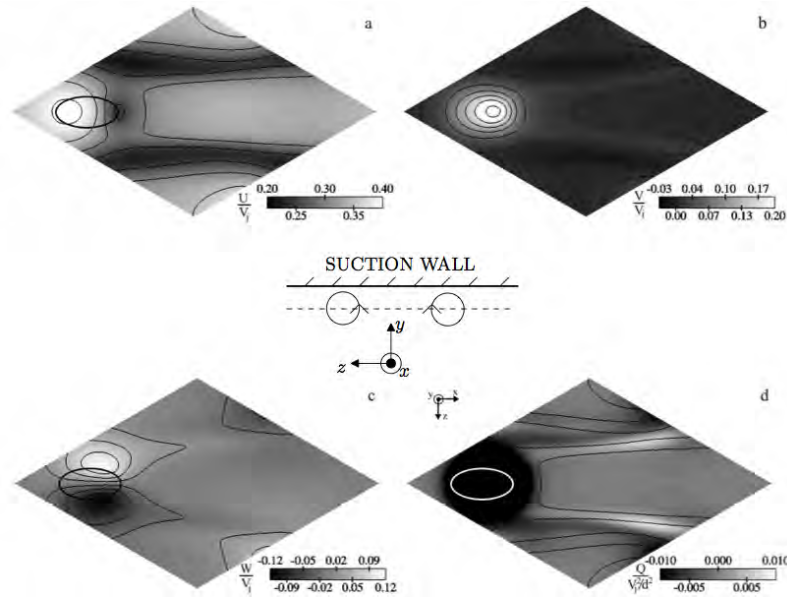


Figure 1.17: Time averaged solutions from fully resolved adiabatic computation from [125]. The thick black and white ellipses correspond to the projection of the aperture inlet. (a): Contours and isolines of time averaged streamwise velocity. (b): Contours and isolines of time-averaged normal velocity. (c): Contours and isolines of time averaged spanwise velocity. (d): Contours of  $Q$  criteria. Isolines of time averaged streamwise velocity as in (a). A schematic in the center of the figure shows the direction of rotation of the vortices; the dotted line shows the location of the cutting plane  $y = -2.5d$  displayed in this figure

as they move away from the suction wall. Figure. 1.17(a,d) also shows that the streamwise vortices delimit the low streamwise velocity zones (shown by isolines). The flow near the perforated plate on the suction side proves to be highly three-dimensional, with streamwise vortices appearing downstream of the perforation. This organisation is therefore very different from a uniform suction.

### Into the aperture:

The flow inside the hole is known to be highly inhomogeneous. Information about the in-hole flows has been obtained through numerical simulations, either by RANS (Walters & Leylek 2000 [174]) or LES (Iourokina & Lele 2006 [83] and Mendez and Nicoud [125]). In spite of the difficulty of performing direct measurements in the hole itself, experimental data can be found in the work of the group of M. W. Plesniak for normal short holes (Peterson & Plesniak [144, 145]). Mendez and Nicoud [125]) showed numerically that the maximum pressure variations are observed at the downstream edge of the hole inlet.

The LES from Mendez and Nicoud [125] and the RANS simulation from Leylek

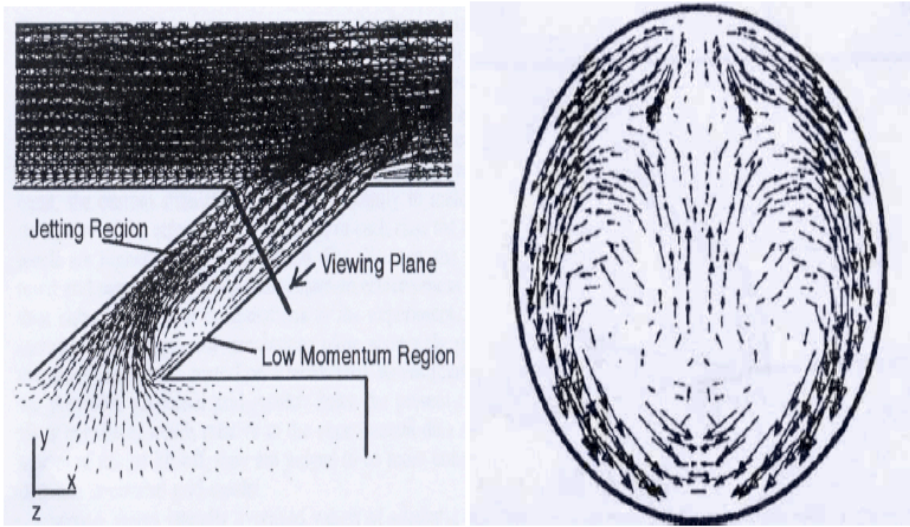


Figure 1.18: Averaged velocity field in the perforation from Leylek and Zerkle (1994) [113]. Left: symmetry plan. Right : normal slice to the perforation displaying tangential velocity.

and Zerkle [113] (see Fig. 1.18), highlight both a low velocity bubble and a tangential velocity inducing contra-rotating vortices. Indeed, the presence of a normal high velocity zone (jetting region) and a low velocity zone (low momentum region) presented on Fig. 1.18 leads to a pair of counter-rotating vortices with a horseshoe form. As presented on Fig. 1.18, sucked flow comes from all directions in a good agreement with the previous observation. The same conclusion was also drawn by [83] thanks to instantaneous structures of the flow coming from numerical simulations. Brundage and Plesniak [36] showed the presence of the recirculation bubble for both co-flow and counter-flow configuration.

Peet presented instantaneous and averaged LES fields into the aperture (see Fig. 1.19). The conclusion was that the flow is fully turbulent into the pipe but not established. The streamlines highlight the recirculation zone.

Figure 1.20 from LES of Mendez and Nicoud [125] shows contours and isolines of the three components of the time-averaged velocity over three horizontal planes ( $y = -2d$ ;  $y = d$ ;  $y = 0$ ). At the inlet of the hole, the streamwise velocity (Fig. 1.20a) is rather homogeneous, with small values still related to the suction cross-flow velocity. The vertical velocity field (Fig. 1.20b) shows small values in the upstream part of the hole inlet and high values (superior to  $V_{jet}$ ) near the downstream edge. The authors [125], linked this result with the pressure gradient distribution. As seen in the organisation of the flow on the suction side, the aperture is fed by fluid

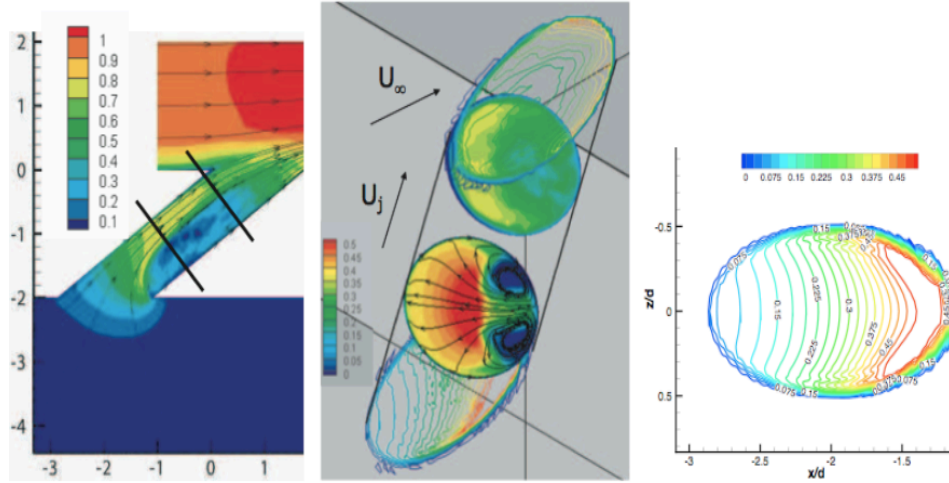


Figure 1.19: Averaged field in the perforation from Peet (2006) [143]. Left : velocity field and streamlines. Middle : normal velocity field and stream lines. Right : Normal slice at the entrance displaying normal velocity.

coming from its lateral neighbourhood: this explains the spanwise velocity field in Fig. 1.20(c), with strong values near the lateral edges of the hole.

In the middle of the hole, a strong vertical velocity forces the jet to be aligned with the direction of the hole. The jet is then flattened against the upstream wall, with smaller values of velocity magnitude near the downstream boundary. The vertical velocity is more homogeneous (Fig. 1.20e) than at the inlet (Fig. 1.20b). On the contrary, the streamwise velocity (Fig. 1.20d) shows a kidney shape characteristic of effusion cooling. The jetting region and the low-momentum region defined by Walters and Lylek (2000) [174] are confirmed by Fig. 1.20(d) and Fig. 1.20(e). The vertical and the spanwise components of the velocity allow observation of counter-rotating vortices in the aperture, localized in the low-momentum region as reported by Lylek and Zerkle (1994) [113] or Brundage *et al.* (1999) [36]. The counter-rotating vortices seem to be related to the separation at the entry of the hole. A second weaker pair of vortices can be seen at the upstream wall. This structure is due to the full coverage film cooling (FCFC) configuration. In other words, the suction field of the hole is interacting with the suction fields of upstream holes. This feature is expected to be stronger as the suction rate increases.

The structure of the flow does not change much between the half-height plane and the outlet of the hole (top row). Note however, that the kidney shape is even clearer in the streamwise velocity (Fig. 1.20 g) and the vertical velocity (Fig. 1.20 h)

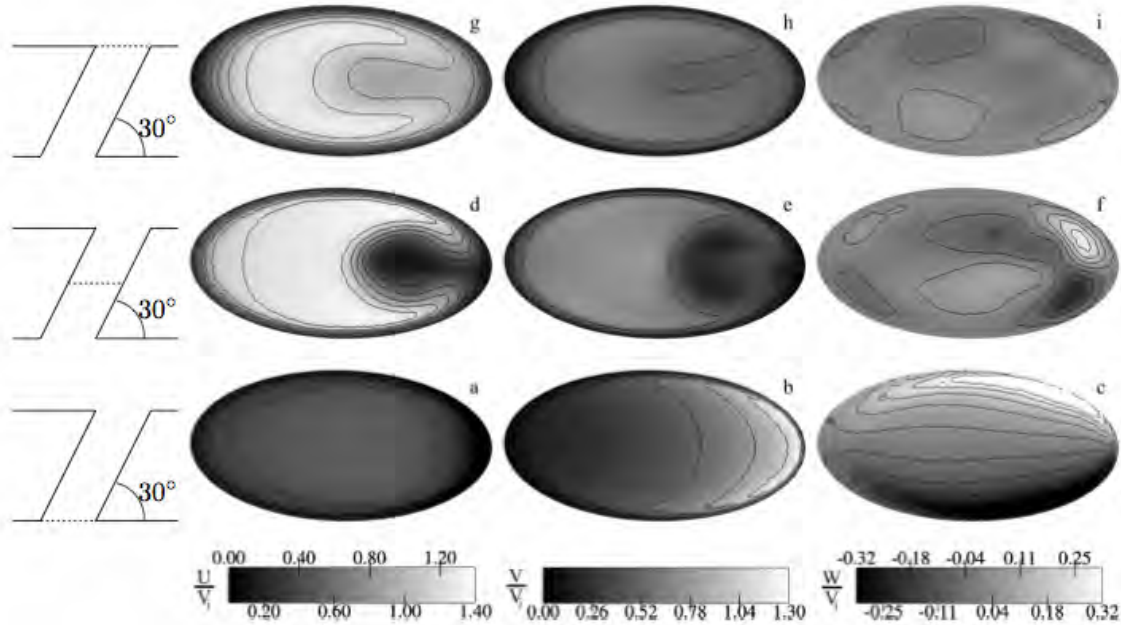


Figure 1.20: Contours and isolines of the three components of the time-averaged velocity on horizontal planes in an effusion hole. The planes are represented on the left. Top row: outlet plane. Intermediate row: half-height plane. Bottom row: inlet plane. Left column: streamwise velocity. Central column: normal velocity. Right column: spanwise velocity. [125]

is more homogeneous. As flow in the hole is highly inhomogeneous, studies where the calculation domain is cut at the outlet or even at the inlet of the hole, should be analysed with care. In addition, the complexity of the flow prevents the use of usual heat transfer correlations to assess the convective heat flux along the hole.

### Injection side:

Concerning single jets studies as illustrated by Fig. 1.21b, Fric and Roshko [67] presented a figure of Horseshoe Vortex and Counter rotating vortex pair while New *et al.* [139] showed leading edge vortices. On Fig. 1.21a, four different structures can be reported, the counter-rotating vortex pair, the jet shear layer vortices, the horseshoe vortices and the wake vortices. Tyagi and Acharya [172] used numerical simulations to highlight the hairpin structure which depends on the operating point of the flow (M and J). All these structures were extensively studied by many authors [19, 44, 67, 94, 138, 137, 136].

The counter-rotating vortex pair is the main structure of the jet in cross-flow, present in the far field and aligned with the jet. The shear layer vortices result from the Kelvin-Helmholtz instability that develops at the edge of the jet. Horseshoe

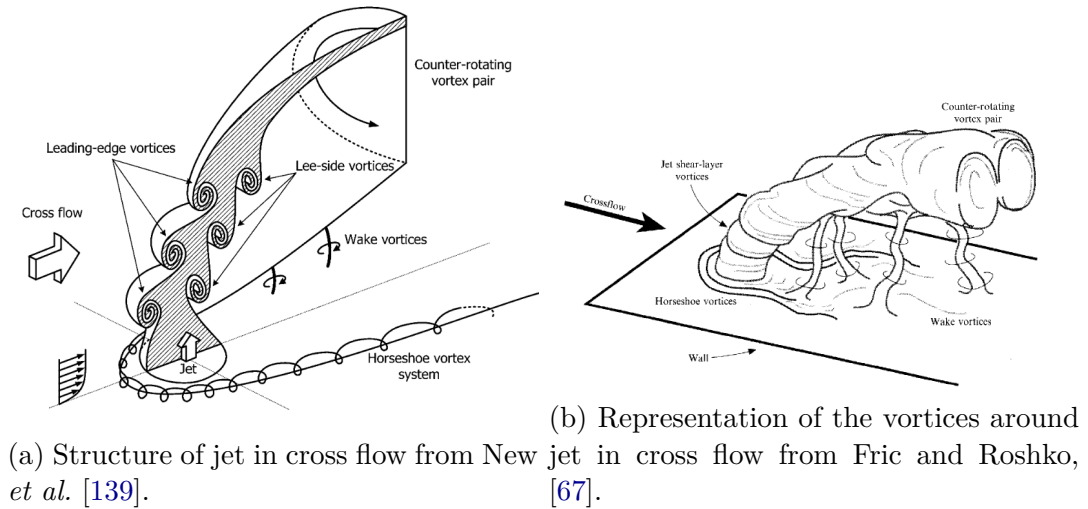


Figure 1.21: Flow on the injection side.

vortices are created by the adverse pressure gradient, the jet acting as an obstacle to the cross-flow. In the wake of the jet, with wall-normal oriented, wake vortices start from the wall and ending in the jet. Both counter-rotating and horseshoe vortices are visible in the average field. More recently, transient vortices have been detected just downstream of the hole exit, both experimentally by Peterson & Plesniak [145] and numerically by Hale, Plesniak and Ramadhyani [77] or Peet [143]. Peterson & Plesniak (2004a) refer to these vortices as downstream spiral separation node vortices to distinguish them from the unsteady "wake" vortices reported by Fric & Roshko [67].

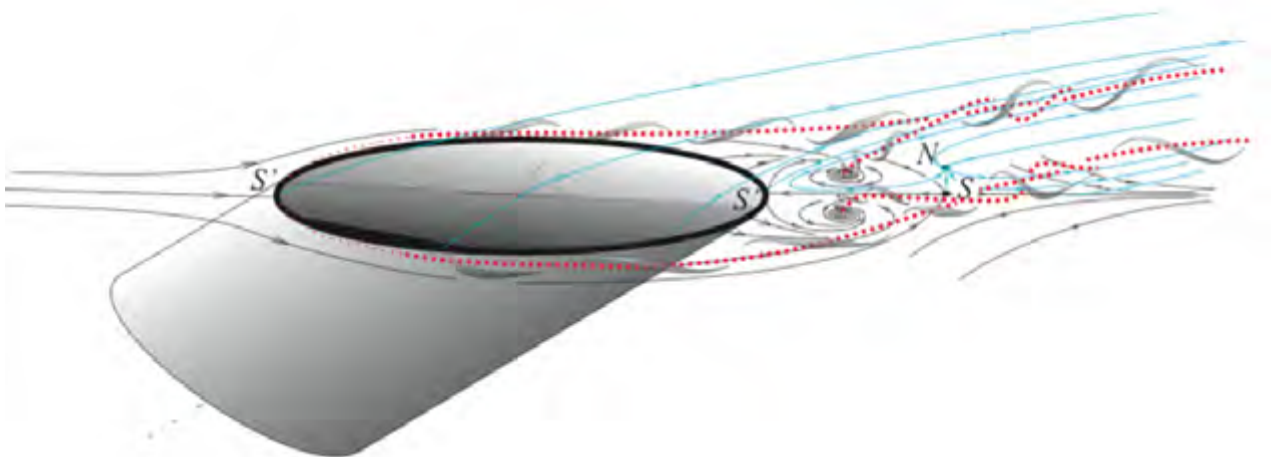


Figure 1.22: Scheme of the formation of CRVP [74]. Red dashed line represents the trajectory of CRVP.

Gustafsson [74] proposed another representation of the flow near the jet, see Fig. 1.22. Two structures are visible, a counter-rotating vortex pair just after the jet and two vortices just before the hole (beginning of the red line) in good agreement with the result of [172]. Note also that the trajectory of the jet can also be computed from equations developed from experimental results. For more detail, see [116, 117].

To the author knowledge, inner structure of a jets in cross flows interacting with others has been studied by Mendez and Nicoud [125], focused on the idealized configuration of an infinite plate, and found the main jets in cross flows features. Note that, it is difficult to get general trends from the local, configuration specific, behavior of jets in cross flows on a finite effusion plate, as depicted in the following section.

### Effusion cooling on a fine plate

As illustrated in Fig. 1.23 the effusion cooling can be decomposed into three distinct parts:

- The primary zone.
- The established zone.
- The recovery zone.

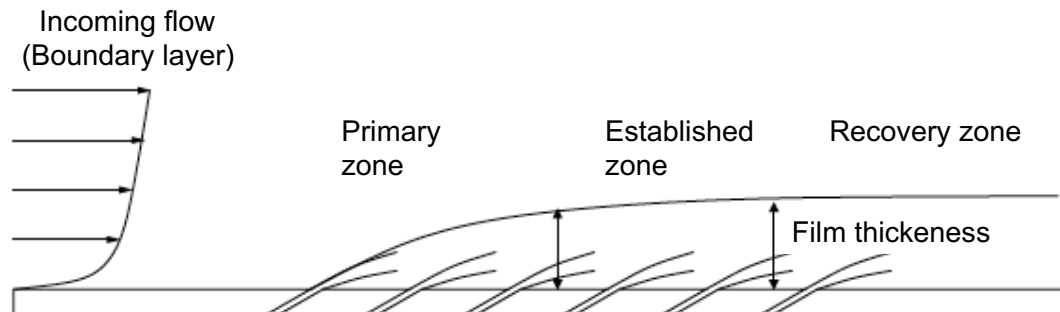


Figure 1.23: Adapted from the PhD thesis of Mendez [124]

At the beginning of a multiperforated plate, flow is very similar to a jet in cross-flow presented above. After the established zone, typically 5-7 rows, the film thickness reaches an autosimilar configuration (see Lahbib [100]). Downstream the last rows, cold air protects the wall and mixes with the main flow in the recovery zone. The length of this zone (and by the way the effectiveness of the effusion cooling) depends on  $M$  and  $J$ .

Rouvreau studied experimentally the evolution of the effusion layer, see Fig. 1.24. In his thesis, the recovery zone and thus the evolution of the layer after the multiperforated plate can be seen on Fig. 1.25.

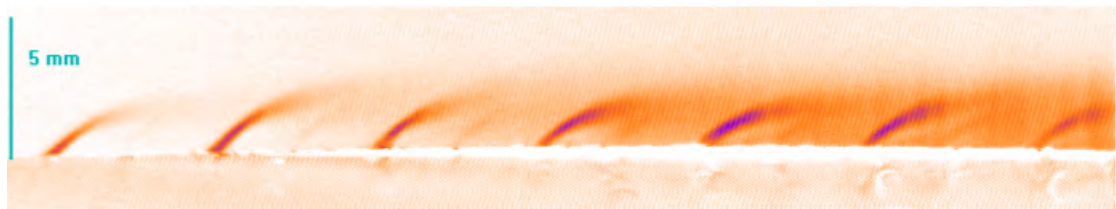


Figure 1.24: Visualisation of the film cooling using steam tracers on the multiperforated zone. Result from the PhD thesis of Rouvreau [158]

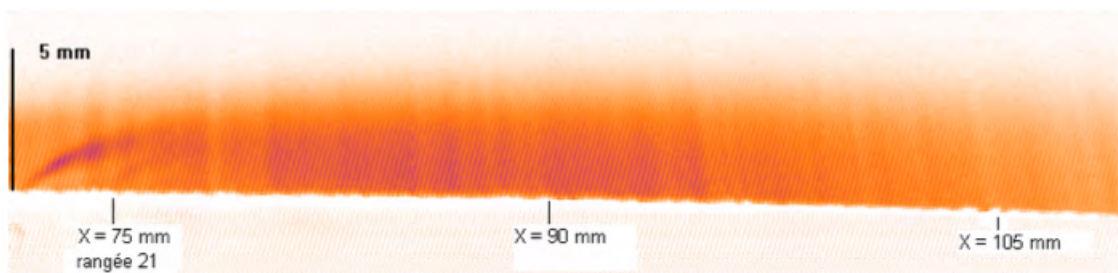


Figure 1.25: Visualisation of the film cooling using steam tracers on the recovery zone (after the multiperforated plate). Rouvreau [158].

## Chapter 2

# Numerical methods for effusion cooling

The modelling methods to compute the aerodynamic field of a full combustor are listed at the beginning of this chapter. The challenge of assessing the combustor's wall temperature, with the relevant numerical modelling methods, are then presented. Finally, axes of improvement are detailed, depicting the objectives of the thesis.

<b>2.1</b>	<b>Modeling strategies for aerodynamics</b>	<b>32</b>
2.1.1	Point mass sources	32
2.1.2	Distributed mass sources	33
2.1.3	The heterogeneous model of Rida <i>et al.</i> [155]	34
2.1.4	The heterogeneous model of Briones <i>et al.</i> [34]	35
2.1.5	The homogeneous model of Mendez and Nicoud	35
2.1.6	The heterogeneous model of Lahbib	37
<b>2.2</b>	<b>Modelling strategies accounting for thermal evolution into the solid</b>	<b>37</b>
2.2.1	Physical Aspects	37
2.2.2	Conduction	38
2.2.3	Convection	38
2.2.4	Radiation	39
2.2.5	Assessment of the effusion wall temperature	39
<b>2.3</b>	<b>Thesis objectives and organisation</b>	<b>44</b>

## 2.1 Modeling strategies for aerodynamics

As presented in the last chapter, the aerodynamics of the effusion cooling has been experimentally and numerically studied in simple configurations with a small to moderate number of perforations. However, in the case of real combustor there are more than 40 000 holes. The streamwise ( $\alpha$ ) and deviation ( $\beta$ ) angles depend on the hole's localisation, as well as the operating point (M and J) which is given by the pressure drop. At last, the operating point of the engine (different during take-off or during the cruise) controls the flow. During the design process, all these variables are optimized. With this high amount of testing parameters, experiments are expensive, with slow feedback. Numerical simulation are cheaper, with faster feedback but prone to uncertainties, approximations and errors. Notwithstanding the increasing computational resources, the simulation of an entire effusion cooled combustor still represents a challenge hardly compatible with stringent time requirements typical of the industry. To make these investigation affordable, many authors proposed approaches based on the modelling of film cooling injection to avoid the meshing of discrete holes [47, 81, 169, 37, 126, 22, 126, 155]:

- Local mass sources models (Kampe and Völker [22] and Voigt *et al.* [173])
- Point sources (Andreini *et al.* [15])
- Distributed sources (Andrei *et al.* [11])
- Uniform injection (Mendez and Nicoud [126])
- Imprinting models (Rida *et al.* [155] and Briones [34]).

### 2.1.1 Point mass sources

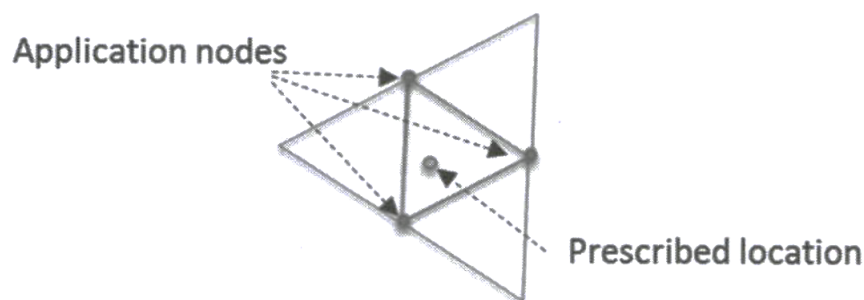


Figure 2.1: Sketch of source point application in CFX

This approach is based on local point sources to model coolant aspiration and injection. The model was developed to work with ANSYS CFX, which allows the

native application of a source points within the domain. The source is specified at a given coordinate and then it is applied within the cell that contains the assigned point (see Fig. 2.1). The model was proposed by Voigt *et al.* [173] and further developed by Andreini *et al.* [15]. According to several sensitivity analyses carried out during the development of the model, an optimal mesh sizing was identified, corresponding to two elements per hole diameter. Refer to Andreini *et al.* [15] for further details concerning the methodology.

### 2.1.2 Distributed mass sources

In 2015, the same team from UNIFI came with a second model which can be considered as a simplified approach of the one proposed by Kampe and Völker [22]. It provides distributions of the physical quantities within the injection volume, calculated from in-house developed correlations. The model proposed by Andrei *et al.* [11] is based on the application of the mass source within an injection volume (see Fig. 2.2). In fact, velocity, temperature and turbulence are calculated coherently with Andreini *et al.* [15] and applied uniformly within the injection volume. Note that this kind of modelling is sensitive to mesh refinement ([22, 11]).

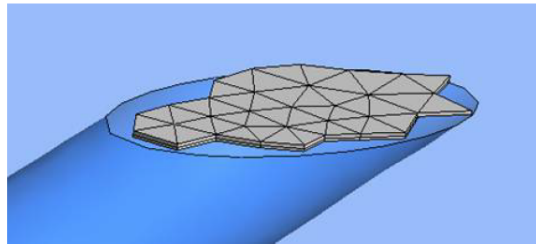


Figure 2.2: Example of distributed mass source from [122]

In 2017, Andrei *et al.* [11] had compared different shapes (see Fig. 2.3). A delimited cylinder has been proven more reliable for medium and high-blowing ratios.

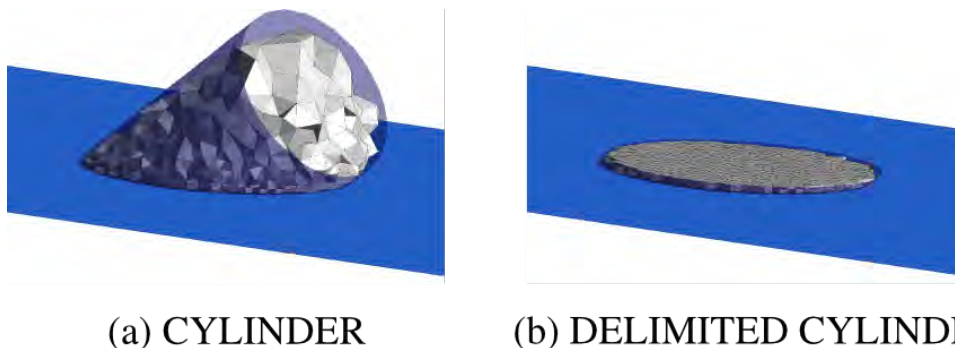


Figure 2.3: Injection volumes film cooling models with different shapes: a cylinder (a) and a delimited cylinder (b). Visualisation from [11]

### 2.1.3 The heterogeneous model of Rida *et al.* [155]

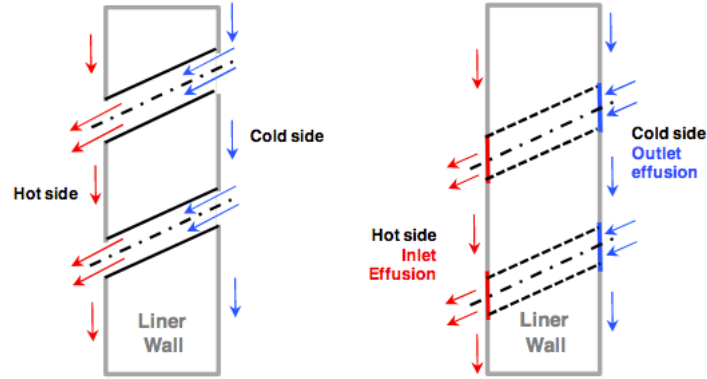


Figure 2.4: Imprinted effusion concept with inlet and outlet boundaries from [155].

Rida *et al.* [155] proposed an imprinted method which is a compromise between source sink and meshed hole. With this model, the effusion orifice pipes are removed, but the imprints on the cold and hot sides of the liner are maintained (See Fig. 2.4). Mass is extracted and injected through the imprinted boundaries based on local flow conditions (pressure differences) and orifice  $Cd$ . When talking about imprinted method, mesh has to follow the curve of the hole and thus a large number of cells into the diameter are needed to obtain a reasonable curvature (See Fig. 2.5). The imprinted effusion method ensures geometric fidelity while the removal of effusion orifice pipes allows for easier near wall meshing and eliminates the inaccuracies related to inadequate in-pipe mesh resolution. Rida *et al.* [155] claim however that the main idea behind the imprinted effusion approach is not to entail a reduction of the mesh size (gain of 20%), but rather to avoid the coarse and poor quality mesh that is usually obtained in the effusion orifices. At the end, it seems that the imprinted effusion has the same level of accuracy and fidelity as the meshed effusion approach without the burden of meshed effusion's pipes.

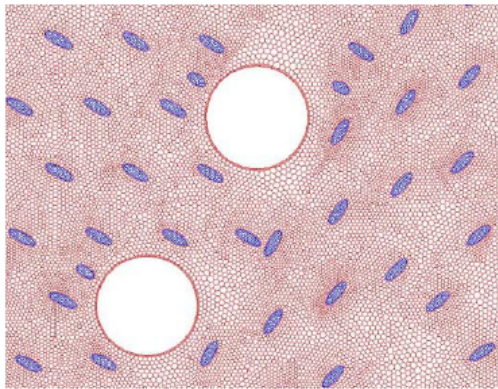


Figure 2.5: Imprinted effusion pattern on the liner wall from [155].

### 2.1.4 The heterogeneous model of Briones *et al.* [34]

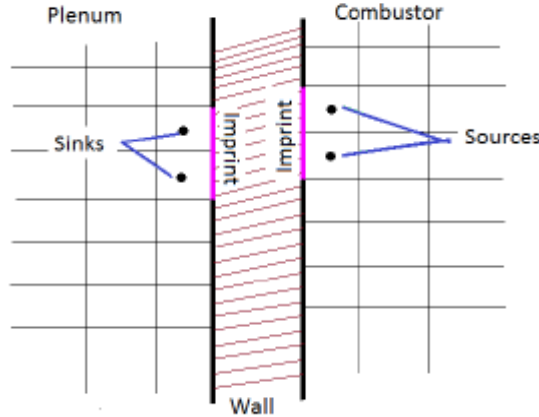


Figure 2.6: Volumetric cell-centred sources and sinks adjacent to the imprint wall boundaries in the combustor and plenum domain, respectively. From[34].

Briones *et al.* 2016 [34] developed a model to simulate combustor liners under RANS context (ANSYS Fluent). It was named PAPRICO (parallelised, automated, predictive imprint cooling). This algorithm (see Fig. 2.6) automatically identifies and computes the jet area, jet diameter, jet center from an arbitrarily partitioned mesh. PAPRICO requires the total temperature, total pressure, jet angle, discharge coefficient and orientation as an input. According to the authors, this method outperforms the hole resolved geometry because it reaches grid independence at an earlier cell count than the fully resolved geometry does.

### 2.1.5 The homogeneous model of Mendez and Nicoud

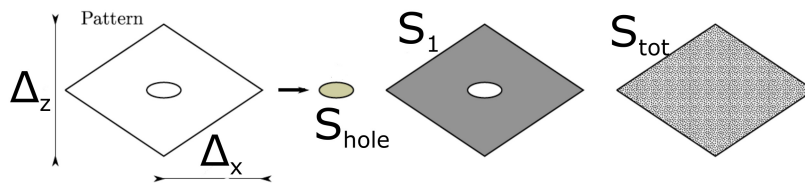


Figure 2.7: Surface of influence of one hole (diamond shape).

In order to understand the physics of the flow, Mendez and Nicoud [126] performed a wall resolved Large Eddy Simulation (LES) of a bi-periodic plate with effusion. This database showed that the viscous terms, including the classical wall shear stress  $\tau_w$ , are small compared to the inviscid flux of longitudinal momentum,  $\rho UV$ , through the holes. This questions all attempts to represent effusion flow with a modified logarithmic law based on classical wall units, where the friction velocity

$\sqrt{\tau_w/\rho}$  would be the characteristic velocity. Instead, Mendez and Nicoud [125] proposed an homogeneous adiabatic model able to represent the effect of effusion on the boundary layer structure. In this view, the multi-perforated plate is modelled as a uniform boundary so that meshes far too coarse to represent the holes can still be used. The homogeneous model [125] is now commonly used in full-scale computations of combustors with perforated liners as mentioned in the review of Savary *et al.* [162].

The homogeneous approach models the multiperforated plate as a porous plate injecting mass over its whole surface with a uniform velocity. Mendez and Nicoud [126] showed that a multiperforated plate model must represent the proper mass and longitudinal momentum fluxes across the boundary. These two quantities can be written as:

$$\int_{S_{tot}} \rho V_n^{mod}(x, z) dS = \int_{S_{tot}} \rho V_n^{jet}(x, z) dS, \quad (2.1)$$

$$\int_{S_{tot}} \rho V_n^{mod}(x, z) V_t^{mod}(x, z) dS = \int_{S_{tot}} \rho V_n^{jet}(x, z) V_t^{jet}(x, z) dS, \quad (2.2)$$

with  $\rho$  the density of the fluid.  $V_n^{mod}(x, z)$  and  $V_t^{mod}(x, z)$  are respectively the normal and tangential velocity imposed by the homogeneous model on the plate at the position  $(x, z)$ .  $V_n^{jet}(x, z)$  and  $V_t^{jet}(x, z)$  are respectively the normal and tangential velocity at the outlet of the hole for the real pipe at the position  $(x, z)$ . When integrated over the control surface  $S_{tot}$ , diamond pattern visible on Fig. 2.7, Eqs (2.1) and (2.2) become:

$$\rho \langle V_n^{mod} \rangle_{S_{tot}} = \rho \langle V_n^{jet} \rangle_{S_{hole}}, \quad (2.3)$$

$$\rho \langle V_n^{mod} \rangle \langle V_t^{mod} \rangle_{S_{tot}} = \rho \langle V_n^{jet} \rangle \langle V_t^{jet} \rangle_{S_{hole}}, \quad (2.4)$$

with  $\langle \rangle$  the associated mean surface value. It follows that the proper velocity to impose for a homogeneous description of a multiperforated liner is:

$$\langle V_n^{mod} \rangle = \langle V_n^{jet} \rangle / \sigma, \quad (2.5)$$

$$\langle V_t^{mod} \rangle = \langle V_t^{jet} \rangle, \quad (2.6)$$

The homogeneous model allows to represent the main effects of the effusion, with a proper injected mass and momentum flux (see Fig. 2.8). It gives very good results and allows to handle coarse meshes typical in aeronautical engines. However the limit of this model is the loss of numerical convergence: no improvement in the mixing representation when resolution increase.

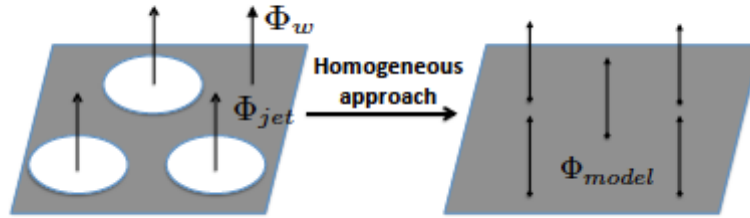


Figure 2.8: Homogenization of the velocities over the plate surface from [100].

### 2.1.6 The heterogeneous model of Lahbib

During his PhD thesis, Lahbib [100] developed the first heterogeneous model for Large Eddy Simulation of effusion cooling inspired from Mendez and Nicoud homogeneous model. He proposed to thicken the injecting surface if the mesh is not sufficient fine. The first results showed good agreements with a reference DNS. Mass and momentum balances agreed reasonably well and flow profiles were satisfactory. However, further applications on other configurations and mesh resolutions exhibited momentum errors for the coarse meshes. This became prominent on a complex academical configuration, yielding major flow disturbances due to particularly unfavorable resolution and  $M, J$  combination.

All these models focus on the aerodynamic of the flow with an adiabatic hypothesis. The following section presents models which take into account heat transfers, assuming for the overall wall temperature.

## 2.2 Modelling strategies accounting for thermal evolution into the solid

### 2.2.1 Physical Aspects

Heat transfer is the physical act of thermal energy's exchange between two systems. The amount of thermal energy available is determined by its temperature. On a molecular scale, the kinetic energy is directly linked to thermal energy. Regions that contain higher kinetic energy transfer the energy to regions with lower kinetic energy. Simply put, heat transfer can be grouped into three broad categories: conduction, convection, and radiation.

### 2.2.2 Conduction

Conduction refers to the transfer of energy through the movement of particles in contact with each other. In the solid this phenomenon is caused by photons and free electrons while in fluid it is due to the molecular movement. The process of heat conduction depends on the following factors: temperature gradient, cross-section of the material, the length of the travel path, and physical material properties. The temperature gradient is the physical quantity that describes the direction and rate of heat flux. Heat flux goes from hot to cold or, as stated before, higher to lower kinetic energy. Once there is thermal equilibrium between the two temperature differences, the thermal transfer vanishes.

Fourier's law [63] gives an empirical relationship between the conduction rate in a material and the temperature gradient in the direction of energy flow. For a unidirectional conduction process this observation may be expressed as:

$$\dot{q} = -\lambda \nabla T, \quad (2.7)$$

with  $\dot{q}$  the heat flux (W/m<sup>2</sup>),  $\nabla T$  the temperature gradient (K/m), and  $\lambda$  the thermal Conductivity (W/m/K).

### 2.2.3 Convection

When a fluid, such as air or a liquid, is heated and travels away from the source, it carries thermal energy along. This type of heat transfer is called convection. At the molecular level, the molecules expand thanks to added thermal energy. As the temperature of the given fluid mass increases, the volume of the fluid must increase by the same factor. This effect on the fluid causes a displacement. As the immediate hot air rises, it pushes denser, colder air down. This series of events represents how natural convection currents are formed.

The equation for convection rates was derived from an empirical observation of convective cooling of hot bodies made by Isaac Newton in 1701. He stated that "the rate of loss of heat by a body is directly proportional to the excess temperature of the body above that of its surroundings." It can be expressed as follows:

$$\dot{q} = h(T_{adiab} - T_{ref}), \quad (2.8)$$

with  $h$  the Heat Transfer Coefficient (W/m<sup>2</sup>/K),  $T_{adiab}$  the adiabatic temperature (K) and  $T_{ref}$  the reference temperature (K).

## 2.2.4 Radiation

Thermal radiation generates electromagnetic waves. These waves carry the energy away from the emitting object, through a vacuum or any transparent medium. All materials radiate thermal energy based on their temperature. The hotter an object, the more it will radiate. The sun is an example of heat radiation that transfers heat across the solar system. At normal room temperatures, objects radiate as infrared waves. The temperature of the object affects the wavelength and frequency of the radiated waves. As temperature increases, the wavelengths within the spectra of the emitted radiation decrease. Thermal radiation is calculated by using the Stefan-Boltzmann law (1879):

$$\dot{q} = \epsilon \sigma T^4, \quad (2.9)$$

with  $\epsilon$  the emissivity coefficient of the object (between [1-0], one corresponds to a black body).  $\sigma$  corresponds to the Stefan-Boltzmann Constant and is equal to  $5.6703 \cdot 10^{-8}$  (W/m<sup>2</sup>/K<sup>4</sup>).

## 2.2.5 Assessment of the effusion wall temperature

All the study and models presented in the previous part focus on the aerodynamic of the flow usually using adiabatic walls. As presented in section 2.1 and 1.5, the aerodynamic of the jets is quite complex. The Kader laws [90] can be used to compute the plate temperature from the flow, useful when dealing with two channels in parallel but this approach does not take into account the mixing of the effusion jets. The present part lists methods to assess the effusion wall temperature.

### Analytical and empirical models

Analytical 1D models have been first proposed in the literature to assess wall film cooling for flat walls [119, 72]. However, they lack of precision due to the numerous assumptions. That is why some correlations has been created from either experiments or resolved numerical simulations [104, 130, 41, 49, 108, 45].

Florenciano and Bruel [61] have compared the output of several correlations for heat transfer coefficients on the injection side ( $h_{hot}$  [ $W m^{-2} K^{-1}$ ]) with respect to a fully coupled, holes resolved simulation where both the fluid and solid domains were accounted for. Heat transfer coefficients are often used to represent the wall heat flux  $\Phi$  thanks to the Newton relation  $\Phi_{hot} = h_{hot} (T_{ref} - T_{wall hot})$  and are expressed through (experimental) correlations based on non-dimensional numbers. Regarding effusion flows for example, Cottin [45] proposed for the injection side:

$$h_{hot} = \rho_{hot} C_{p,hot} U_{hot} S_t, \quad (2.10)$$

with the Stanton number approximated by:

$$S_t = 0.00675 \left( \frac{V_{jet}}{U_{hot}} \right)^{0.67} \left( \frac{\rho_{jet}}{\rho_{hot}} \right)^{1.22}, \quad (2.11)$$

$C_{p,hot}$  stands for the specific heat capacity of the air in the hot side, and  $S_t$  is the Stanton number. Florenciano and Bruel [61] proposed another expression to evaluate the Stanton number dedicted to high momentum and blowing ratios flows ( $M \approx 8$  and  $J \approx 30$ ):

$$S_t = 0.00241 \left( \frac{V_{jet}}{U_{hot}} \right)^{0.67} \left( \frac{\rho_{jet}}{\rho_{hot}} \right)^{1.22}. \quad (2.12)$$

Cottin [45] also proposed correlations to assess the Nusselt number for the suction side (Eq. 2.13) and the hole's inner surface (Eq. 2.14):

$$N_{u,cold} = 0.023 Re_{Dh}^{0.8} Pr^{0.33} \left( 1 + 0.5 \frac{V_{jet}}{U_{cold}} \right)^{0.77}, \quad (2.13)$$

$$N_{u,hole} = 0.02775 Re_d^{0.8} \left( Re_d^{0.17} \left( \frac{L}{d} \right)^{-0.8} \right)^{0.275}. \quad (2.14)$$

The Reynolds number ( $Re_{Dh}$ ) used to compute the Nusselt number on the cold side is based on the hydraulic diameter and the bulk velocity [41, 61].  $Pr$  denotes the Prandlt number. The Nusselt number into the holes takes into account the aspect ratio  $L/d$  (*i.e.* the perforation length-to-hole diameter ratio) and the Reynolds number based on the hole diameter [61]. Using these Nusselt numbers, the heat transfer coefficients can then be recovered using the relation  $h = N_u \lambda / L_{ref}$ , with  $\lambda$  the thermal conductivity of the fluid and  $L_{ref}$  a characteristic length. For example, Florenciano and Bruel [61] took for characteristic length the average of the minor and major axis of the ellipse in the middle section of the hole.

Assuming that appropriate correlations for the heat transfer coefficients are available for the suction ( $h_{cold}$ ), the injection sides ( $h_{hot}$ ) and the inner hole of the plate ( $h_{hole}$ ), the corresponding heat fluxes can then be computed from  $\Phi_{cold} = h_{cold} (T_{ref\ cold} - T_{wall\ cold})$ ,  $\Phi_{hot} = h_{hot} (T_{ref\ hot} - T_{wall\ hot})$  and  $\Phi_{hole} = h_{hole} (T_{ref\ hole} - T_{wall\ hole})$  respectively. As the Biot number of the plate is very small ( $Bi = h e / \lambda_s < 10^{-2}$  in [61]), the temperature variations across the plate thickness can be neglected. Then, balancing the three heat fluxes at steady state allows to compute the wall temperature  $T_{wall}$  (see Section 6.4 for details). However the values of  $T_{ref}$  have to be determined on both sides and into the holes, as highlighted by Grenard and Scherrer [72]). Such quantity is not trivial to assess since the temperature on the hot side results from the mixing between the cold jets and the cross flow of hot gases.

### Numerical models from UNIFI

The numerical computation of an entire combustion chamber involves a separation of scale. On the one hand, the size of an engine is about one meter, on the other hand, multiperforated holes have a diameter of half a millimeter. Thus, it is impossible to resolve the flow scales with the present resources and orifices have to be modeled as well as heat transfer.

Andreini *et al.* [14] proposed a method to study heat transfer on complex geometries, which relies on porous boundary condition to model the fluid behaviors. Two computations are needed. A first one with adiabatic boundary conditions assesses the convective temperature thanks to a flux balance. A second flux balance from a computation with isothermal boundary conditions gives the heat transfer coefficient.

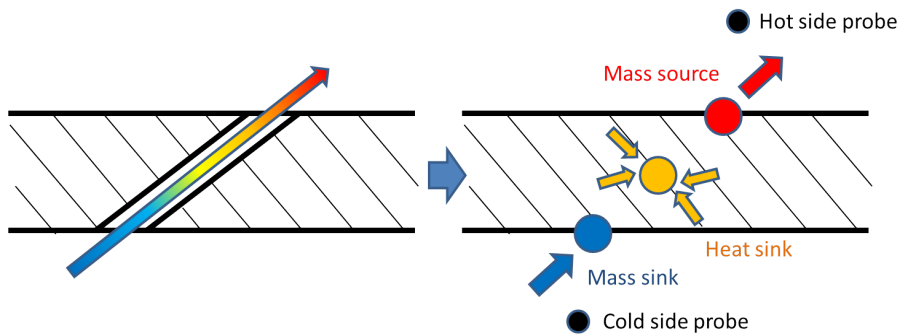


Figure 2.9: Conceptual representation of effusion hole modeling from [16].

To gain precision, Voigt *et al.* [173] proposed a point mass source model which allows to perform a conjugate heat transfer (CHT) simulation without dealing with the effusion pipe. Since this pipe is modeled by a mass source and a mass sink it drastically reduces the computational cost. Andreini *et al.* [16] improved this model thanks to a local pressure drop formulation allowing the automatic calculation of the mass flow. This model called SAFE (Source based effusion model), is based on the replacement of each effusion hole with a mass sink on the cold side of the plate and a mass source on the hot side, whereas convective cooling within the perforation is accounted for with a heat sink (see Fig. 2.9). The innovative aspect of the work is the automatic calculation of the mass flow through each hole, obtained by run-time estimation of isentropic mass flow with probe points, while the discharge coefficients are calculated through an in-house developed correlation. In the same manner, the heat sink is calculated from a Nusselt number correlation available in literature for short length holes. This method was implemented in a RANS solver ANSYS CFX and gives satisfactory results as demonstrated in Andreini *et al.* [17].

### Coupled methods to simulate a multiperforated plate

A hole-resolved simulation of a combustor is still a challenge. Numerical computations including conduction in the solid and radiation are even more expensive in terms of CPU resources. Still, academic runs can give usefull insight for modelling.

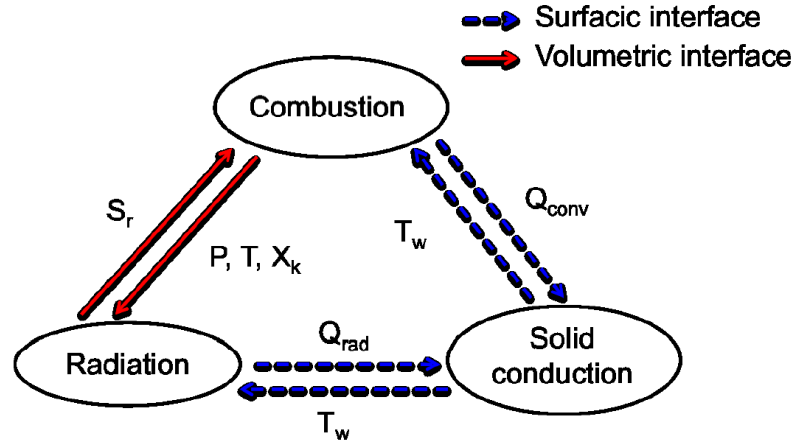


Figure 2.10: Representation of the 3 codes coupling used by Berger *et al.* [24]

Lahbib *et al.* [101] and Florenciano and Bruel [62] used the same solvers and method to perform a conjugate heat transfer large eddy simulation of an academic test case. It was a 12 holes's resolved case, computed with a LES solver. Conduction in the solid as well as heat transfers excepted radiation was solved into the fluid. Both used the coupling strategies developed by [54, 87, 86]. The strategy is presented in Section 6.1.2.

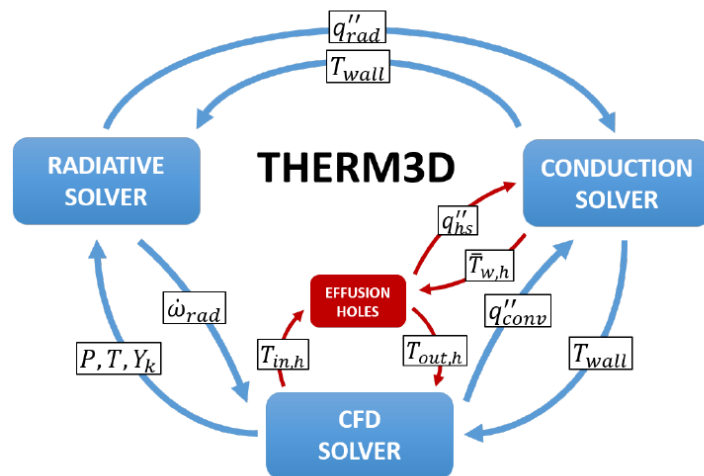


Figure 2.11: Representation of the THERM3D methodology, from [17].

The effect of radiation has also been studied. Mazzei *et al.* [123] used a 3-code coupling between a fluid, a solid and a radiation solver. Berger *et al.* [24] used the same methodology but solved the fluid dynamics with a LES solver. In the latter, effusion holes were modelled with a homogeneous model from Mendez and Nicoud [125] the adiabatic temperature was approximated by a probe near the wall estimated thanks to Cottin’s correlation presented above. The methodology of Berger *et al.* [24] is sketched on Fig. 2.10.

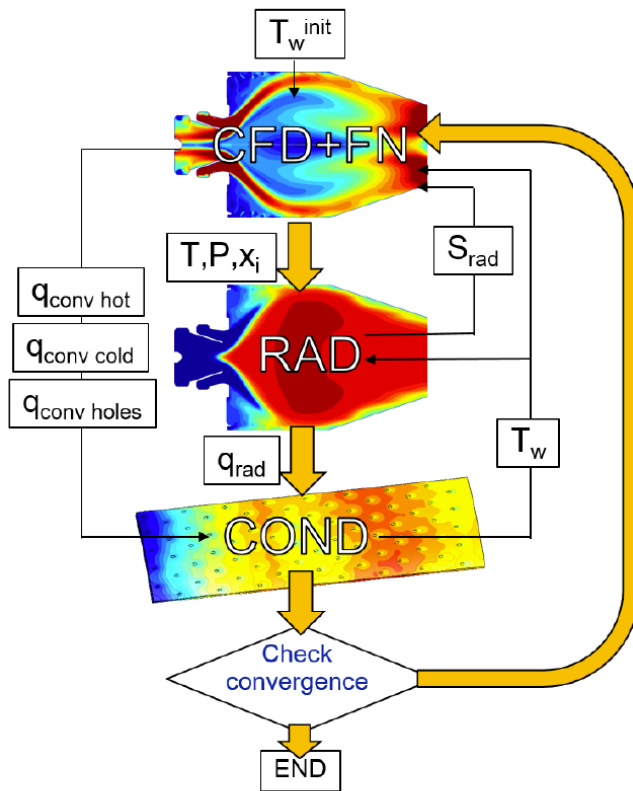


Figure 2.12: Example of THERM3D application.

The Team of Unifi developed another coupling methodology named THERM3D (see Figs. 2.12 and 2.11) applied when an accurate prediction of the metal temperature 3D distribution is required, for example during detailed design of combustor’s liners. The aerothermal flow field of the combustor is computed employing a RANS simulation. The key concepts of the methodology are presented in [123] using ANSYS®CFX code. The interaction among the simulations is accomplished according to [54, 24, 25]. The three simulations run in a sequential manner but all of them are simultaneously loaded. The queues and exchange of data are handled by User Defined Functions (UDFs) [1, 57].

The THERM3D procedure is composed of two different internal loops, as shown in Fig. 2.12. An inner loop exploits a UDF (i.e. “effusion holes” block in Fig. 2.12) to

compute and set the hole's outlet gas temperature based on a continuous updating of hole inlet gas temperature. This inlet temperature is given back to the UDF in order to compute mean gas temperature into the holes for molecular properties estimation. An outer loop, instead, performs the metal temperature evaluation that is given back to the CFD solver as wall temperature distribution and to the UDF as mean hole wall temperature. The first guess CFD solution is obtained assuming a uniform metal temperature distribution.

## 2.3 Thesis objectives and organisation

When looking into the literature, existing models to simulate the aerodynamics of effusion cooling in industrial combustors are no more satisfactory in the Large Eddy Simulations context. Indeed in 2018, the grid resolution is close to the hole diameter. A homogeneous approach cannot take advantage of such precision. The objective of this work is to improve the existing models, but also ensure their applicability on very high resolutions, even if these are not affordable today.

During this thesis, the first goal is to improve the approach of Lahbib. A systematic monitoring of mass and momentum balance for all resolutions is required. This model must give results as well as the homogeneous one when the mesh is coarse and better results when the mesh is finer. This development is presented in Part II. The bibliographical review showed that studies with deviation angles are rare and numerical models are generally not evaluated in these cases. A second point is therefore the production of a relevant database for effusion cooling with deviation.

Wall temperature of the effusion plate is the final objective. The available methods are either too expensive, and therefore not adapted to the engine design process, or need approximations that question the relevance of the results. During this thesis, the second goal is to propose a method usable and reliable, by taking advantage of the specificity of effusion devices found in aeronautical chambers. The description of the methodology, named "Adiab2colo", is given in Part III.

Lahbib stated that hole resolved effusion cooling will not be available before 2050. The present work will try to prove that this assertion is too pessimistic, as it disregarded a potential mesh adaptation technique focused on effusion. In Part IV, a mesh adaptation strategy is suggested and tested to increase substantially the effusion resolution with a reasonable over-cost. Thanks to these new meshes, the aerodynamic and thermal model convergence is tested, showing their applicability on high resolutions.

The goal of this PhD is also to prove the applicability of all the proposed methods on complex cases for the design phase. That is why, after being validated on academic test cases, for each method, the application on a real combustor is presented.

## Part II

# Aerodynamic modelling

## Chapter 3

# The thickened-hole model

In the following chapter, the adiabatic aerodynamic effusion model started from Lahbib and developed during this thesis is detailed. It has been published in Flow, Turbulence and Combustion journal (FTaC) [29] and presented at the INCA conference [27]. Note that this formulation is already in use at Safran Helicopter Engine for the design phases since 2017.

<b>3.1</b>	<b>Hole resolution</b>	<b>47</b>
<b>3.2</b>	<b>Presentation of the thickened-hole model [29]</b>	<b>48</b>
3.2.1	Distribution function in the hole frame	48
3.2.2	Projection on the mesh	49

### 3.1 Hole resolution

When performing numerical simulations of multiperforated plates, the important parameter is the aperture-to-mesh ratio ( $R$ ). It allows to characterise the corresponding mesh resolution constraints:

$$R = \frac{d}{dx}, \quad (3.1)$$

where  $d$  is the diameter of the perforations and  $dx$  the typical mesh size. These values are not absolute but to ease the classification, we can consider that a coarse mesh would correspond to  $R \leq 1$  while when  $R \geq 16$  the mesh is called fine. Note however, that more cells could be needed to resolve the jet in cross flow as mentioned by Mendez and Nicoud [126]. Typical values of  $R$  are illustrated on Fig. 8.1.

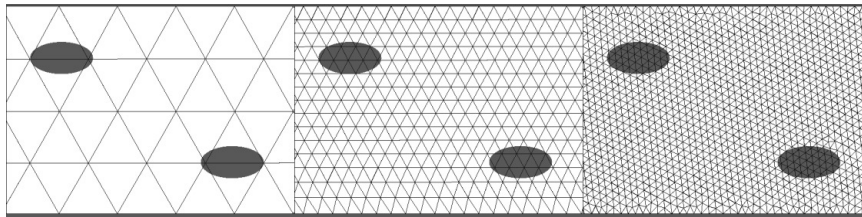


Figure 3.1: Superposition of multiperforation holes over different grids. Left:  $R=0.5$ . Middle:  $R=2$ . Right:  $R=4$

In aeronautical combustor condition, jets are at low Reynold and Mach numbers (Mach $<0.3$  and Re $<2000$ ). In these cases, when  $R \geq 16$ , the actual geometry, including effusion pipe, can be computed without modelling and the effect of the multi-perforated liner is obtained by simply using the flow equations. This kind of simulation has been carried out with RANS approaches [133] but is not expected for LES solvers before 20 years [100]. At the opposite, when  $R \leq 1$ , the liner must be modelled as a homogeneous surface; apertures are not represented. In this case, either both injection and suction sides can be computed or just the injection side. In both cases, the state-of-the-art is then to use the homogeneous model of Mendez and Nicoud [125] where the coolant flux is homogeneously injected on the whole boundary. This model has indeed proven reliable in many configurations [97]. Its drawbacks are, however, a bad prediction of the mixing process close to the wall and no benefit from better mesh resolution.

Thanks to the increasing available computational resources, typical mesh resolutions used for industrial LES predictions of actual burners already reach  $R$  above unity near the wall and are a clear asset to improve the near wall mixing in a LES context. This, however, goes with a modelling effort since the homogeneous formulation cannot benefit from such improved resolutions. This approach should then be replaced by a better one, based on a heterogeneous formulation. This is why a new

model, called thickened-hole model has been proposed [29]. It is based on the combination of an heterogeneous approach where holes are projected on the mesh and a homogeneous model where mass and momentum are conserved. This approach is local since it self-adapts the model as a function of the mesh resolution ( $R$ ).

## 3.2 Presentation of the thickened-hole model [29]

The homogeneous model represents the main effects of the effusion (proper injected mass and momentum flux), as detailed in [126]. At the same time, representing the heterogeneity of the injection through discrete holes would be beneficial in LES where macro mixing plays a key role. Since typical mesh resolutions are not sufficient to represent the intra jet flow, a basic idea is to make the apertures thicker so that the grid resolution can represent the modified holes. From the analysis of Mendez and Nicoud [125], (who considered infinitely thickened-holes in a sense), thickening the aperture modifies the momentum flux and must be compensated.

The next step is then to limit the Mendez and Nicoud [125] formulation (Eqs. (2.5), (2.6) ) to the region corresponding to each thickened-hole. Outside of this region, a wall law model, suitable for an impermeable solid plate, is applied. It uses a two layer logarithmic law along with a slip condition applied as detailed in [84]. In order to define the injection region, a distribution function is necessary. The easiest way to define the distribution function is to use a local coordinate  $(u_r, u_\theta, z_{local})$  where  $z_{local}$  is the axis of the hole (direction of the jet) with a cylindrical point a view  $(r, \theta, z)$ .

### 3.2.1 Distribution function in the hole frame

When using local coordinate and cylindrical mark, the distribution function, local to the hole, is only a function of the distance from the hole axis ( $r$ ). Indeed, it is independent from  $\theta$  and  $z_{local}$ . It can be written as follows:

$$f(r) = 0.5 \left( 1 - \tanh \left( \frac{r - 0.5d\Gamma}{\beta_{stiff} dx} \right) \right). \quad (3.2)$$

In Eq (3.2),  $\Gamma$  is the thickening factor, defined as  $\Gamma = \text{Max} \left( \frac{E}{R}, 1 \right)$ , where  $E$  is the minimum number of cells per hole diameter, defined by the user. Note that for non-uniform grids; the mesh size  $dx$  used to compute the  $R$  ratio is the cell size of the closest cell to the center of the hole. The parameter  $\beta_{stiff}$  is introduced to control the stiffness of the distribution function and avoid numerical stability issues. It is also user-defined. Preliminary experiences indicate that  $E = 3$  and  $\beta_{stiff} = 0.1$  are adequate values. At this step the function is independent on the mesh.

### 3.2.2 Projection on the mesh

On each node of the boundary wall, the distance from the axis ( $r$ ) is evaluated. This allows to compute the value of the distribution function which is then assigned to the corresponding node. Since the axis  $z_{local}$  can be, not normal to the boundary, the projected hole can be an ellipse. Note that the value of the distribution function  $f(\vec{x})$  is equal to unity in the hole region and zero outside (see Fig 3.2):

A numerical porosity is then introduced as:

$$\sigma_n = \frac{S_{hole}}{S_{num}} = \frac{S_{hole}}{\int_{S_{tot}} f(\vec{x}) dS}, \quad (3.3)$$

where  $S_{num}$  corresponds to the injection surface, that is equal to the surface of the thickened hole through which the jet velocity profile is imposed;  $\sigma_n$  is local and associated to each hole. It ranges between 1 when the hole is perfectly represented and  $\sigma$ , the physical porosity used in [125], when coolant air is injected on the whole plate in a homogeneous way. When using the thickened-hole model, the velocity applied on the boundary, noted  $V_n^{thick}(\vec{x})$  and  $V_t^{thick}(\vec{x})$  for the normal and tangential directions respectively, follow the expressions:

$$V_n^{thick}(\vec{x}) = A_n f(\vec{x}), \quad (3.4)$$

$$V_t^{thick}(\vec{x}) = A_t f(\vec{x}), \quad (3.5)$$

where  $f(\vec{x})$  introduced the spatial heterogeneity.  $A_n$  and  $A_t$  are constant values and are determined by the following equations. The mass conservation corresponding to the integration of the normal velocity on the control surface  $S_{tot}$  for the thickened hole and for the real jet through the plate allows to find  $A_n$ :

$$\int_{S_{tot}} \rho A_n f(\vec{x}) dS = \int_{S_{tot}} \rho V_n^{jet}(\vec{x}) dS, \quad (3.6)$$

$$A_n = \frac{\langle V_n^{jet} \rangle S_{hole}}{\int_{S_{tot}} f(\vec{x}) dS}, \quad (3.7)$$

Momentum conservation then allows to find  $A_t$ :

$$\int_{S_{tot}} \rho A_n f(\vec{x}) A_t f(\vec{x}) dS = \int_{S_{tot}} \rho V_n^{jet}(x, z) V_t^{jet}(\vec{x}) dS, \quad (3.8)$$

$$A_t = \langle V_t^{jet} \rangle \frac{\int_{S_{tot}} f(\vec{x}) dS}{\int_{S_{tot}} f^2(\vec{x}) dS}. \quad (3.9)$$

When the mesh resolution is enough to properly represent the velocity field inside the hole,  $R > E$ , this model is equivalent to a heterogeneous model without

thickening. If  $R < E$  apertures are thickened (See Fig 3.2). Finally, when  $R \ll E$  the model degenerates to a homogeneous model. Note that no turbulence activity or equivalently turbulence shear stress is added on the injection surface of the boundary. Indeed it would be complex to add such terms since the jet size is variable (injection surface  $S_{num}$  depends on the thickening) and since the RMS field [126] is quite complex in terms of profile, it can not be imposed with only few cells.

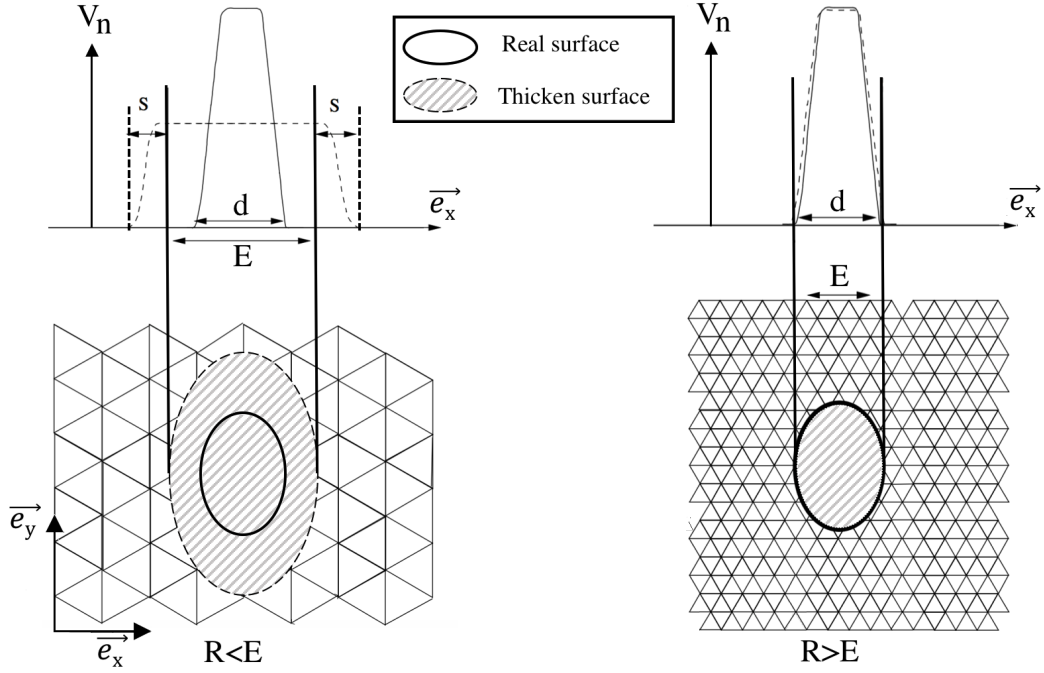


Figure 3.2: 1D representation of the normal velocity profile (top figures) and representation on a 2D mesh of the injecting surface (bottom figures) for  $R=2$  (left) and  $R=4$  (right).

In order to compute the final value of  $V_n^{thick}(\vec{x})$ ,  $V_t^{thick}(\vec{x})$  and  $f(\vec{x})$ , an accumulation (sum) of the value computed independently for each hole on each node is performed.

In the following section the performance of the thickened-hole model is evaluated as a function of the grid resolution on two different setups, each one including two variants in the multiperforation's hole arrangement.

---

## Chapter 4

# Thickened-hole model applied on four academic cases

In the following chapter, the proposed effusion model is applied on two configurations, the Maveric plate and the Michel tube. Each has a longitudinal ( $\beta = 0^\circ$ ) and a transverse version ( $\beta = 90^\circ$ ). For the Maveric test case a database for each deviation angle was created thanks to a hole-resolved computation. Numerical softwares used to create the database are presented. In the case of Michel tube, the database comes from experimental results. Numerical results using the thickened-hole and the homogeneous models are tested with various grid resolutions. Results on the Maveric test case without deviation have been published in [29].

---

<b>4.1</b>	<b>Maveric test case</b>	<b>52</b>
4.1.1	General presentation of the Maveric test case	52
4.1.2	Description of the numerical softwares	56
4.1.3	Maveric plate with longitudinal cooling	57
4.1.4	Maveric plate with transverse cooling	63
4.1.5	Feasibility of a two-side effusion simulation with the thickened-hole model	68
<b>4.2</b>	<b>Michel tube test case</b>	<b>70</b>
4.2.1	Experimental setup	70
4.2.2	The longitudinal Michel tube cooling case	72
4.2.3	Michel tube with transverse cooling	77
<b>4.3</b>	<b>Thickened-hole model capabilities</b>	<b>80</b>

---

Two cases have been chosen to validate the model, both have a high blowing and momentum ratio typical of aeronautical combustion chambers :

- One without experimental results but a very controlled case where fully resolved simulation can be performed. This first case is denoted Maveric test case. Two geometrical hole orientations have been used, one without deviation angle ( $\beta = 0^\circ$ ) and one with a deviation angle ( $\beta = 90^\circ$ ).
- One with experimental results and more complex. It contains many more apertures and the multiperforated wall is curved. This second test case is denoted Michel tube. It also includes two geometrical variants for the hole cooling orientation: a longitudinal ( $\beta = 0^\circ$ ) and a transverse one ( $\beta = 90^\circ$ ).

The four operating points considered are displayed in table 4.1.

Case	Deviation angle	M	J	Re	Mach
Maveric plate with longitudinal cooling	$\beta = 0^\circ$	8.4	31	2700	0.26
Maveric plate with transverse cooling	$\beta = 90^\circ$	8.4	31	2700	0.26
Michel tube with longitudinal cooling	$\beta = 0^\circ$	8.7	76	1200	0.16
Michel tube with transverse cooling	$\beta = 90^\circ$	8.7	76	1200	0.16

Table 4.1: Characteristics of the four test cases.

## 4.1 Maveric test case

### 4.1.1 General presentation of the Maveric test case

This section is extracted from two publications written during this PhD thesis [29, 30]. However, more precisions are given in the present manuscript.

The first studied geometry is denoted Maveric plate. It is inspired from the Maveric set up built and studied by Petre *et al.* [147], Miron [132] and Florenciano [60]. It consists of two parallel channels communicating through 144 converging holes disposed in 12 staggered rows as shown in Fig. 4.1 and described in [101, 29].

Due to experimental constraints, the holes were upscaled (12.5:1) compared to typical apertures of perforated liners used in combustors. The numerical Maveric setup recovers the actual hole diameter of 0.4 mm and aims at reproducing geometrical and operating conditions more representative of real combustor liners than other databases available in the literature. All the geometric parameters: The hole diameter on the injection side  $d$ , the longitudinal ( $\Delta x$ ) and spanwise ( $\Delta z$ ) distances between two consecutive holes, the injection angle  $\alpha$  and the thickness of the plate  $e$ , are given in Table 4.2.

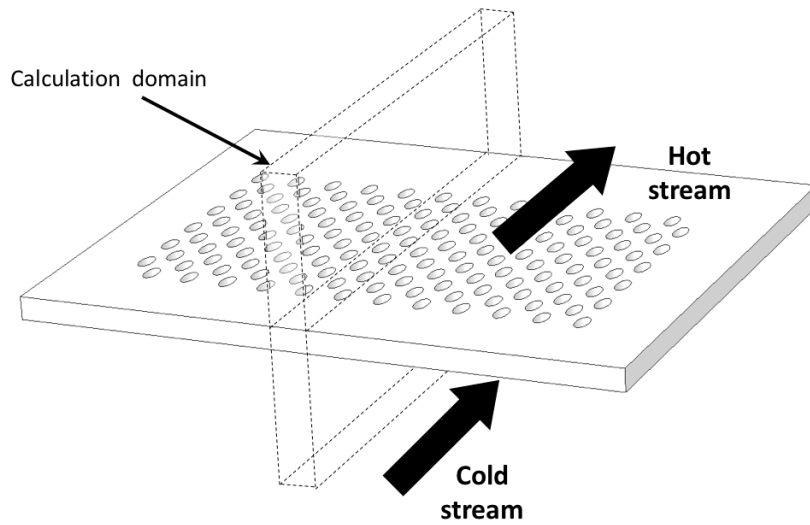


Figure 4.1: Maveric multiperforated plate setup. The computational domain is also displayed.

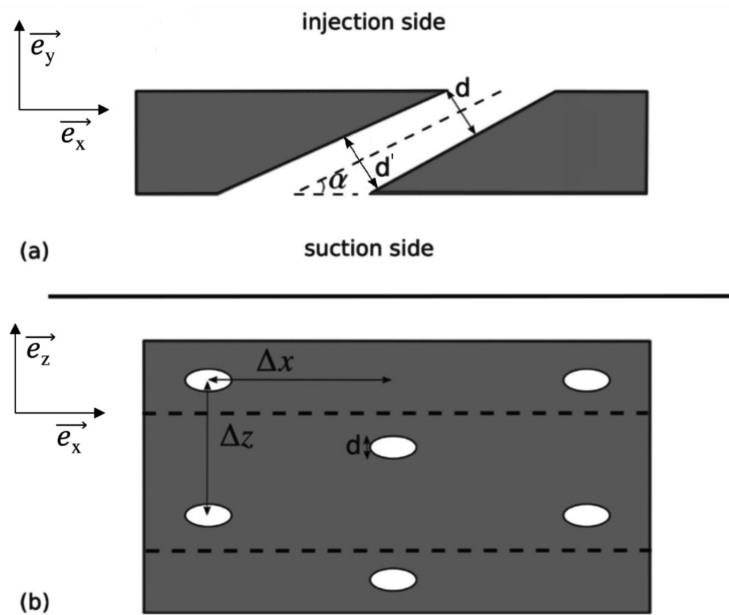


Figure 4.2: (a) Detailed side view of the perforation, (b) top view of the plate with the periodic domain calculated (dotted).

The hot and cold channels are  $114.25d$  long,  $H = 24d$  high and  $6.74d$  wide. The perforation length is about  $4.3d$ , a typical value for liners in combustion chambers. Note also that the apertures are slightly conical (convergent) with  $d' = 1.33d$  (see Fig. 4.2). The pressure of the hot flow is about 0.445 MPa and the temperature equals 1580 K, while it is 667 K on the cold side.

Diameters (mm)	Porosity $\sigma$	Angle $\alpha$	Thickness $e$	$\Delta x$	$\Delta z$
$d = 0.4, d' = 1.33d$	$4.09 \times 10^{-2}$	$27.5^\circ$	$2d$	$5.84d$	$6.74d$
	M	J	Re	Mach	
	8.4	31	2700	0.26	

Table 4.2: Main characteristics of the numerical Maveric configuration. Geometrical parameters are the same as in experiment from Florenciano and Bruel [35] except that  $d=0.4$  mm instead of  $d=5$  mm. The flow regime (M and J values) is representative of an actual aero-engine.

The computational domains used in this study are depicted in Fig. 4.3. To ease the reproduction of the calculation and because turbulent fluctuations in the main flow play a minor role for the investigated flow regime [58, 40], no turbulent fluctuations were prescribed at the inlet boundaries. Still, the velocity profiles were set with a power law based on the Reynolds number as appropriate for turbulent flows. For the hot side, the inlet velocity is defined as:

$$U_{hot} = 30 \left( 1 - \left( \frac{|y_{ch} - y|}{0.5H} \right)^5 \right), \quad (4.1)$$

where  $y_{ch}$  is the  $y$  coordinate of the hot channel center and  $H$  his height. It corresponds to a mean velocity of  $25 \text{ m s}^{-1}$ .

The inlet velocity on the cold side is defined as:

$$U_{cold} = 57.8 \left( 1 - \left( \frac{|y_{cc} - y|}{0.5H} \right)^{6.4} \right). \quad (4.2)$$

where  $y_{cc}$  is the  $y$  coordinate of the cold channel center and  $H$  his height. It corresponds to a mean velocity of  $50 \text{ m s}^{-1}$ .

The mass flow rate across the plate is controlled by the pressure difference between the two channels, which is about 3% of the injection side pressure ( $\Delta P = 13327 \text{ Pa}$ ). The working fluid is air. These conditions lead to blowing and momentum ratios equals to  $M = 8.4$  and  $J = 31$  respectively. The resulting Reynolds (based on the aperture diameter and bulk velocity) and Mach numbers within the perforations (averaged over the twelve rows) are 2700 and 0.26, respectively. The main physical properties of the material used (KCN22W) for the plate itself are given in Table 4.3.

To save computational time and because side effects have no influence on the flow at the center, only one hole per rows have been computed (instead of 12 in the experiment) making a total of 12 holes in the simulation out of 144 in the experiment. Periodic conditions have been used in the spanwise direction to properly reproduce the staggered arrangement and jets interactions. The upper and lower

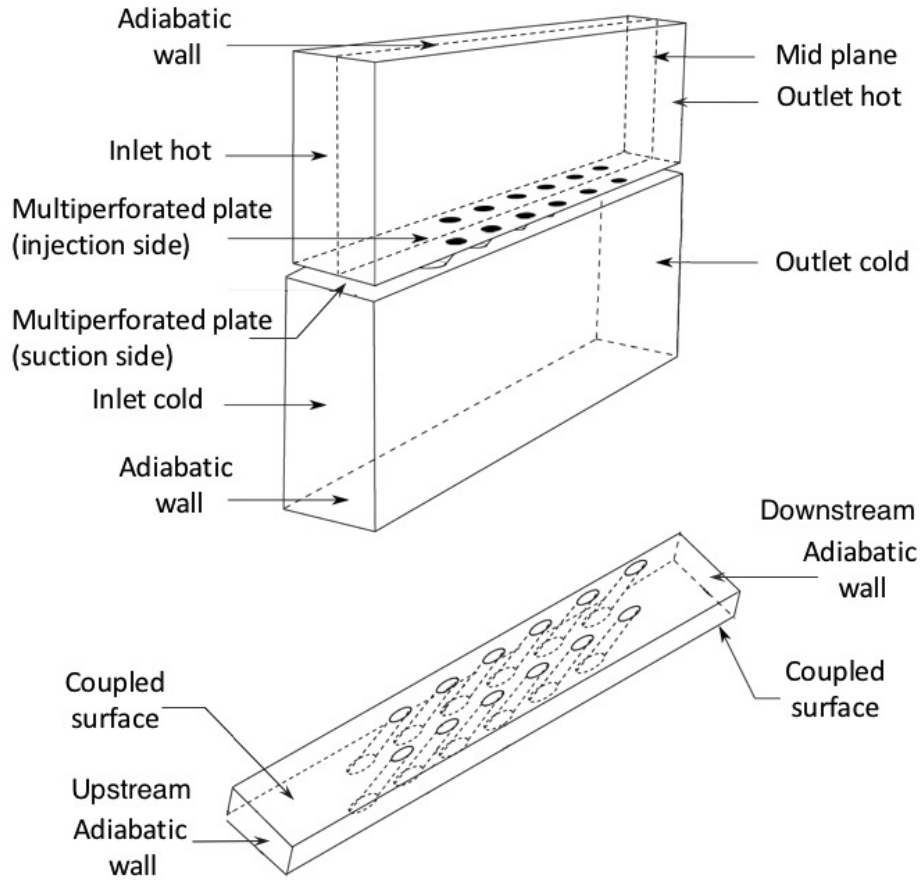


Figure 4.3: Fluid (top) and solid (bottom) computational domains and boundary conditions used in the Maveric numerical setup.

walls of the hot and cold channels are both considered adiabatic (Fig. 4.3). For the boundary interfaces between the flow domain and the multi-perforated plate, a no slip condition is applied on the cold and hot sides of the plate as well as within the apertures. The thermal condition is either adiabatic for fluid standalone simulation or temperature imposed when both the fluid and solid domains are coupled. In the latter case, the heat flux computed from the fluid side is used as a boundary condition for the solid domain where the unsteady heat equation is solved. In both cases, adiabatic wall conditions are prescribed at the downstream and upstream solid faces (Fig. 4.3).

Density $\rho$	$7900 \text{ kg m}^{-3}$
Conductivity $\lambda_s(T)$	$5.96 + 0.017 \times T \text{ W m}^{-1} \text{ K}^{-1}$
Heat capacity $C_P$	$586 \text{ J kg}^{-1} \text{ K}^{-1}$

Table 4.3: Thermo physical properties of the plate.

## 4.1.2 Description of the numerical softwares

### AVBP

The AVBP LES solver [159] mainly used during this PhD thesis is own by CERFACS and IFPEN (Institut Francais du Petrole Energies Nouvelles). It has been extensively used and widely validated on reactive flow numerical simulation, mainly for combustion applications [135, 171, 153]. It was designed from the very beginning to be used for massively parallel computations on dedicated architectures, addressing all the issues associated with High Performance Computing (HPC). The simulations presented in this work were performed on both internal (Neptune, Nemo and kraken) and external machines (Occigen and Terra1000-2).

The code solves the full compressible, multi-species, reactive NS equations, presented previously in the simplified mono-species and non-reactive form suitable for our study. The solver relies on the cell-vertex approach (data stored at mesh nodes) and finite volume method on unstructured or hybrid meshes which gives among other advantages a good robustness against mesh distortion [103]. Temporal integration is performed by an explicit formulation which globally controls the timestep and respect the Courant Friedrichs Lewy condition (CFL). LES requires numerical schemes providing high order discretisations and especially low-dissipation models (to respect the distribution of energy on the turbulent spectra) which are often offered by central differencing schemes [12]. In AVBP, various numerical schemes are available, particularly two schemes were used in this work:

- Lax-Wendroff scheme is a space and time second order centred scheme [105, 107] adapted to the cell-vertex method [48]. It does not have excellent dissipation and dispersion properties and is only used here for transient and initialisation of the calculations because it is the cheapest one.
- TTGC is a version of the two-step Taylor-Galerkin schemes providing a third order discretisation both in space and time [43]. It is known to be a good candidate for LES thanks to its good dissipation and dispersion properties [160]. It is used for all the simulations.

In AVBP, the use of centred schemes with low dissipation requires the addition of artificial diffusion operators. Indeed, transport of high gradient may lead to the Gibbs phenomenon [70] with the apparition of non-physical node-to-node oscillations called wiggles. To help the diffusion operator in its task, artificial viscosity can be added locally in the field to remove numerical oscillations. A sensor [85] specifically dedicated to unsteady turbulent flow can automatically detect numerical anomalies and increase local viscosity in the limitation of a user-defined threshold.

## YALES2

The second LES solver used during this thesis for a few comparisons is the YALES2 solver [134]. It is an unstructured low-Mach number code developed at CORIA. YALES2 aims at the solving of two-phases combustion, from primary atomisation to pollutant prediction on massive complex meshes. It is able to handle efficiently unstructured meshes with several billions of elements, thus enabling the Direct Numerical Simulation of laboratory and semi-industrial configurations. YALES2 is based on a large numerical library to handle partitioned meshes, various different operators or linear solvers, and on a series of simple or more complex solvers.

### 4.1.3 Maveric plate with longitudinal cooling

To create a database, a fully resolved simulation, where hot and cold sides as well as the flow within the holes are taken into account, has been performed. The fully resolved mesh is presented on Fig. 4.4. The mesh resolution corresponds to  $R = 16$ ; It is unstructured without stretching direction.

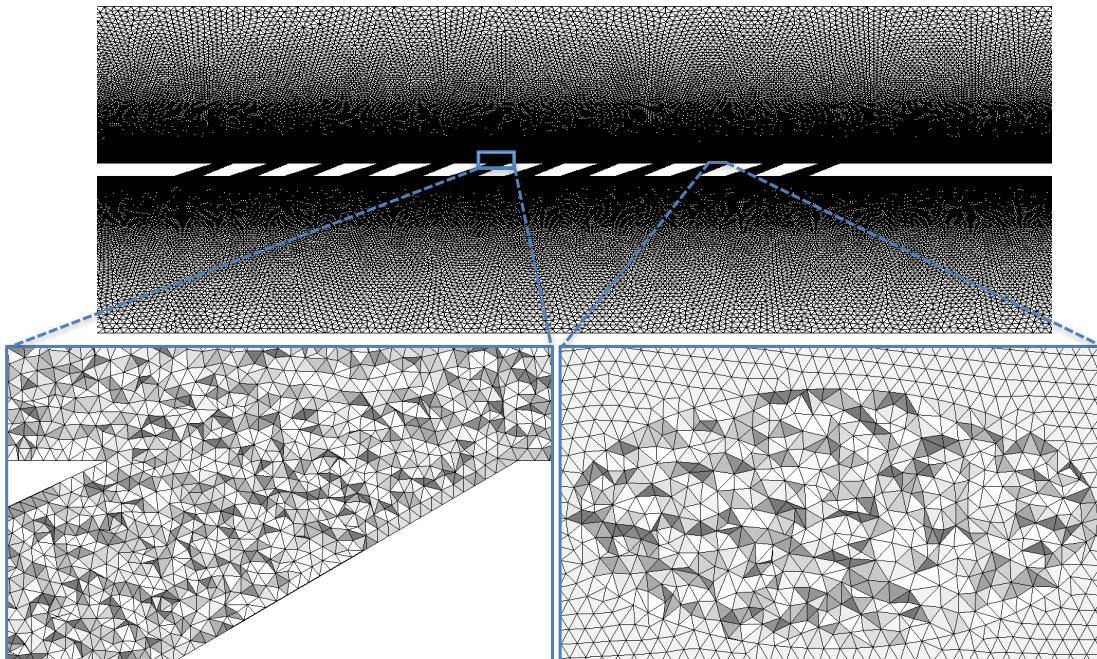


Figure 4.4: Visualisation of the mesh used to perform the fully resolved computation.

As part of the validation of the database, the influence of the subgrid scale model has been tested. Two fully resolved adiabatic simulations have been performed with the AVBP LES solver. One using  $\sigma$ -model [142], and one with the WALE subgrid scale model [141]. From the result of the simulations, the  $\sigma$ -model induced less

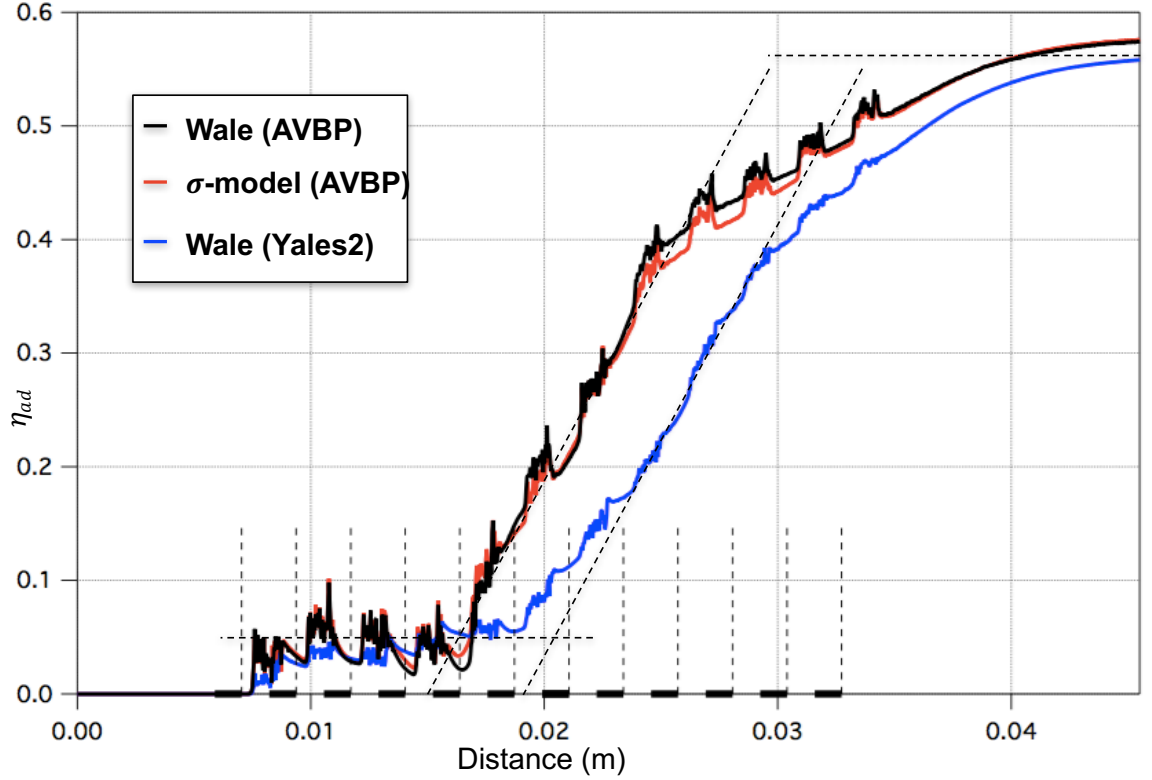


Figure 4.5: Comparison of the fully resolved adiabatic computation using two solvers; A compressible third order in space AVBP; An incompressible fourth order Yales. WALE and  $\sigma$  subgrid scale models are also compared.

viscosity. However, both computations give about the same results, as presented on Fig. 4.5. The solver itself has also been tested, the same simulation (same resolution but not the same geometry for boundary conditions issues) using YALES2 solver has been performed. Comparison on the adiabatic efficiency is presented on Fig. 4.5. Both results are close since the slope and the final value are the same. However, the mixing process does not seem to be the same, and the wall adiabatic temperature is shifted of about one row. The fully resolved computation from AVBP using WALE subgrid scale model will be considered as the reference for the following study.

To validate the accuracy of the thickened-hole model, four mesh resolutions were considered and presented on Fig. 4.6. Only the injection side (hot side) is considered. Mass flow rate is extracted from the fully resolved computation and corresponds to  $3.3m^3/s$ . On each mesh two simulations, one with the homogeneous model and one with a thickened-hole model has been performed and compared to the results from the fully resolved computation, *i.e.* perforations simulated, considered as the reference. All the simulations performed on the Maveric plate with longitudinal cooling cases are summarised on Fig 4.4.

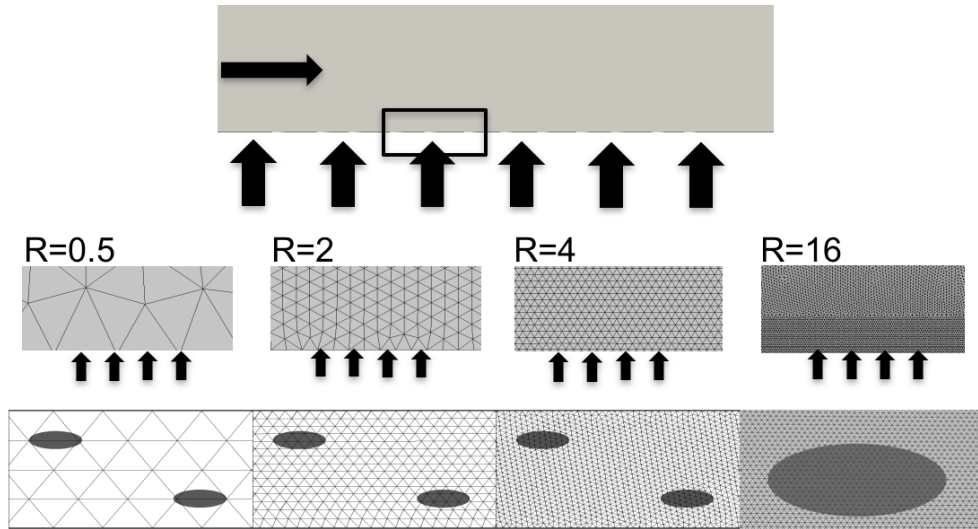


Figure 4.6: Mesh resolution comparison on both the multiperforated wall and in the domain. The arrows represents the inlets.

Software	Hole resolution	sub-grid model	Effusion model
AVBP	Resolved	WALE	N/A
AVBP	Resolved	$\sigma$ -model	N/A
YALES2	Resolved	WALE	N/A
AVBP	R=16	WALE	Thickened-hole
AVBP	R=4	WALE	Thickened-hole
AVBP	R=4	WALE	Homogeneous
AVBP	R=2	WALE	Thickened-hole
AVBP	R=2	WALE	Homogeneous
AVBP	R=0.5	WALE	Thickened-hole
AVBP	R=0.5	WALE	Homogeneous

Table 4.4: Characteristics of the simulations performed on the Maveric plate with longitudinal cooling test cases.

Time averaged solutions are first considered. To provide a fair comparison between homogeneous and thickened-hole models, the profiles are averaged over the transverse direction in two portions of the flow: Pos1, where the flow is not established and Pos2, (grey rectangles on Fig. 4.7), where the film cooling effect is present. Figures 4.8, 8.2 and 4.10 present profiles of momentum in the tangential direction, momentum in the normal direction and temperature, respectively, as a function of  $Y^*$ , the distance from the plate in the normal direction normalized by  $\Delta$  the inter-row distance, Fig. 4.7. On Fig. 4.11 and Fig. 4.12, profiles for temperature RMS fluctuations as well as streamwise velocity RMS fluctuations are also presented.

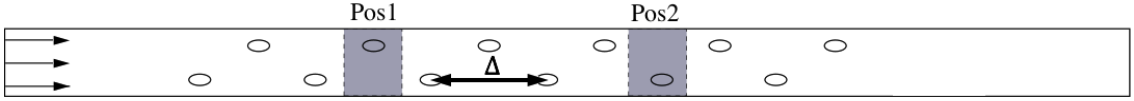


Figure 4.7: Top view of the plate with the location of the averaging areas Pos1 and Pos2.

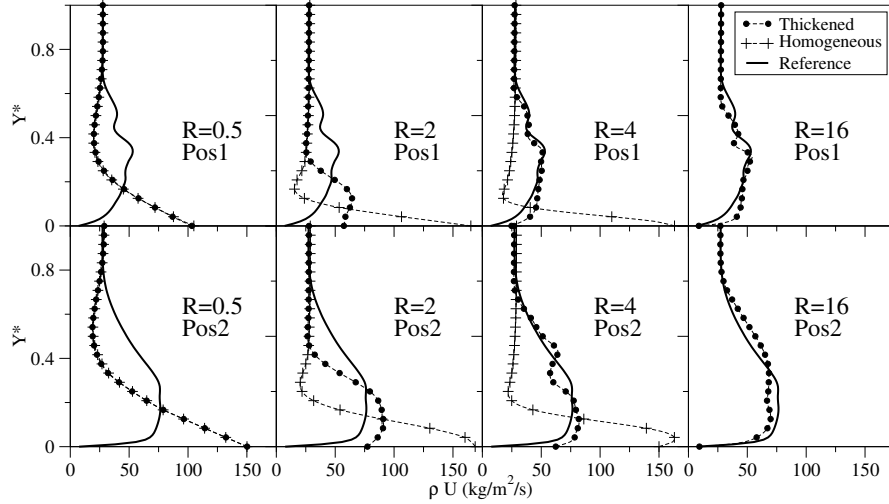


Figure 4.8: Spatially and temporally averaged streamwise momentum  $\rho U$  at positions Pos1 (top) and Pos2 (bottom), for ratios  $R=0.5; 2; 4; 16$  (from left to right). —: reference, ●: thickened-hole model, +: homogeneous model.

When the ratio  $R$  is lower than one, the homogeneous and thickened-hole model give, as expected, very similar results, in bad agreement with the resolved computation. Figure 4.8 shows that the tangential momentum is too large close to the plate, leading to a thinner mixing layer and to a lower temperature at the wall as shown on Fig. 4.10. When the flow is established (Pos2), normal momentum is well represented since the mass flow rate through the multiperforated plate is correctly imposed (see Fig. 8.2).

When  $R$  is equal or bigger to 4, the thickened-hole model gives better results than the homogeneous model. With this resolution, results are close to the fully resolved one whatever the position and for all variables.

For intermediate values,  $R=2$ , the thickened-hole model better predicts the evolution of the flow compared to the homogeneous model. Indeed, the shape of the mixing layer is accurately predicted both for established (Pos2) and non-established (Pos1) flows. In the non-established region, the thickened-hole model is able to capture the negative values for  $\rho V$  observed in the resolved computation for  $Y^* > 0.4$  (Fig. 8.2). This specific feature is crucial if one focuses on non-established flows.

RMS temperature fluctuations (Fig. 4.11) and streamwise RMS velocity fluctua-

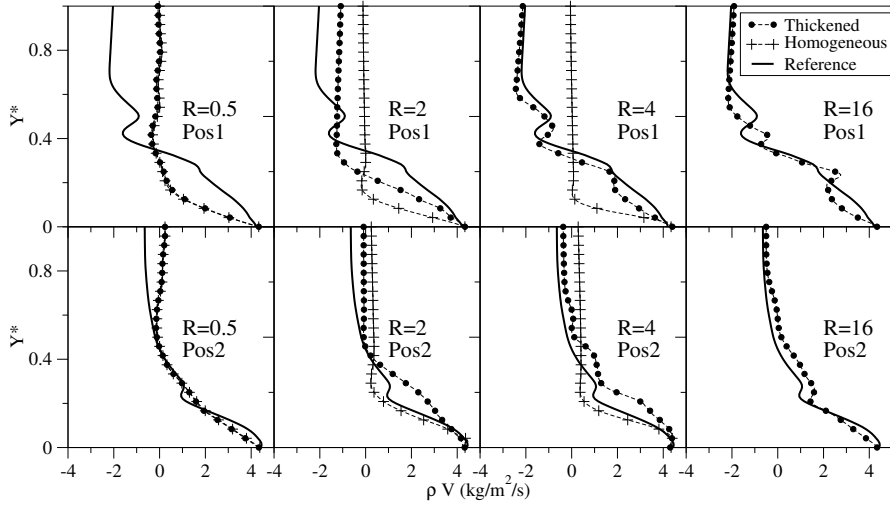


Figure 4.9: Spatially and temporally averaged normal momentum  $\rho V$  at positions Pos1 (top) and Pos2 (bottom), for ratios  $R=0.5$ ; 2; 4; 16 (from left to right). **—**: reference, **•**: thickened-hole model, **+**: homogeneous model.

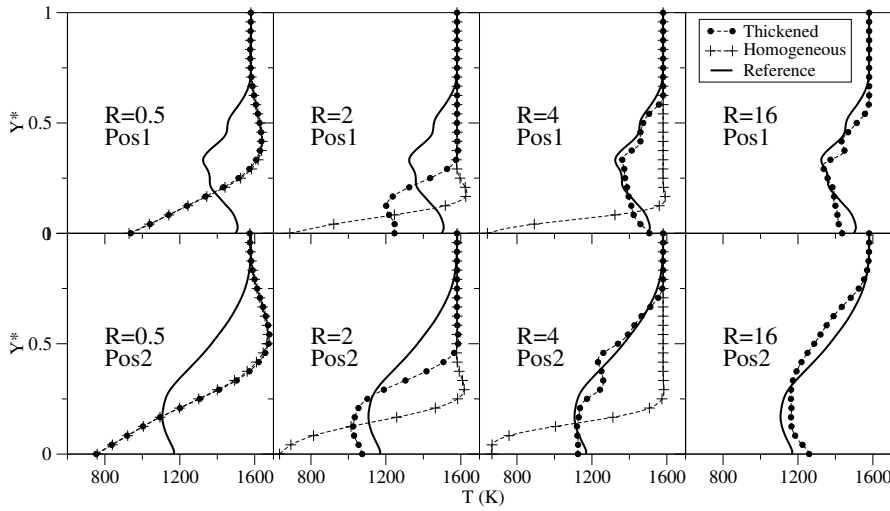


Figure 4.10: Spatially and temporally averaged temperature profiles at positions Pos1 (top) and Pos2 (bottom), for ratios  $R=0.5$ ; 2; 4; 16 (from left to right). **—**: reference, **•**: thickened-hole model, **+**: homogeneous model.

tions (Fig. 4.12) are produced when  $R$  is greater or equal to 4 with the thickened-hole model. For  $R = 4$ , the model predicts very small fluctuations at the first position (Pos1) where the film cooling is not established; the agreement being much better for Pos2 which points to potential issues when facing non fully established flows. Note that this specific difficulty can not be adequately treated with existing models other than the thickened-hole model. When  $R=16$ , the RMS fluctuations match the reference data even in the non established region.

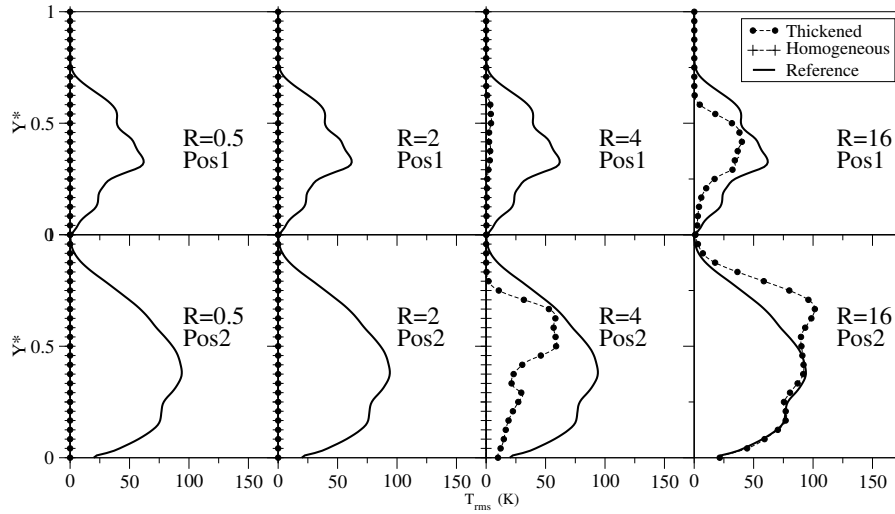


Figure 4.11: Spatially and temporally averaged RMS temperature profiles at positions Pos1 (top) and Pos2 (bottom), for ratios  $R=0.5$ ; 2; 4; 16 (from left to right). **—**: reference, **•**: thickened-hole model, **+**: homogeneous model.

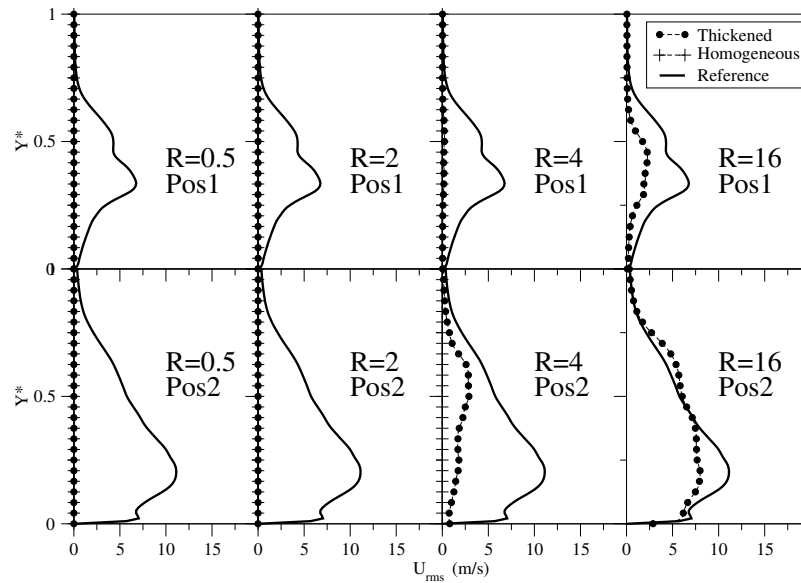


Figure 4.12: Spatially and temporally averaged streamwise RMS velocity profiles at positions Pos1 (top) and Pos2 (bottom), for ratios  $R=0.5$ ; 2; 4; 16 (from left to right). **—**: reference, **•**: thickened-hole model, **+**: homogeneous model.

At this point, the thickened-hole model has been validated based solely on time and space averaged fields. The discrete form of this model however also allows to represent the flow fluctuations in LES as hinted by Figs. 4.12 and 4.11. This capacity is further illustrated by Fig. 4.13 where instantaneous temperature fields for the homogeneous and the thickened-hole models for various  $R$  values are compared

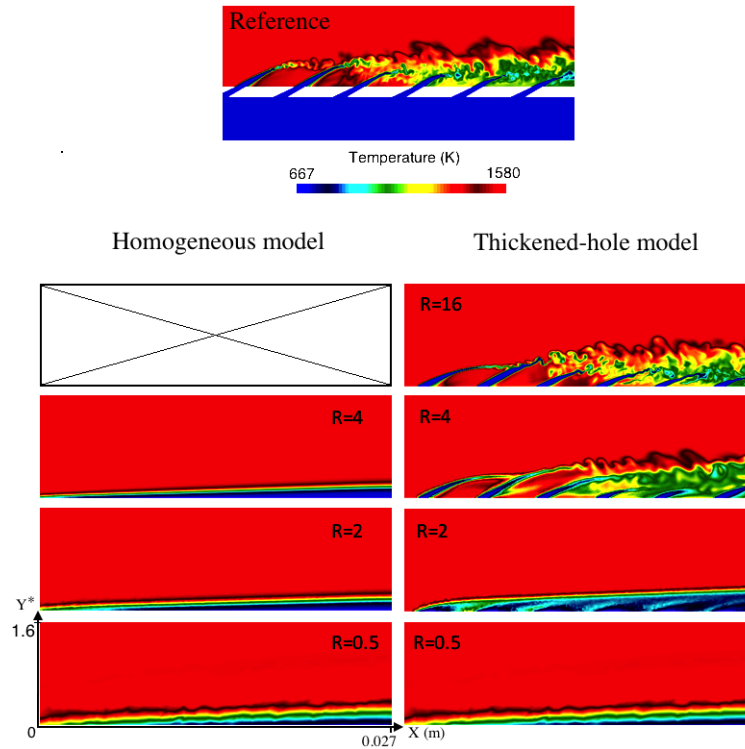


Figure 4.13: Visualisation of the coolant film. Comparison between simulations using homogeneous model (left) and thickened-hole model (right) for various  $R$  values.

to the resolved simulation. With the thickened-hole model, jets can be distinguished for  $R \geq 2$ . This is a major step forward as the interaction between jets can now be examined. For  $R \geq 4$ , the jets are very similar to the resolved ones.

#### 4.1.4 Maveric plate with transverse cooling

In order to study the effect of the deviation, the Maveric test case with transverse cooling is considered. The first step consist in the creation of the database. A fully resolved computation with  $\alpha = 30^\circ$  and  $\beta = 90^\circ$  has been simulated using AVBP software and wale subgrid scale model. The mesh is presented on Fig. 4.14. The geometry is different compared to the last case, however, the mesh resolution is similar and corresponds to  $R = 16$ . The flowrate through the 12 holes extracted from the reference computation corresponds to  $2.7 \cdot 10^{-4} \text{ m}^3/\text{s}$  instead of  $3.3 \cdot 10^{-4} \text{ m}^3/\text{s}$  when  $\beta = 0^\circ$ . It corresponds to a difference of 17%. However, for all the modelled simulations, a flowrate of  $3.3 \cdot 10^{-4} \text{ m}^3/\text{s}$  has been imposed.

Three mesh resolutions from  $R = 0.5$  to  $R = 4$  already presented in the last section (See Fig. 4.6) have been used. On each, two simulations, one with the thickened-hole model [29] and one with the homogeneous model [125] have been

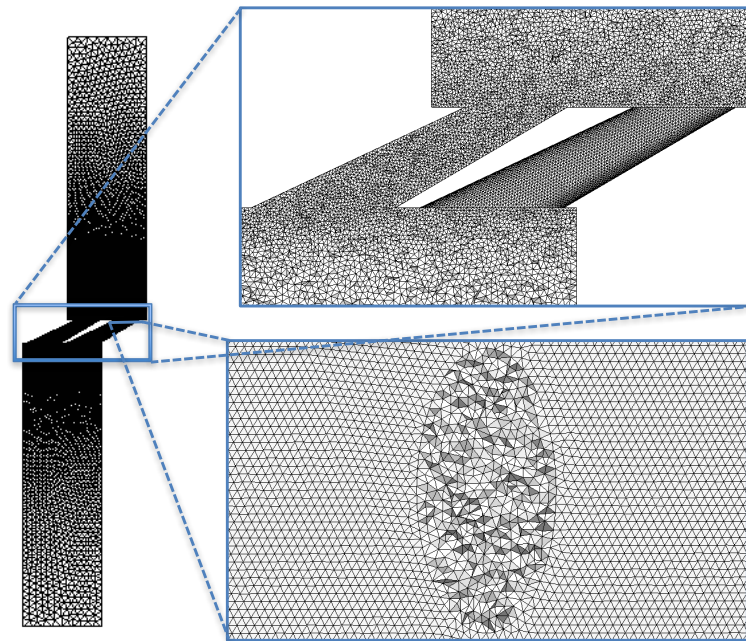


Figure 4.14: Representation of the mesh resolution on the fully resolved Maveric test case with transverse cooling.

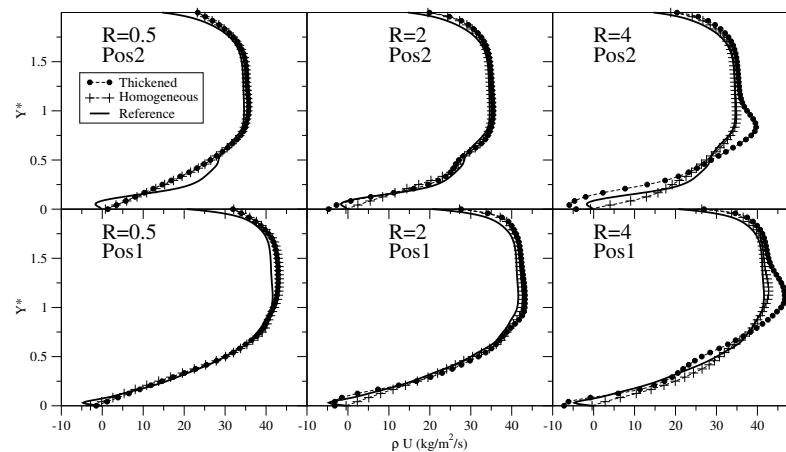


Figure 4.15: Spatially and temporally averaged streamwise momentum  $\rho U$  at positions Pos1 (top) and Pos2 (bottom), for ratios  $R=0.5$ ; 2; 4 (from left to right).  $\bullet$ : reference,  $\bullet$ : thickened-hole model,  $+$ : homogeneous model.

performed. The same post-processing as for Maveric plate without deviation has also been performed. On Figs. 4.15, 4.16 and 4.17, profiles for streamwise and tangential velocity as well as temperature fields are presented. Performed simulations are summarised on Fig 4.5.

Software	Hole resolution	sub-grid model	Effusion model
AVBP	Resolved	WALE	N/A
AVBP	R=4	WALE	Thickened-hole
AVBP	R=4	WALE	Homogeneous
AVBP	R=2	WALE	Thickened-hole
AVBP	R=2	WALE	Homogeneous
AVBP	R=0.5	WALE	Thickened-hole
AVBP	R=0.5	WALE	Homogeneous

Table 4.5: Characteristics of the simulations performed on the Maveric case with a deviation angle.

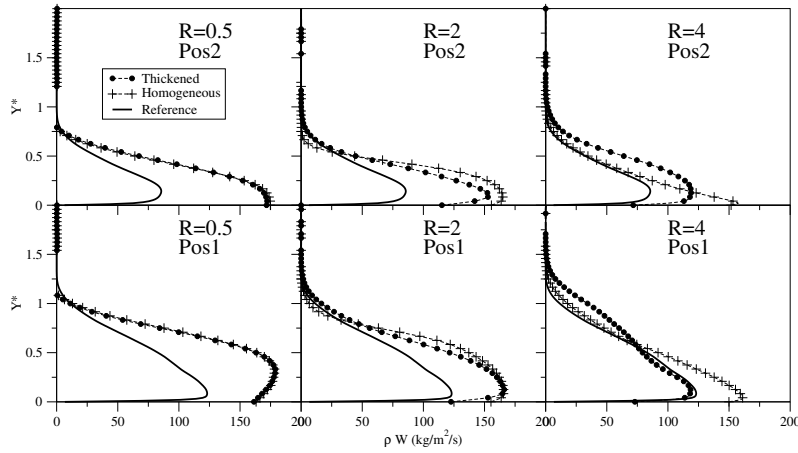


Figure 4.16: Spatially and temporally averaged spanwise momentum  $\rho U$  at positions Pos1 (top) and Pos2 (bottom), for ratios  $R=0.5$ ; 2; 4 (from left to right). —: reference, ●: thickened-hole model, +: homogeneous model.

The first comparison can be made between the two cases ( $\beta = 0^\circ$  and  $\beta = 90^\circ$ ); the wall temperature is much lower when using deviation angle (Fig. 4.17) than without (Fig. 4.10). Indeed, for high deviation angle, such as in the present case, the flow is more homogeneous, and the wall is better protected. As already known, this system is much more efficient. First rows (pos1) as well as established zone (pos2) reach lower adiabatic wall temperature.

When focusing only on the present case (with deviation), globally both models predict close results for any mesh resolution. When looking closer, for  $R = 0.5$  and  $R = 2$ , homogeneous and thickened-hole models give the same result. Both are close from the longitudinal momentum ( $\rho U$ ) (see Fig. 4.15) and for the temperature (see Fig. 4.17). For the tangential momentum ( $\rho W$ ) (see Fig. 4.16) both models overpredict it for the two positions.

When the resolution increases to  $R = 4$ , the thickened-hole model captures the peak and the gradient, contrarily to the homogeneous model. However as pointed

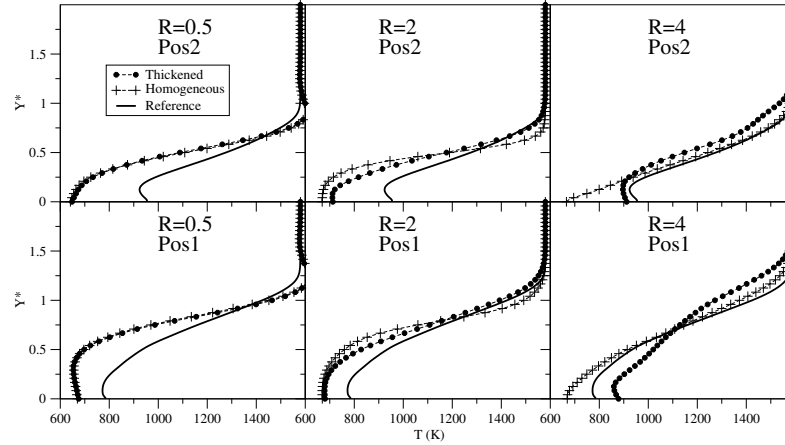


Figure 4.17: Spatially and temporally averaged temperature profiles at positions Pos1 (top) and Pos2 (bottom), for ratios  $R=0.5$ ; 2; 4 (from left to right). **—**: reference, **••**: thickened-hole model, **++**: homogeneous model.

out in the last section, when the resolution is higher, jets penetrate too much (see Fig. 4.17).

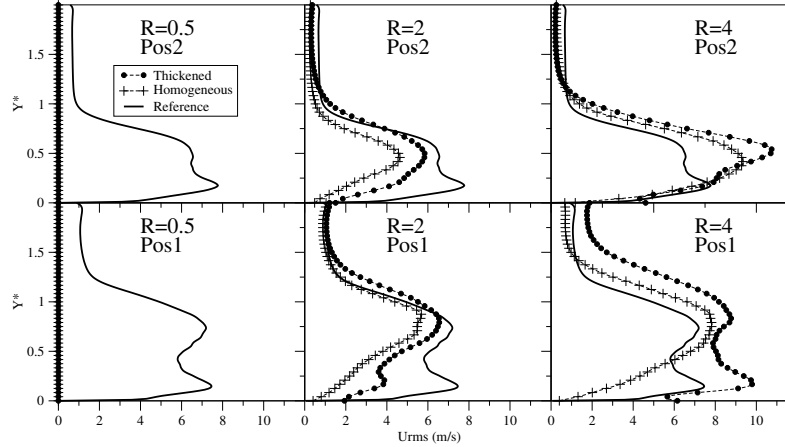


Figure 4.18: Spatially and temporally averaged streamwise RMS velocity profiles at positions Pos1 (top) and Pos2 (bottom), for ratios  $R=0.5$ ; 2; 4 (from left to right). **—**: reference, **••**: thickened-hole model, **++**: homogeneous model.

RMS fluctuations on the streamwise and tangential velocity as well as temperature fluctuations are also presented on Figs. 4.18, 4.19, 4.20.

On the case without deviation ( $\beta = 0^\circ$ ), RMS fluctuations appear when  $R \leq 4$  instead of  $R \leq 2$  for the transverse case ( $\beta = 90^\circ$ ). Indeed, the  $R = 0.5$  case is not sufficient to recover the RMS quantities. When the resolution increases, both models predict the proper level of fluctuation. However, the thickened-hole mode allows to capture the first peak on  $U_{rms}$  (See Fig. 4.18) which is not the case for

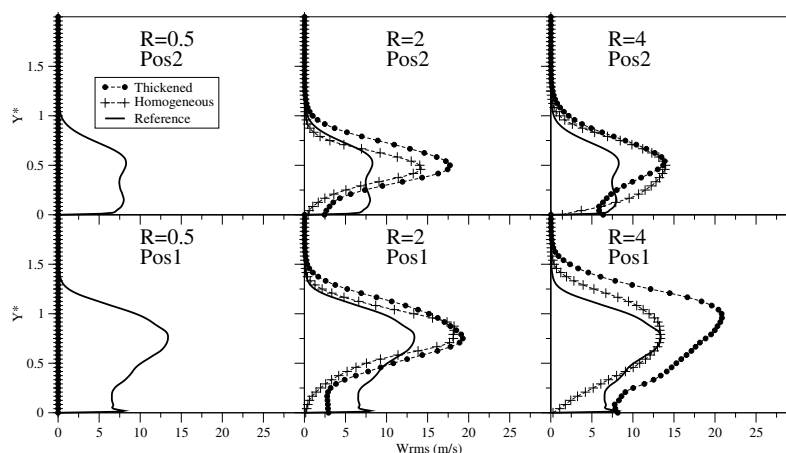


Figure 4.19: Spatially and temporally averaged spanwise RMS velocity profiles at positions Pos1 (top) and Pos2 (bottom), for ratios  $R=0.5$ ; 2; 4 (from left to right). —: reference, ●: thickened-hole model, +: homogeneous model.

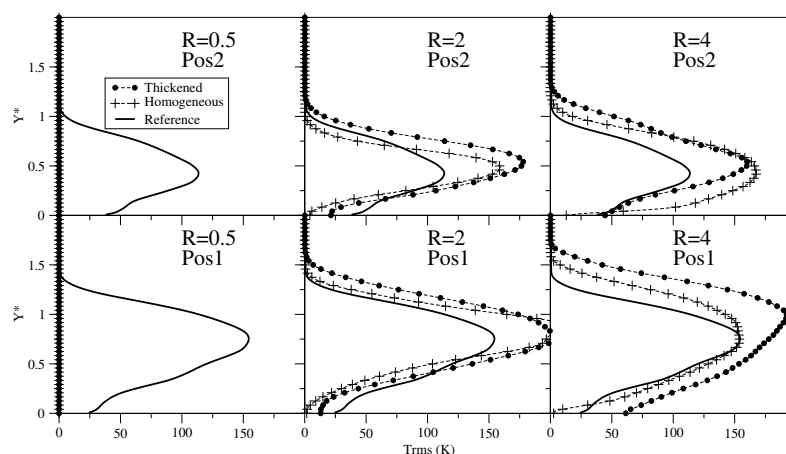


Figure 4.20: Spatially and temporally averaged RMS temperature profiles at positions Pos1 (top) and Pos2 (bottom), for ratios  $R=0.5$ ; 2; 4 (from left to right). —: reference, ●: thickened-hole model, +: homogeneous model.

the homogeneous model. On the fine case ( $R=4$ ), the thickened-hole approach overpredicts the RMS, but accurately predicts the trend (peaks and gradients) for the three directions. On the contrary, the homogeneous model better predicts the global value of the RMS level.

The thickened-hole model in the transverse case has been investigated by considering time and space averaged fields. Instantaneous temperature fields for each mesh resolution and modelling strategy are presented on Fig. 4.21. Contrary to the longitudinal case, the jets cannot be distinguished on any mesh resolution. Whatever the mesh resolution, both model presents a really close temperature field. It

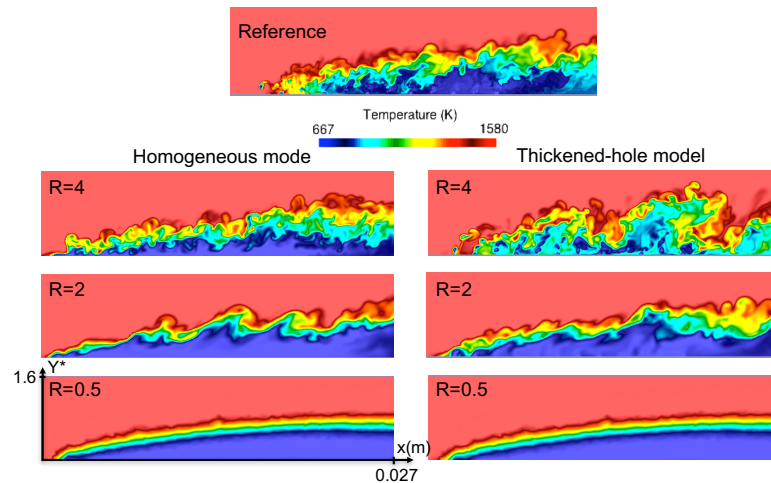


Figure 4.21: Visualisation of instantaneous temperature field. Comparison between simulations using homogeneous (left) and thickened-hole model (right) for various  $R$  values.

leads to the conclusion that the mesh resolution plays the leading role since the mixing process is dependent on the small eddies. The result on the  $R=4$  resolution is really close to the reference even if the thickened-hole model mixes too much and has a higher temperature than the reference one close to the wall.

The thickened-hole model [29] is now tested on an academic test case including both sides of the domain, and is thus, closer to what it is expected on real combustor.

#### 4.1.5 Feasibility of a two-side effusion simulation with the thickened-hole model

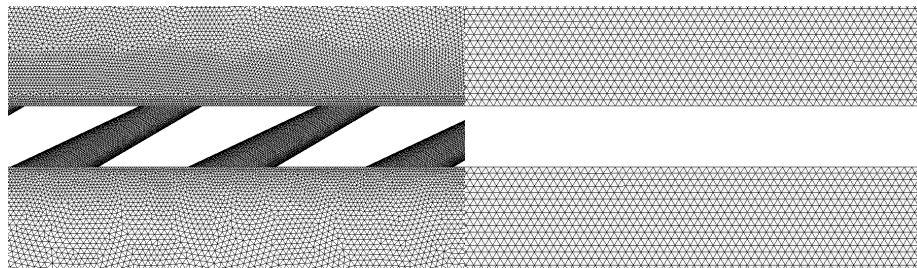


Figure 4.22: Comparison of the fully resolved mesh where holes are meshed (left) and modelled where holes are erased (right). Resolution is also different:  $R=16$  for the resolved and  $R=4$  for the modelled.

Simulate the two sides of the perforated plate is necessary when dealing with industrial combustor. Using the same principle as explained in section 3.2, the

flowrate relevant to each single aperture feeds the effusion model on the injection side (see Section 3.2). For the suction side, the holes are projected on the boundary along the jet axis and the suction model is the one introduced by Mendez and Nicoud [125] using the corresponding flowrate.

The mesh is presented on Fig. 4.22. On the left, the fully resolved mesh already presented in the last section is visible. On the right, the modelled mesh which corresponds to  $R=4$  is only composed of the two sides while holes are erased. Note that the hole position is well projected on both side and thus the angle of the jets is well accounted (see Fig. 4.23).

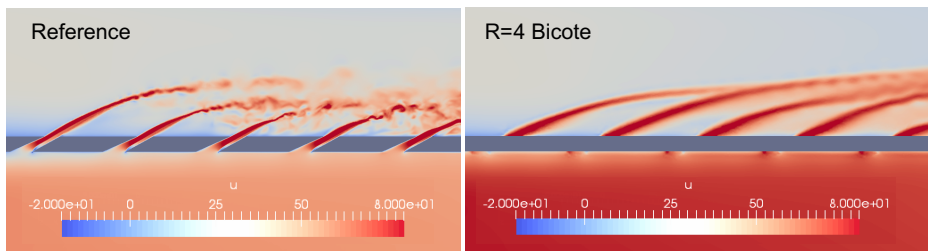


Figure 4.23: Instantaneous flow visualisation of the streamwise velocity for the fully resolved (left) and the modelled (right) case.

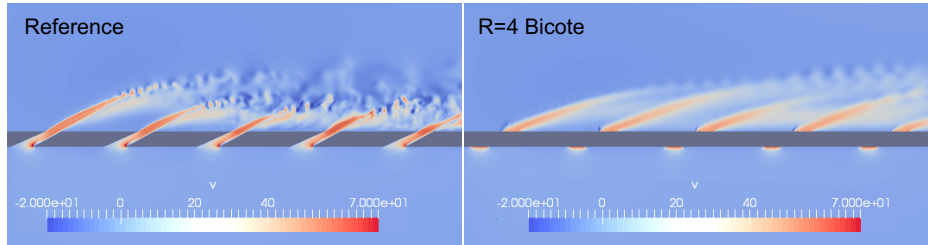


Figure 4.24: Instantaneous flow visualisation of the normal velocity for the fully resolved (left) and the modelled (right) case.

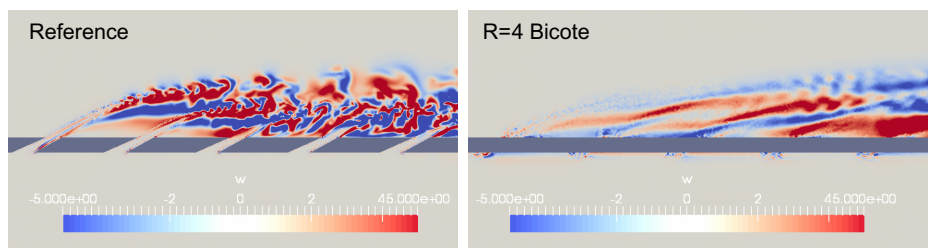


Figure 4.25: Instantaneous flow visualisation of the spanwise velocity for the fully resolved (left) and the modelled (right) case.

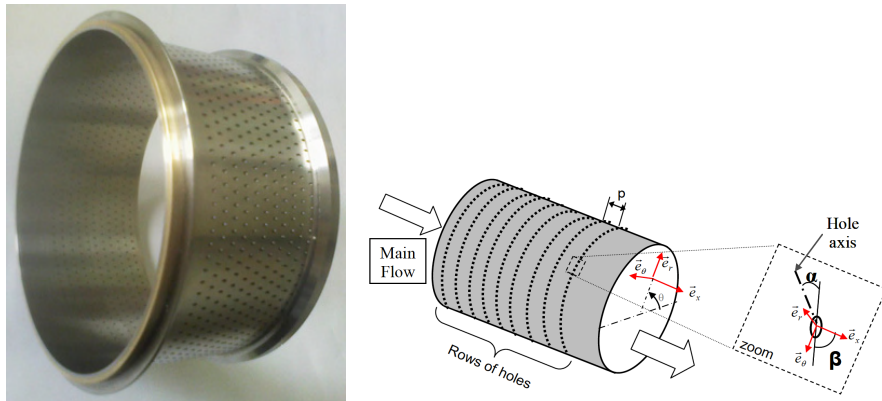
Time and space averaged results are the same as the one presented in Section 4.1.3 for the injection side and are thus not presented again. The instantaneous result of the simulation for the streamwise (see Fig. 4.23), normal (see Fig. 4.24) and spanwise (see Fig. 4.25) velocity components are presented. Since the flow into the pipe is not simulated the jets are not exactly the same but the position of the holes on the suction side is well modelled and the global flow structure remains close. On Fig. 4.25, the reference case has much more fluctuations than the modelled one.

## 4.2 Michel tube test case

### 4.2.1 Experimental setup

The second geometry investigated has been studied numerically and experimentally by Brice Michel [129]. There are a primary and a secondary flow (see Figs. 4.26 and 4.27a). Air from the secondary flow goes through the multiperforated ring and is thus injected into the first channel.

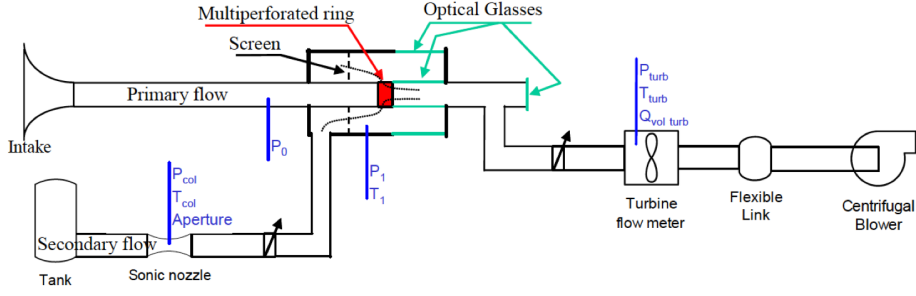
The optical access being after the ring mount, it is impossible to measure the inlet profiles (see Fig 4.27a). The trick was to use a dummy ring without perforation and to measure quantities, assuming the strong hypothesis that the multiperforated ring has no influence upstream.



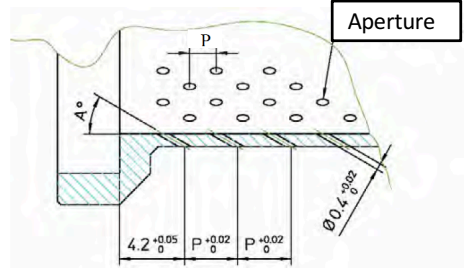
(a) Visualisation of the multiperforated ring (b) Schematic view of the ring. Axes conventions is also display.

Figure 4.26: Michel tube setup

Holes have a diameter of 0.4 mm (geometrical parameters are summarized in table 4.6). The injection angle is  $\alpha = 30^\circ$ . The longitudinal and spanwise spacing are  $8.6d$  and  $7.9d$  respectively. The porosity,  $\sigma$  is 0.023 which is typical of aeronautical combustors. The blowing ratio and the momentum ratio are 8.7 and 76 respectively. The Mach number into the aperture is close to 0.16 while the Reynolds number based on the jet velocity and the hole diameter is 1200.



(a) Visualisation of the experimental setup



(b) Schematic view of the arrangement of the apertures.

Figure 4.27: Brice Michel Setup

Diameters (mm)	Porosity $\sigma$	$\Delta x$	$\Delta z$	M	J	Re	Mach
$d = 0.4$	$2.3 \times 10^{-2}$	$8.6d$	$7.9d$	8.7	76	1200	0.16

Table 4.6: Parameters of the Michel tube setup.

As presented in Table 4.7, two configurations with different angle of apertures have been considered: a longitudinal one ( $\beta = 0^\circ$ ) and a transverse one ( $\beta = 90^\circ$ ). The multiperforated cylinder is laser drilled [152] with 891 holes distributed on 99 rows of 9 staggered apertures (see Fig. 4.27b).

Case	$\alpha$	$\beta$	Number of row	Number of hole per row
longitudinal	$30^\circ$	$0^\circ$	9	99
transverse	$30^\circ$	$90^\circ$	9	99

Table 4.7: Characteristics of the Michel tube setup.

A numerical simulation with the thickened-hole model [29] has been performed and compared to experimental results of Michel tube. Since the results of the experiment are very questionable (for the transverse case, the multiperforated ring seems to influence the inlet flow), present results have never been published.

## 4.2.2 The longitudinal Michel tube cooling case

The simulated case is the longitudinal one ( $\beta = 0^\circ$ ). The geometry is a cylinder of length  $9.288 \cdot 10^{-2}$  m. The Multiperforated Plate (MP) is  $3.096 \cdot 10^{-2}$  m long and located at the center. Indeed the inlet of the tube is  $3.096 \cdot 10^{-2}$  m away from the beginning of the MP, outlet is  $3.096 \cdot 10^{-2}$  m far from the end of the plate. The mesh is shown on Fig 4.28. This figure also displays the mesh evolution and the position of the experimental and numerical measurements. The thickened-hole model [29] has been used to model the multiperforated plate. Since the mesh is fine enough ( $R=5$ ), no thickened has been applied. The mesh resolution is shown on Fig. 4.29. In order to compare the numerical simulation to the experiment, inlet parameters are taken from the experience. Turbulence has also been added at the inlet. 10% on the streamwise velocity and 5% on the other directions. To ensure the correct transport of the inlet velocity and the turbulence intensity, the corresponding profiles are checked just before the multiperforated plate and presented just after.

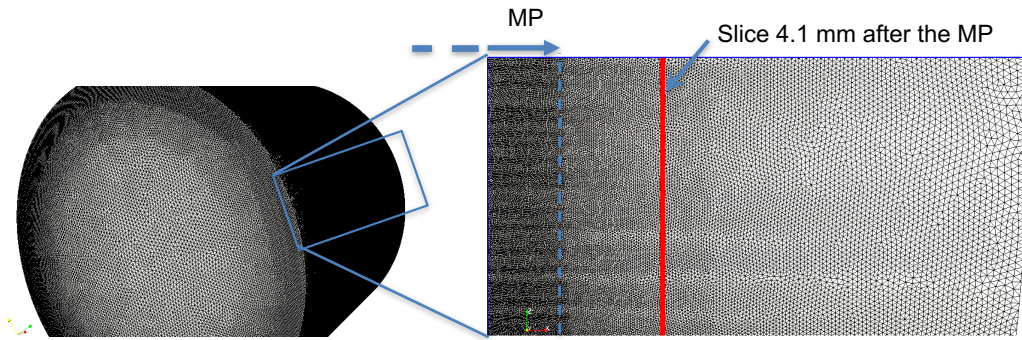


Figure 4.28: Mesh visualization of the full  $360^\circ$  setup.

Due to the periodicity, a 40 degrees sector can be computed. In order to check the validity of this assumption, the result of one sector ( $40^\circ$ ) has been compared to the full  $360^\circ$  using exactly the same parameters. The mesh of the full  $360^\circ$  setup contains about 350M elements while the sector of  $40^\circ$  contains about 40M cells. To check the convergence of the time averaged solution, more physical time was computed on the sector case, (see Table 4.8). To avoid the axis singularity in LES, in the  $40^\circ$  case, the center of the domain has been removed, flow rate has thus been adapted in order to keep the correct mean velocity. A slip wall has been used for the boundary close to the center in order to limit the boundary influence which is not present in the reality.

case	R	Cells	nb of processor	CPU cost (Kh)	Physical time (s)
Full $360^\circ$	5	345 267 965	5600	250	$2.8 \cdot 10^{-2}$
Sector $40^\circ$	5	39 391 852	2100	98	$9 \cdot 10^{-2}$

Table 4.8: Characteristics of the Michel tube setup.

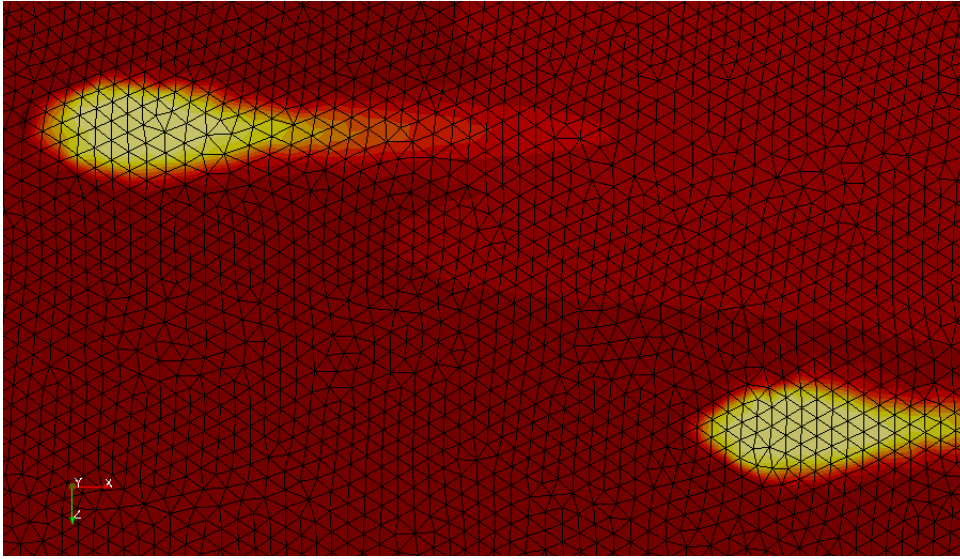


Figure 4.29: Representation of the jet on the mesh for the longitudinal Michel tube thanks to the cooling scalar.

The post processing, illustrated on Fig. 4.30, involves a spatial averaged on a ring with a thickness of 1 mm in the streamwise direction. The quantity of interest is plotted as a function of the distance from the center ( $r$ ) normalised by the maximal radius ( $R$ ). Time averaging is also performed.

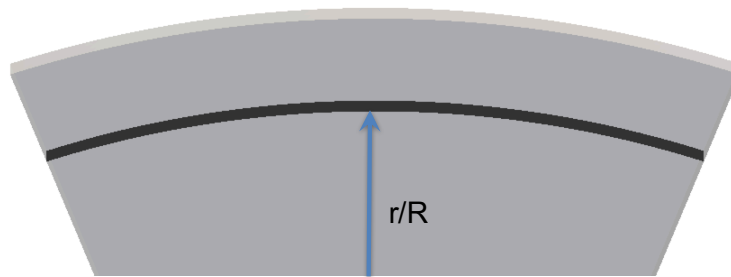


Figure 4.30: Description of the post processing.

On Fig. 4.31, numerical simulation on the sector and on the full geometry are compared to the experimental values. As stated before, in the experimental setup these quantities are extracted using a ring without holes while in the numerical case these quantities are extracted just before the perforated plate. The velocity is normalised by the streamwise velocity of the jet,  $u_p = V_{jet} \sin(\alpha) = 39.43$  m/s (Fig. 4.31a). The RMS are normalised by  $u^*$  which corresponds to the mean RMS value  $u^* = 0.58$  m/s (10%) (Figs. 4.31b, 04.31c, 4.31d). Since the imposed quantities at the inlet are the same, this result ensures the fact that quantities are well

convected. Moreover Fig. 4.31 validate both the periodic assumption and the inlet profiles. The same results are observed on the  $40^\circ$  periodic simulation as in the full  $360^\circ$  one, except at the center of the domain.

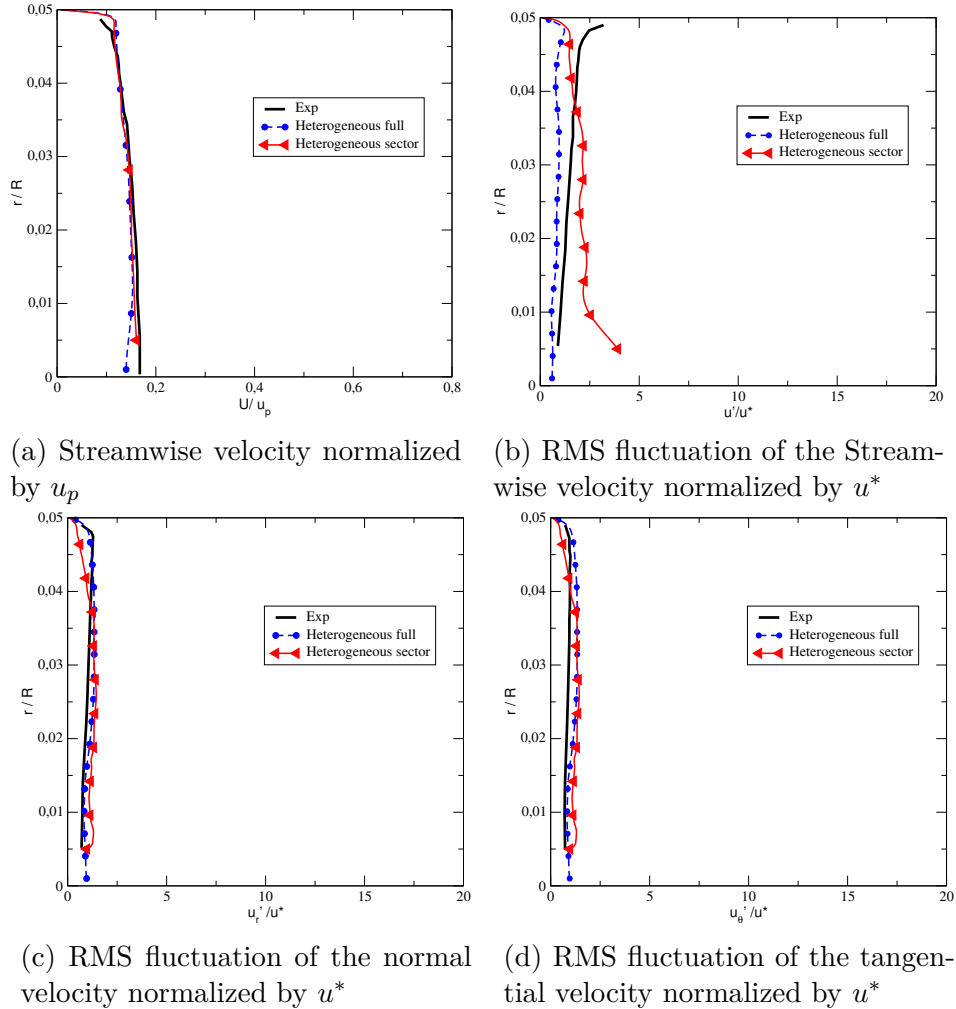


Figure 4.31: Comparison of the inlet velocities between experimental and numerical results for the longitudinal Michel tube.

To check the effects of the multiperforated plate and to compare numerical results with experimental data, the post processing presented on Fig. 4.30 is used 4.1 mm after the multiperforated plate (MP), displayed (red line) on Fig. 4.28.

On Fig. 4.32, results of the thickened-hole model applied either on the full  $360^\circ$  or on the sector are compared to experimental values. Also in order to check the influence of the model, a third computation using the homogeneous model of Mendez and Nicoud [125] on the sector has been added. The influence of the periodicity assumption is very small since the full and the sector computations give very close results. When comparing the simulation using the homogeneous model to the one with the thickened hole model, results are very different, the thickened-hole results

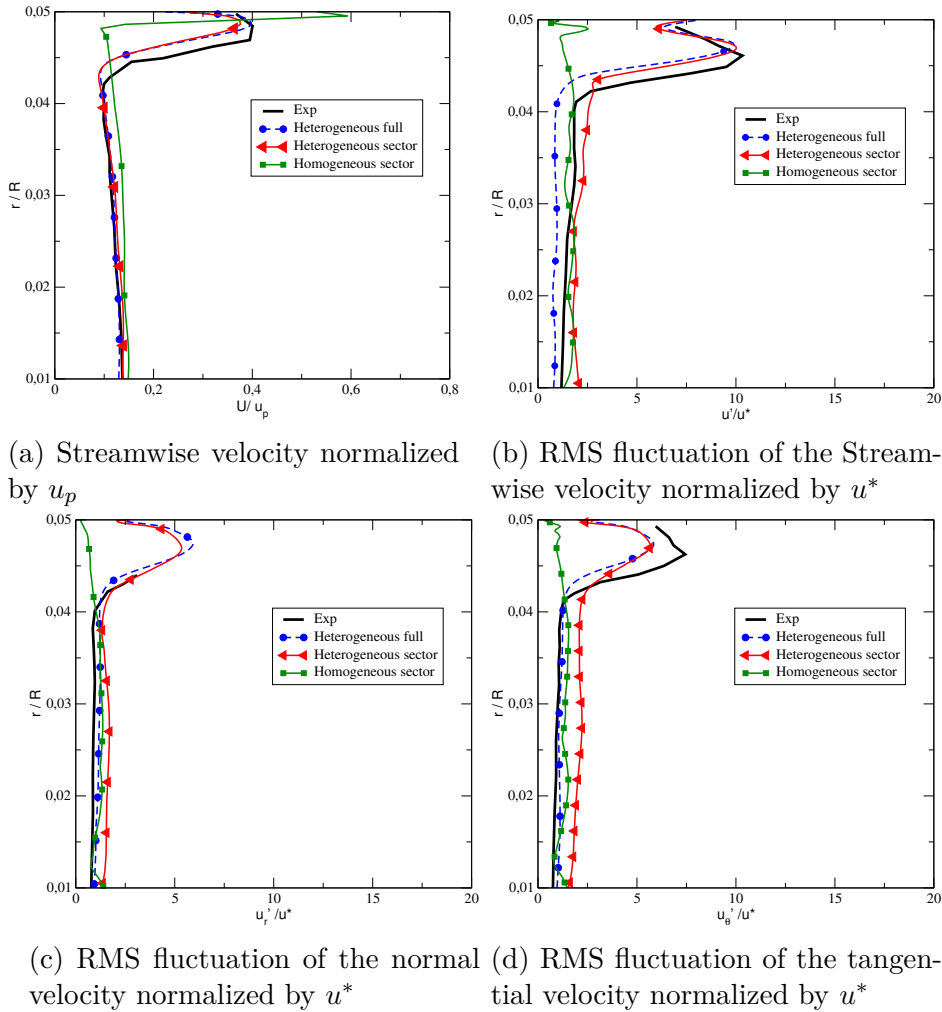


Figure 4.32: Comparison between experimental and numerical results of the velocities 4.1 mm after the multiperforated ring for the longitudinal Michel tube.

showing a much better agreement. On the contrary, the results from the homogeneous simulation overpredicts the streamwise velocity close to the wall and do not produces RMS fluctuations. This model does not predict the correct penetration and the mixing process in this case.

On Fig. 4.33, a cut 4.1 mm after the MP is presented. Time averaged results on one sector and on full  $360^\circ$  computation are compared. Both used the thickened-hole model. As raised before, the same conclusion can be drawn: in both cases, the flow is close. The effect of the sectorisation is thus limited. Note that jet wake are visible in this view.

In a more global view, when looking at the concentration of a passive scalar on the wall (Figs. 4.34a, 4.34b) and into the domain (Figs. 4.34d, 4.34c), homogeneous and thickened-hole models are very different. The most prominent effect is the apparition of jets on the wall. As already highlighted in section 4.1.3, the homogeneous

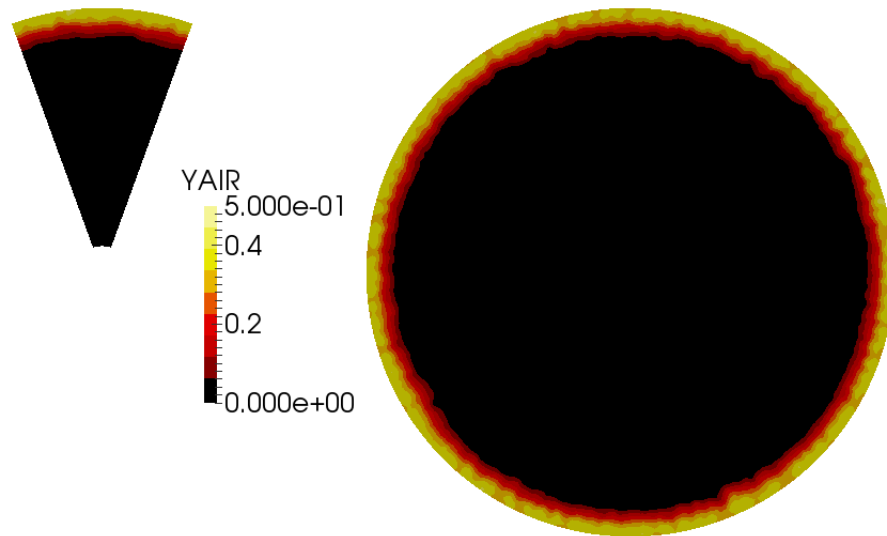


Figure 4.33: Comparison of the time averaged passive scalar concentration 4.1 mm after the multiperforated wall on a sector (left) and full 360° (right) in the longitudinal case, using thickened-hole model with  $R = 5$ .

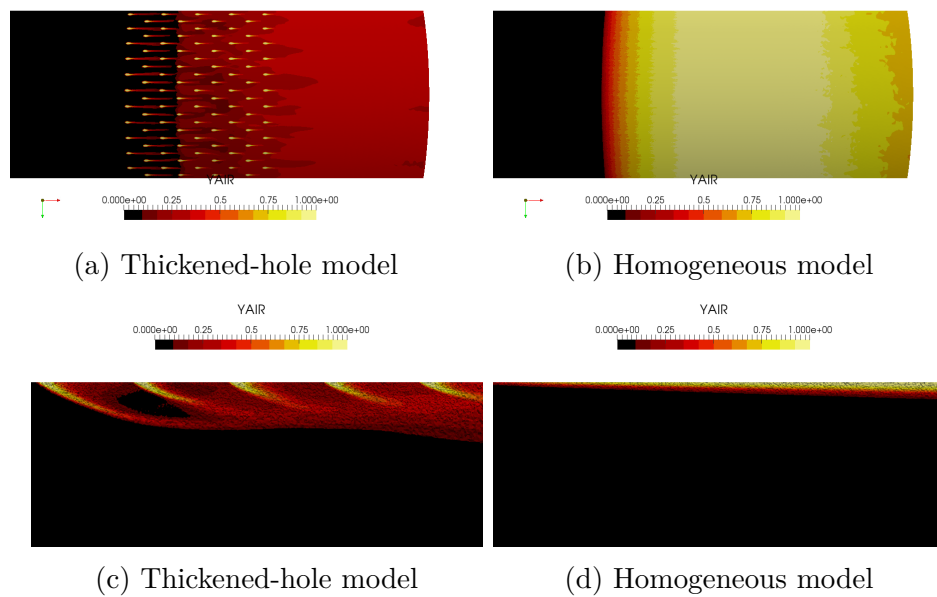


Figure 4.34: Longitudinal Michel tube. Comparison of the instantaneous passive scalar concentration and localisation between the two methods (thickened-hole model on the left and homogeneous one on the right). Visualisation of the wall (a) and (b) and into the domain when cutting through a row of multiperforation apertures (c) and (d).

model does not capture the correct mixing process. Since the heterogeneities are needed, to model effusion cooling both a reasonable resolution (about  $R=4$ ) and a realistic model (heterogeneous) are needed.

### 4.2.3 Michel tube with transverse cooling

Results have been previously shown small difference between a sector of  $40^\circ$  and a full  $360^\circ$  computation. From this conclusion and to reduce the computational cost in this section all the simulations will be performed on a  $40^\circ$  sector. Two computations with a deviation angle ( $\beta$ ) of  $90^\circ$  allowing to compare the multiperforation model on a transverse case has been performed (see Fig. 4.9). One using the thickened-hole model and one with the homogeneous model.

Multiperforated model	R	Sector	Cells	$\alpha$	$\beta$
Thickened-hole	5	$40^\circ$	39M	$30^\circ$	$90^\circ$
Homogeneous	5	$40^\circ$	39M	$30^\circ$	$90^\circ$

Table 4.9: Simulated setup for the transverse case.

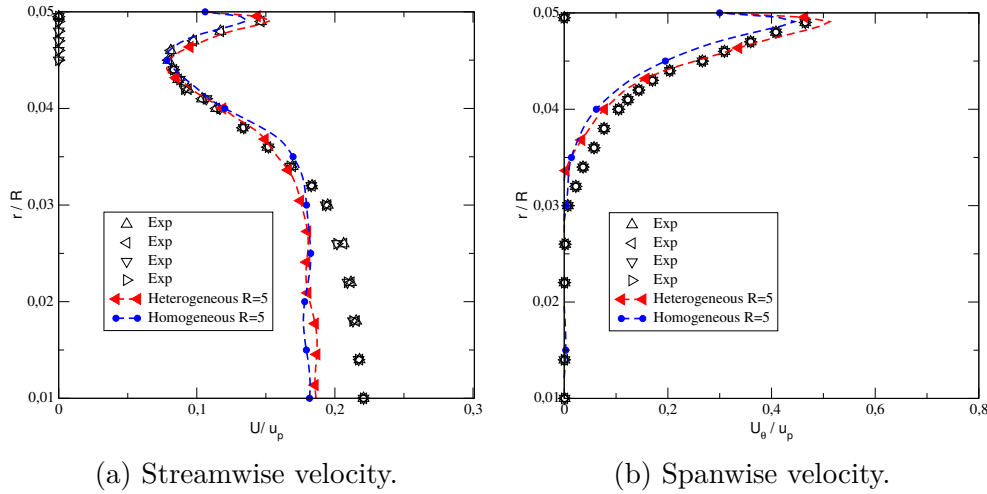


Figure 4.35: Comparison between experimental and numerical results of the velocities 4.1 mm after the multiperforated ring for the transverse case.

On Fig. 4.35, the streamwise and the spanwise velocity post processed with the space and time averaging presented above, 4.1 mm after the multiperforated plate is presented. Both models give very close results. For the streamwise velocity ( $U$ ) (see Fig. 4.35a), the experimental result in the transverse case is the opposite than for the longitudinal case where velocity increased near the wall. In the present case, the multiperforated plate blocks the flow which is thus slowed down near the wall. Thus, in order to keep the same flowrate, the velocity increases in the center of the domain. This overvelocity at the center is not captured by any model. The

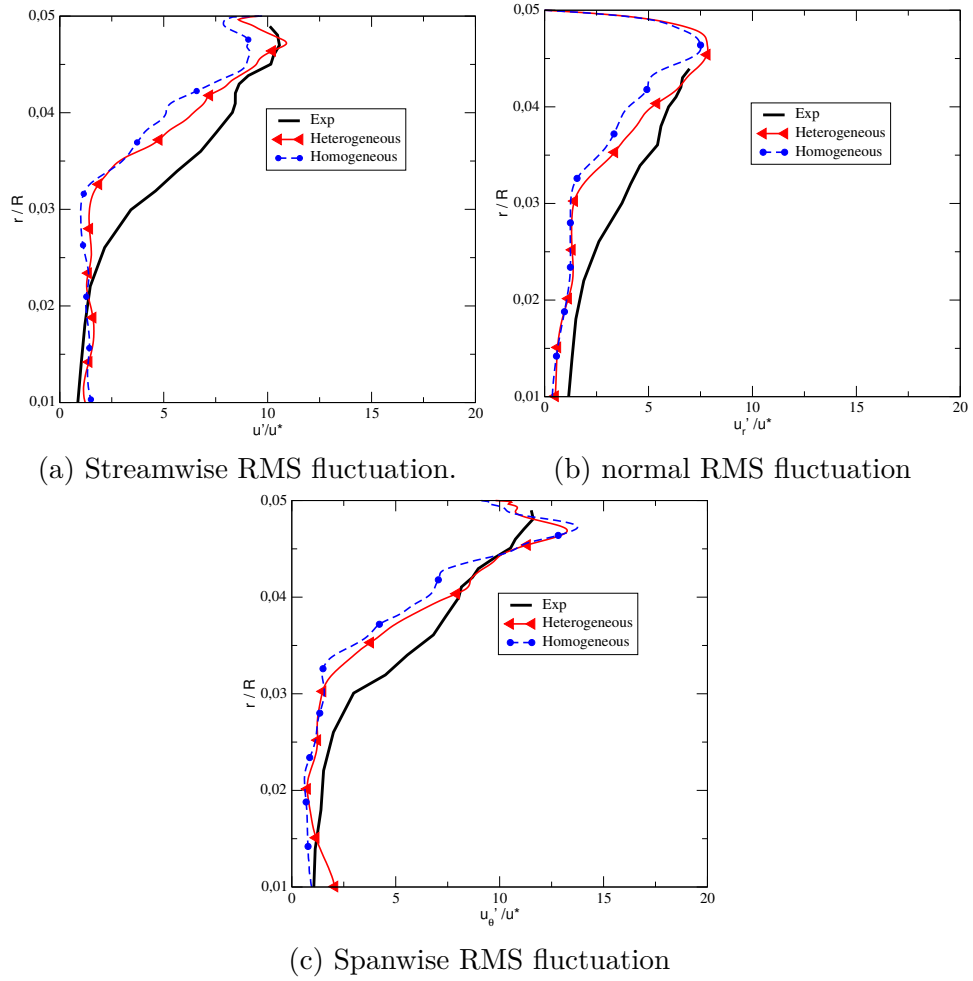


Figure 4.36: Comparison between experimental and numerical results of the fluctuations 4.1 mm after the multiperforated ring on the transverse case.

first reason could be the hypothesis of periodicity. However, the full  $360^\circ$  geometry simulation has not been performed for computational cost reasons and for the small gain in the final conclusion since the expected improvement would be limited on the center of the domain, *i.e.* far from multiperforated plate. When looking at the spanwise velocity ( $u_\theta$ ) (see Fig. 4.35b), for both methods, results are very close to experimental ones, whatever the radius. Note that the spanwise velocity is twice higher than the streamwise one and stays higher on more than 20% of the channel.

Figure 4.36 presents the RMS fluctuation in the three directions. For both models results are in good agreement with the experimental measurements. The level as well as the trend is correctly predicted.

The instantaneous 2D field for the thickened-hole and homogeneous models are compared on Fig. 4.37. Both are very close. The concentration close to the wall of the passive scalar is, however, more important in the homogeneous case. The time averaged 2D field is also presented on Fig. 4.38.

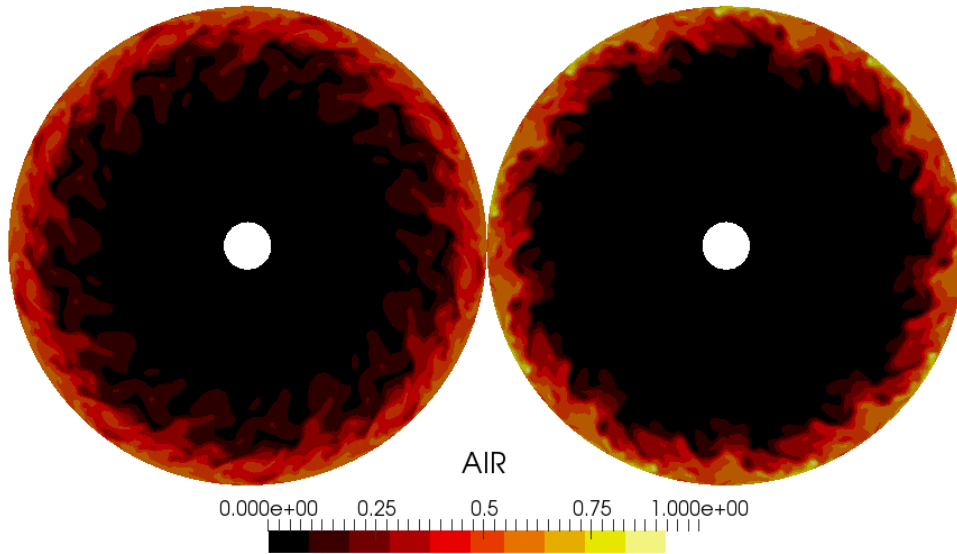


Figure 4.37: Michel tube with transverse cooling. Comparison of the instantaneous passive scalar concentration 4.1 mm after the muliperforated ring between thickened-hole model (left) and homogeneous model (right). The sector is duplicated nine times in order to represent the full geometry.

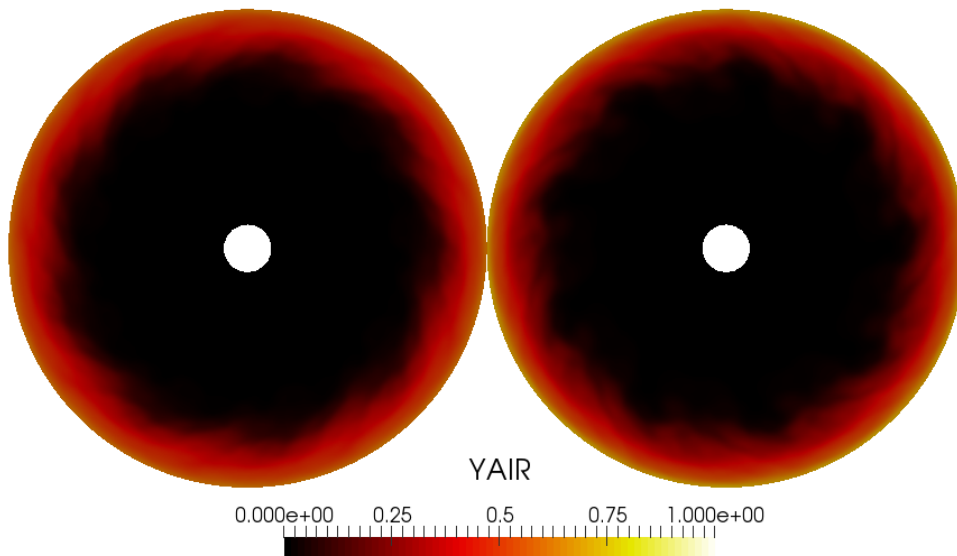


Figure 4.38: Michel tube with transverse cooling. Comparison of the averaged passive scalar concentration 4.1 mm after the muliperforated ring between thickened-hole model (left) and homogeneous model (right). The sector is duplicated nine times in order to represent the full geometry.

When looking at the part just before the multiperforated plate, a transverse flow is developing upstream. This phenomenon is not highlighted by Brice Michel since the apparatus of the experiment could not detect a high velocity rotating bubble upstream the ring. This phenomenon can change the inlet condition which is imposed for the numerical computation. Other studies performed at CERFACS with N3SNATUR and YALES2 led to the same result. As this question about the experimental configuration is crucial for the transverse case, present results have never been published.

The thickened-hole model has been validated thanks to a comparison between a numerical simulation and experimental results. Thickened-hole model gives better results than the homogeneous one on the longitudinal cooling case with  $R = 5$ , while they are equivalent on the transverse case. This observation has already been drawn on the Maveric test case. In parallel, this study also suggests that experimental measurements performed for the inlet quantities are not pertinent since the ring can influence the upstream flow.

### 4.3 Thickened-hole model capabilities

The thickened-hole model, presented in chapter 3 has been compared to fully resolved computations and to experimental observations. The influence of the deviation angle has been illustrated on both test cases. It illustrated that the cooling efficiency increases with the deviation angle ( $\beta$ ). But it also showed from a numerical point of view that longitudinal cooling is harder to predict. For high resolutions ( $R > 4$ ), the thickened-hole model is able to predict the global quantities as well as the RMS fluctuations with accuracy. Thanks to the variety of grid resolutions considered, the efficiency as a function of the grid size is given. It can be used as a guide to choose the R resolution, given the precision expected.

Note that results are presented for a uniform mesh resolution. However, the model is local (the cell size is taken from the mesh, not as an input parameter) and reacts to the local variation of the wall resolution. This property will be discussed in Part IV.

## Chapter 5

# Application to a Safran's combustion chamber, an academic combustor and a turbine blade

The thickened-hole model is currently used by Safran Helicopter Engine on various real configurations. An example is provided in this chapter on a TAF19, an early design of the Arrano engine. A result on an academic combustor, named FACTOR is also presented. At the end, the applicability of the thickened-hole model on cooled turbine blade performed by Harnieh *et al.* is proposed [79].

<b>5.1</b>	<b>Presentation of the test case . . . . .</b>	<b>82</b>
<b>5.2</b>	<b>Comparison between homogeneous and thickened-hole models on real combustor . . . . .</b>	<b>83</b>
<b>5.3</b>	<b>FACTOR Combustor test case . . . . .</b>	<b>84</b>
<b>5.4</b>	<b>Cooled Nozzle Guide Vanes (NGV) . . . . .</b>	<b>86</b>

## 5.1 Presentation of the test case

In this section, a turboshaft reverse flow combustion chamber, as in [24], is considered (see Fig. 5.1). A reactive simulation with adiabatic walls, in which effusion cooling is accounted for thanks to the thickened-hole model [29], has been performed with the LES solver AVBP. Such adiabatic simulation using modeled multiperforated plate is the standard in industry for predicting the combustor exit temperature profile or pollutant emissions. The objective of this section is to evaluate the benefit of the thickened-hole model compared to the homogeneous model, when it is applied on real combustor.

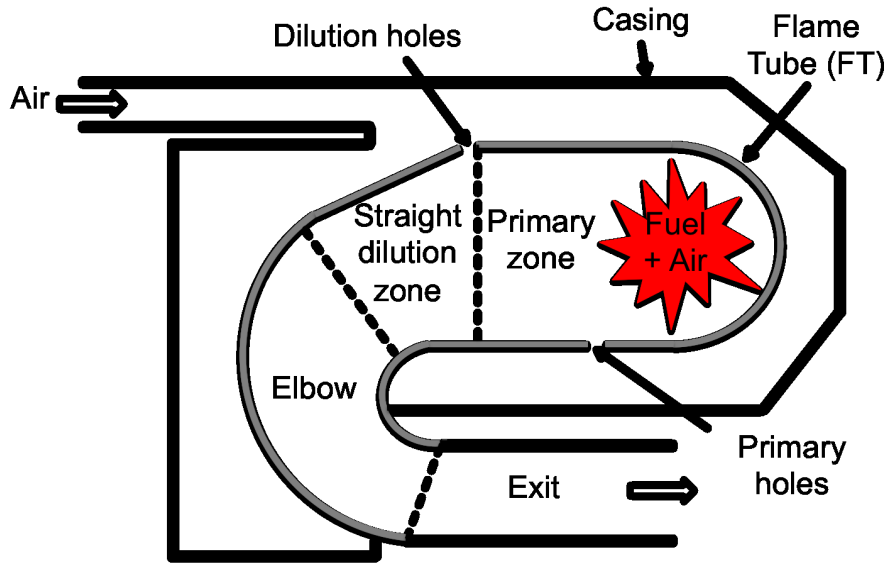


Figure 5.1: Schematic view of the combustor from [24] (same geometrical setup).

The periodicity of the configuration allows to consider only one sector of the combustion chamber, comprising one injector and several primary and dilution holes. The computation was performed on a 45 million elements mesh, with the grid size being of the order of the perforation diameter near the walls. The filtered Navier-Stokes equations were integrated thanks to an explicit Lax-Wendroff [106] numerical scheme, second order accurate in time and space. Combustion was described by the Thickened Flame Model [42] combined with the 2-step BFER kinetic scheme [65]. The Smagorinsky [166] model was also used to account for the subgrid-scale turbulence viscosity.

Ratio $R$	Cells	$\sigma_n$
0.75	45 892 340	0.06

Table 5.1: Characteristics of the mesh for the real combustor.

## 5.2. Comparison between homogeneous and thickened-hole models on real combustor

The mesh size is bigger than the diameter of the hole ( $\Delta x = 0.4$  mm and  $d = 0.3$  mm). If the thickened-hole model is used, holes are thus automatically thickened to  $d' = 1.2$  mm in order to obtain three cells in the aperture. Parameters are given in Table 5.1. A visualisation of the mesh is presented on Fig. 5.2 where injection surfaces (thickened hole) are visible.

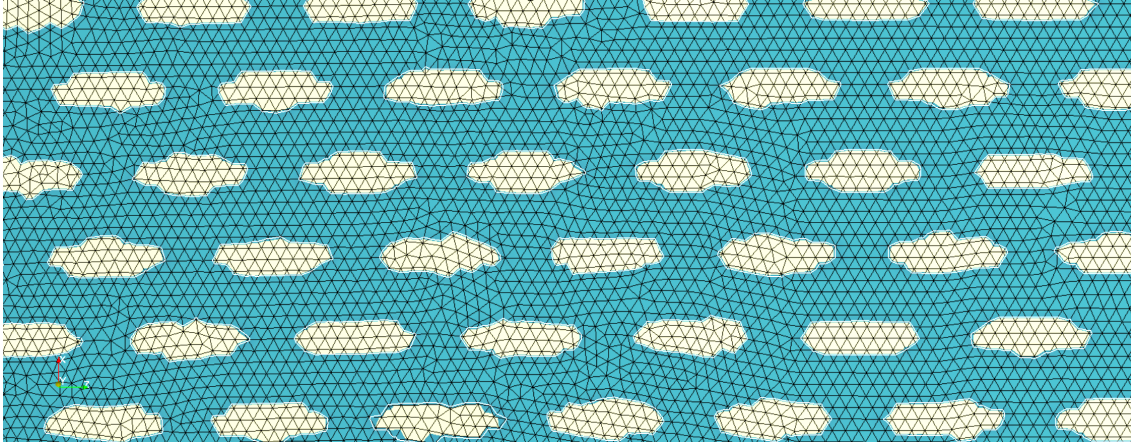


Figure 5.2: Visualisation of the boundary mesh. White zone corresponds to the injection surface.

## 5.2 Comparison between homogeneous and thickened-hole models on real combustor

In order to compare both models, the same computation, except for the effusion cooling part, has been performed with the homogeneous model [125] and with the thickened-hole model [29]. Visualisation of the time-averaged temperature field from the adiabatic simulation using homogeneous model is presented on Fig. 5.3. This figure also displays the name given to each zone of the engine.

Visualisation of the instantaneous wall temperature field is presented on Fig. 5.4. The adiabatic simulation using the homogeneous model (left) is very homogeneous and jets cannot be distinguished. On the contrary, on the adiabatic simulation using the thickened-hole model (right), jets can be identified. Also, even if both present the same patterns, the hot temperature zone seems bigger in the thickened-hole case. Note that holes are enlarged, as presented on Fig 5.2, which is still a limit when the goal is to be as close as possible to the real jets' size for a more accurate adiabatic temperature assessment.

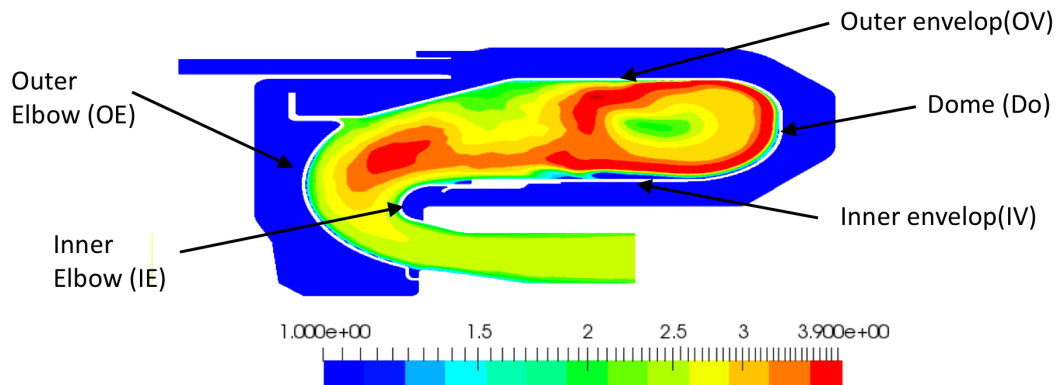


Figure 5.3: Non-dimensional mean fluid temperature field. Results from an adiabatic unresolved simulation using the homogeneous model.

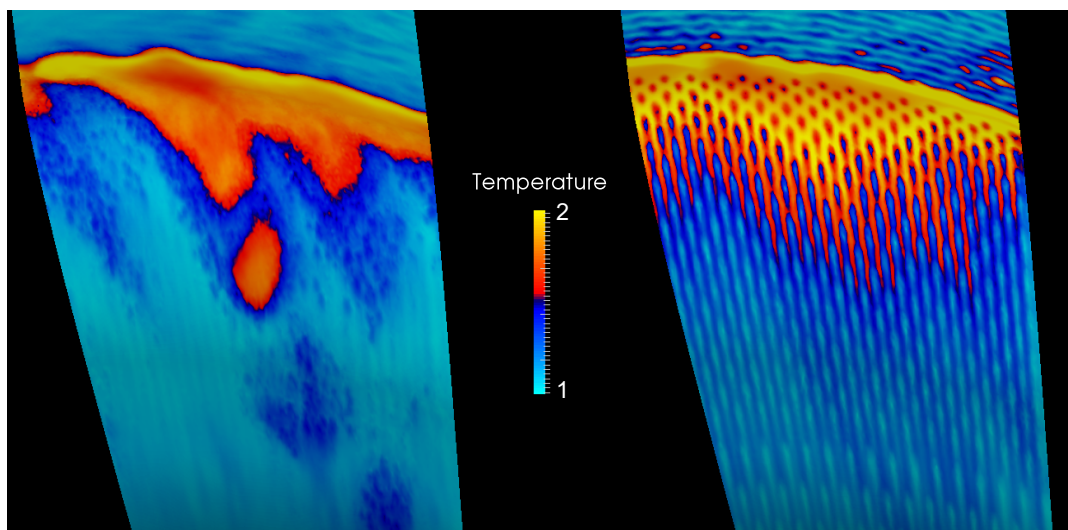


Figure 5.4: Visualisation of instantaneous wall temperature fields from an adiabatic simulation using the homogeneous model (left) and the thickened-hole model (right). The colorbar use fictive colours for confidentiality reasons.

### 5.3 FACTOR Combustor test case

The efficiency of the present model has also been tested on another combustor. It has been published in a conference proceedings [170]. The test case is presented on Fig. 5.6.

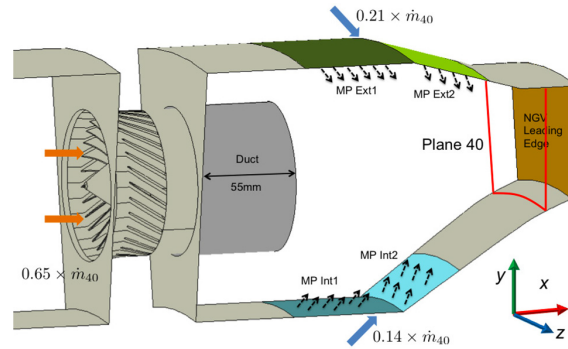


Figure 5.5: Representation of the FACTOR combustion chamber [96]

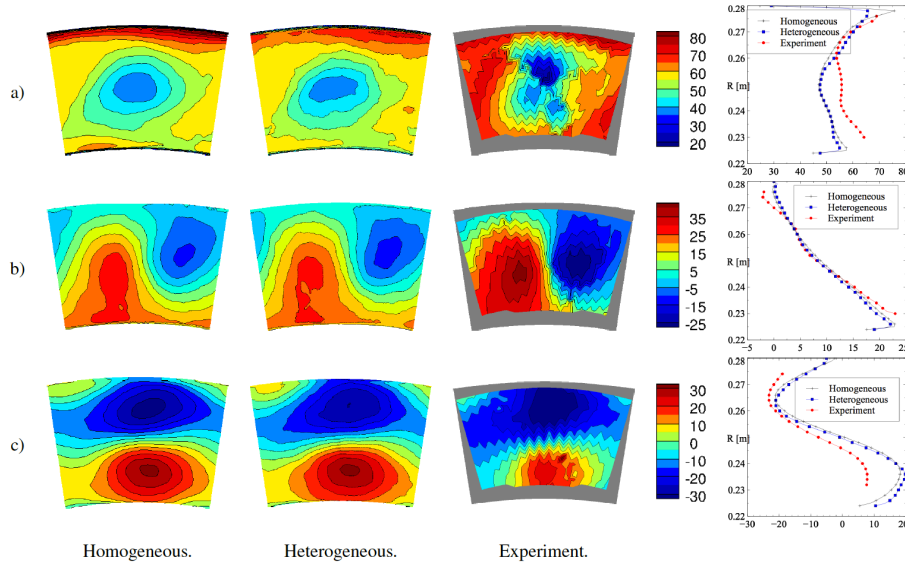


Figure 5.6: Temperature [K] on Plan 40 (defined on Fig. 5.6) for design point. View direction: Downstream. From [170]

Results using homogeneous [125] and thickened-hole [29] models (misleadingly called heterogeneous in the article [170] since the holes are enlarged) has been compared to experimental results. Both give results very close to the experiment. However, in the near wall region, the thickened-hole model leads to a more realistic representation of the cooling film. These results can be considered as an additional validation of the thickened-hole model.

## 5.4 Cooled Nozzle Guide Vanes (NGV)

The thickened-hole model has also been tested on a turbine blade by Harnieh *et al.* [79]. The goal was to test the applicability of the thickened-hole model (designed to handle effusion cooling in combustor) on turbine blades where the flow is totally different. The cooled turbine blade was first modelled using the thickened-hole model and the corresponding results compared to a hole-resolved LES where plenum and holes were taken into account. The mesh for the hole-resolved LES is composed of 67 million cells while there are only 37 million in the modelled case. The resolution between the two simulations was the same, the only difference being the plenum and the hole erased in the modelled case (see Fig. 5.7). As presented on Fig. 5.8, there are about 10 cells in the hole’s diameter ( $R = 10$ ), jets kept therefore their original diameter.

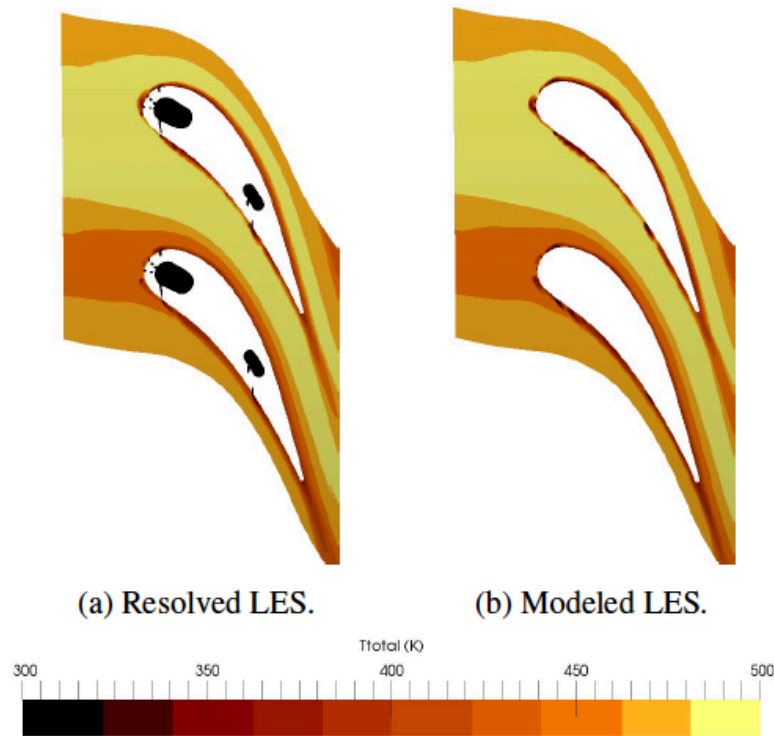


Figure 5.7: Time averaged total temperature field at the mid-height. Extrated from [79]

Figure 5.9 presents the wall temperature as well as isocontour of cooling. The first remark is that both flows are very close. Fluctuations are smaller in the modelled case. Indeed as highlighted in Harnieh *et al.* [79], the thickened-hole model does not inject fluctuations while, in the hole resolved case, the flow inside the pipe is turbulent and thus, RMS fluctuations are present at the exit of the hole. In addi-



Figure 5.8: Isosurface of the coolant jet allowing to visualize the boundary mesh in the modeled case. Extrated from [79]

tion, as presented in section 1.5.4, the profile at the exit of the hole is complex and far from a hyperbolic profile as injected by the thickened-hole model. This should be an improvement to the model which has not firstly been created to reach such precision.

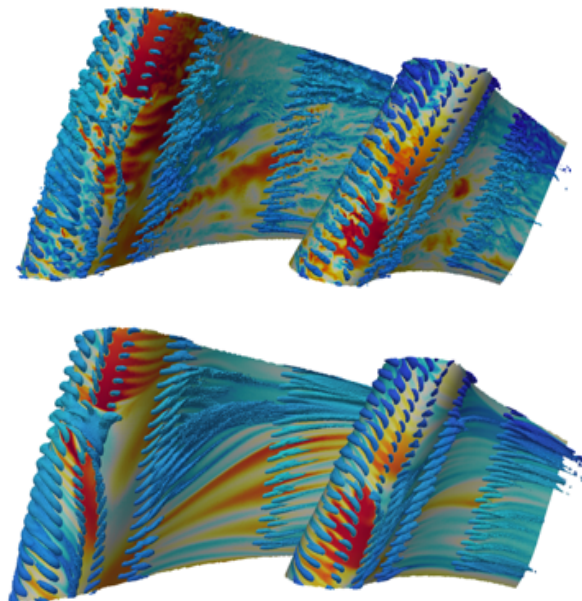


Figure 5.9: Full representation of the two simulated blades, the wall is coloured by the temperature. Also the isocontour of cooling is represented. Results from the hole resolved LES (top) and modelled one (bottom). Extrated from [79]

At the end, since both LES give very close results, the thickened-hole model can be a significant method for the design process. Indeed, it permits both an important CPU time saving and a design process enhancement compared to a resolved simulation where holes are meshed. In addition, with the thickened-hole model, many hole layouts can be tested using a single mesh of the blade.

## Part III

# Thermal modelling

## Chapter 6

# Conjugate heat transfer on a reference Maveric plate simulation

To understand the heat transfer process in aeronautic effusion cooling devices, an academic test case representative of helicopter's engines has been chosen. In this chapter, the contribution of each heat flux is studied thanks to a fully hole resolved conjugate heat transfer simulation extracted from the database of Lahbib. It shows that the adiabatic temperature from an effusion modelled simulation cannot be directly used to assess the wall's temperature. A surrogate method based on a robust estimator of the adiabatic temperature is proposed. All mentioned results and methods have been published in the International Journal of Heat and Mass Transfer (IJHMT) [30] and presented at the *Société Française de Thermique* (SFT) on March 15, 2018 [31].

<b>6.1</b>	<b>Description of the numerical softwares . . . . .</b>	<b>91</b>
6.1.1	The thermal solver: AVTP . . . . .	91
6.1.2	The coupler: OpenPalm . . . . .	91
<b>6.2</b>	<b>The fully resolved conjugate heat transfer simulation . . . . .</b>	<b>93</b>
<b>6.3</b>	<b>Comparison between conjugate heat transfer and the adiabatic simulations . . . . .</b>	<b>94</b>
6.3.1	Flow comparison between adiabatic and coupled flow . . . . .	95
6.3.2	Energy balance from the coupled simulation . . . . .	97
<b>6.4</b>	<b>Low order modeling of the plate temperature . . . . .</b>	<b>100</b>
<b>6.5</b>	<b>Estimation of the adiabatic temperature of the boundary layer . . . . .</b>	<b>103</b>
<b>6.6</b>	<b>Comparison of heat transfer modelling strategies . . . . .</b>	<b>105</b>
<b>6.7</b>	<b>A low-cost heat transfer modelling . . . . .</b>	<b>107</b>

A fully hole-resolved conjugate heat transfer simulation of the Maveric test case has been performed. For this purpose, a fluid solver (AVBP) already presented in Section 4.1.2 and a solid solver (AVTP) presented in the following section have been used and coupled. The communication between the two solvers is enforced thanks to a coupler (Open Palm) presented in the following section.

## 6.1 Description of the numerical softwares

### 6.1.1 The thermal solver: AVTP

The software AVTP solves the unsteady heat equation. It is derived from the previously described fluid code AVBP and shares its parallel treatment of unstructured hybrid grids. Therefore, the second order Galerkin diffusion scheme [53] for spatial discretisations comes from the AVBP solver. Time integration can be performed either with an explicit or an implicit approach. The implicit approach is used in the present work with a first order forward Euler scheme. Finally, the resolution of the implicit system is done with a parallel matrix free conjugate gradient method (Frayssé *et al.* [66]). The time step  $\Delta t$  determination is based on the diffusion velocity of the temperature from one cell to the next and ensures from the Fourier condition:

$$F = a \frac{\Delta t}{\Delta x^2} \quad (6.1)$$

with  $\Delta x$  the smallest cell size.

### 6.1.2 The coupler: OpenPalm

The Parallel Coupling Strategy (PCS) has been used to simulate multiperforated plate by Lahbib *et al.* [101, 100] but also by Florenciano and Bruel [61]. A schematic view of this strategy is presented on Fig. 6.1. This approach relies on two different solvers, each solving a medium (the flow or the plate), which exchange data at a common boundary interface thanks to a code coupler OpenPalm.

The OpenPALM code coupler [4, 154, 55] provides a library of functionalities allowing the creation of a frame work of independent code components or algorithms interacting with each other. The software is capable of handling different applications [157, 7]. Once an appropriate framework has been produced to address a specific physical problem, the software manages the execution scheduling of the various entities as well as the communications between them. The components may be executed in a sequential or concurrent way. For the present couplings, all the codes run concurrently: each of the components are launched at the beginning of the simulation and compute at the same time. During the execution, the exchange of

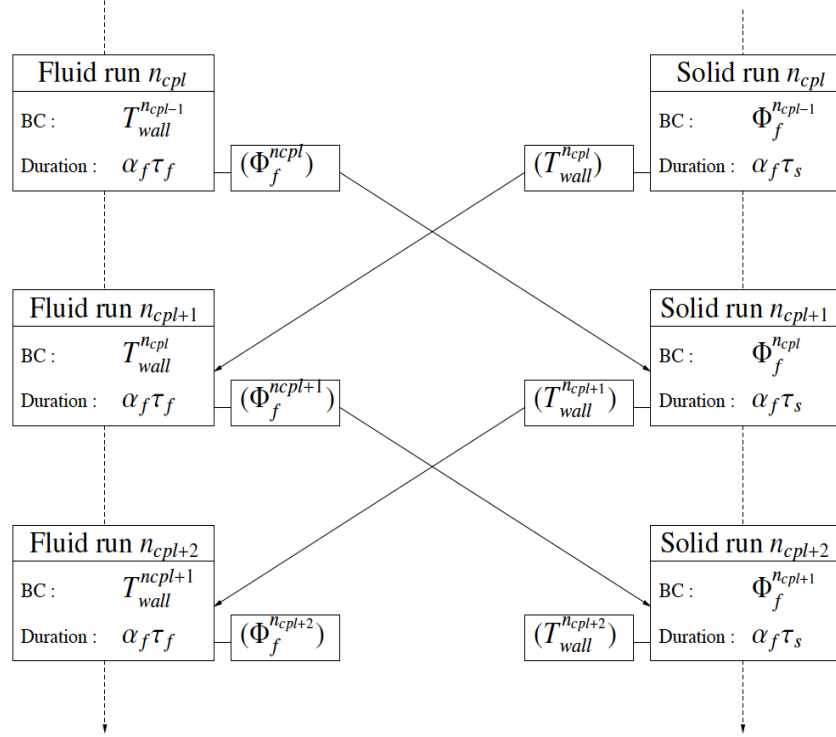


Figure 6.1: Parallel Coupling Strategy (PCS) between a fluid and a solid solver.

physical fields is handled by the CWIPI library [154] linked with OpenPALM. The various code interfaces are generally discretised on different and non-coincident grids and distributed on several computing cores. Therefore, a communication scheme is built between the cores allocated to the different solvers and physical fields are interpolated between grids [86]. As a result, the communication algorithm is split into two phases:

- An initialisation consisting in the determination of the inter-code communication routes and the interpolation coefficients.
- A communication phase during which physical fields are interpolated and exchanged.

For applications that do not involve moving meshes (hence for which the inter-code communication scheme and interpolation coefficients do not vary in time), the initialisation phase is only performed once at the beginning of the computation. Then, during the communication phases, the cores allocated to the different codes exchange data directly via point-to-point MPI communications.

This fully distributed method was shown to ensure a good scalability of the coupled application [87] compared to a method where all the information to exchange is gathered on one computing core.

The coupling of the LES and conduction solvers is achieved following the methodology of Jauré *et al.* [88] both in terms of data exchanged and frequency. Coupling libraries, embedded within the solvers, ensure the information exchange between the two entities. The convective heat flux  $q_{conv}$  is provided by the fluid domain to the solid one which gives back a wall temperature  $T_{wall}$  to the fluid domain. To ensure the performance of the coupling, the parallel coupler OpenPALM developed by CERFACS and ONERA is used [55]. The coupling strategy has been validated and used in previous works of Duchaine *et al.* [56] and Berger *et al.* [24].

## 6.2 The fully resolved conjugate heat transfer simulation

Two meshes have been used, a solid and a fluid one which properties are defined in Table 6.1. The database (the conjugate heat transfer simulation) has been created during the PhD of Lahbib [100].

Fluid cells mesh	Solid cells mesh	CPU cost (h)
$5 \times 10^7$	$5 \times 10^6$	300 000

Table 6.1: Summary of the meshes used; one for the fluid and one for the solid.

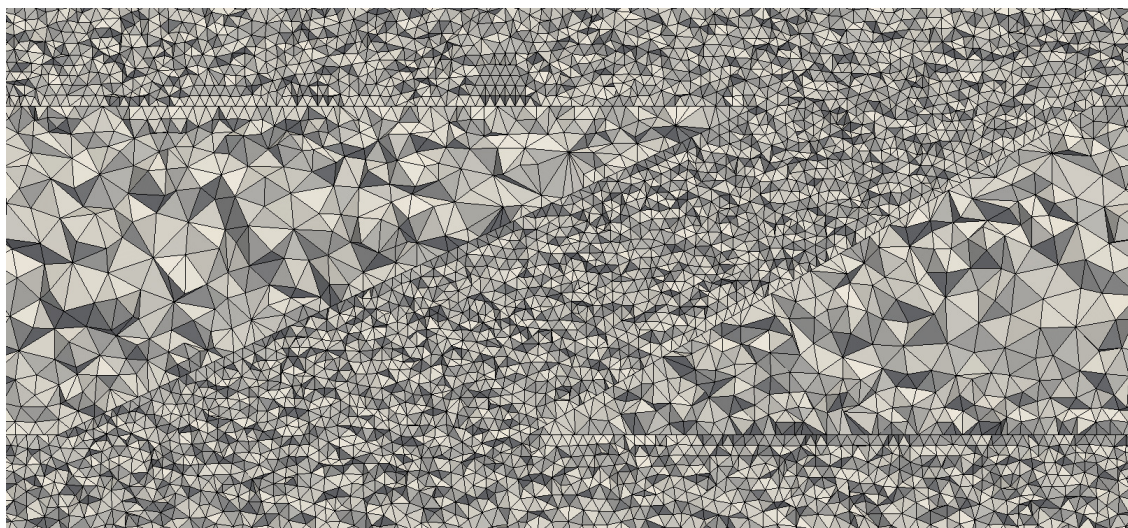


Figure 6.2: Visualisation of the meshes for the fully resolved conjugate heat transfer simulation. Fluid and solid meshes are displayed.

The fully resolved conjugate heat transfer simulation is denoted "resolved coupled". Main characteristics are given in Table 6.1. Holes are explicitly represented together with both the suction and injection sides; both the flow equations (in the fluid domain) and heat equation (in the solid domain) are solved. The mesh used for the fluid is such that the number of cells per aperture diameter is at least 25 in the injection side (more in the suction side due to the conical shape of the holes, see Fig 4.2). In wall units ( $y^+$ ), the first off wall point distance is less than 12 in the aperture, of the order of 5-6 elsewhere. In the solid domain (used only for the resolved coupled simulation), the mesh contains  $5 \times 10^6$  tetrahedral cells which are smaller near the interface for coupling interpolation purposes (see Fig. 6.2). Results from the fully resolved conjugate heat transfer simulation are presented on Fig. 6.3.

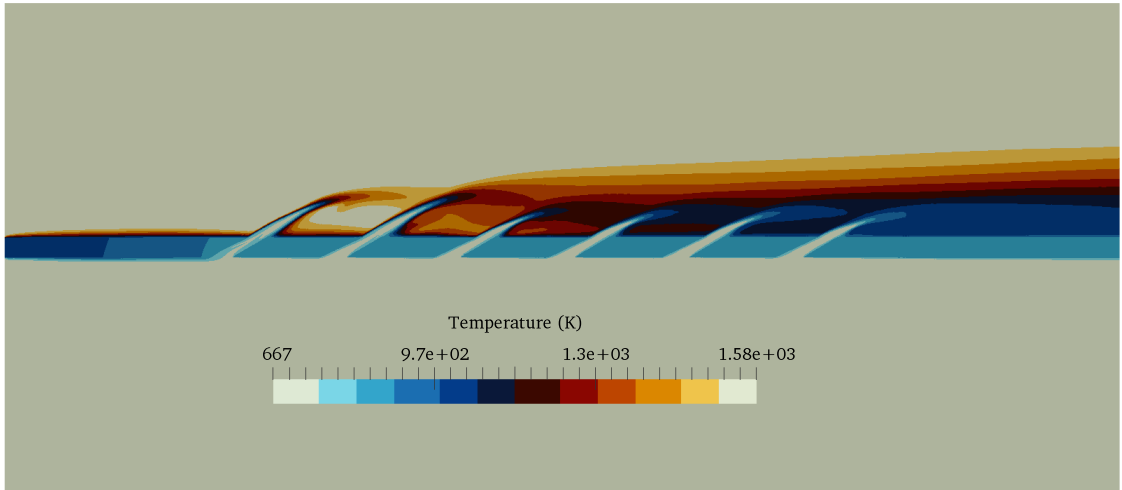


Figure 6.3: Result of the conjugate heat transfer simulations. A 2D cut through a row is presented. Fluid and solid part are displayed.

### 6.3 Comparison between conjugate heat transfer and the adiabatic simulations

Another hole-resolved computation for the fluid domain where adiabatic conditions are used at the multi-perforated plate surfaces and denoted "resolved adiabatic" is performed. The characteristics of the fluid mesh are the same as for the resolved coupled simulations whose main characteristics have been given in Table 6.1. The CPU cost of the coupled simulation is twice the adiabatic one due to the convergence of the solid temperature. The CPU cost, for each simulation is reported in table 6.2.

Simulation	CPU (h)
Resolved coupled	300 000
Resolved adiabatic	150 000

Table 6.2: Comparison of the CPU costs.

### 6.3.1 Flow comparison between adiabatic and coupled flow

A first qualitative comparison can be performed by comparing a two dimensional cut through a row. It can be seen on Fig. 6.4 that both flow fields are very close. The only difference can be seen close to the wall and into the primary holes where the fluid is either pre-heated or pre-cooled depending on the side.

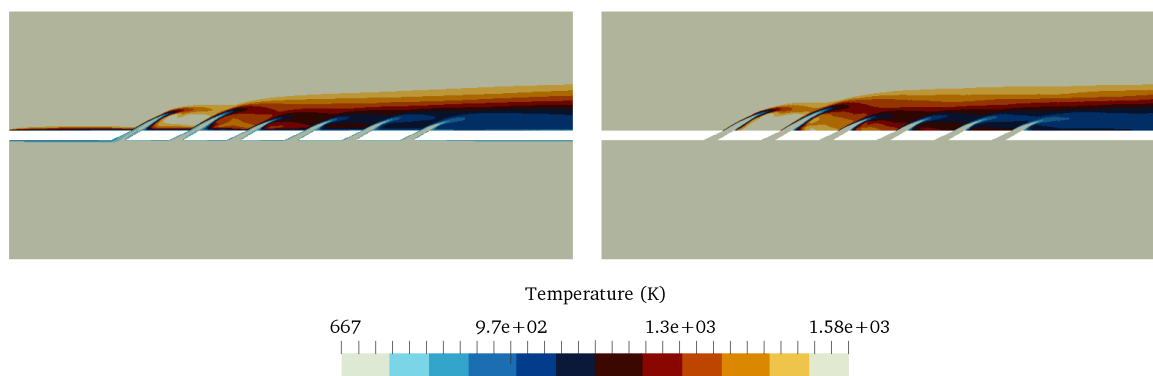


Figure 6.4: Comparison between conjugate heat transfer (left) and adiabatic (right) simulations. Only the fluid domain is displayed.

To assess quantitatively the difference between the resolved coupled and adiabatic computations, temperature and axial mass flowrate profiles are presented. 3D data are time and spanwise averaged and presented as a function of  $Y^*$ , the distance from the plate normalised by the inter-row distance  $\Delta$  defined on Fig. 6.5 ( $\Delta = 11.68d$ ). Figure 6.5 shows such profiles at four axial positions along the multi-perforated plate, in the injection side. The first two positions correspond to the third and tenth rows. The last two positions correspond to 3 and 25 diameters downstream of the last perforation where the film is no more fed by coolant injection.

Overall, the results show a marginal effect of the thermal coupling on the flow quantities. The only significant effect is seen on the temperature profiles for  $Y^* < 0.05$  where the isothermal condition induces strong temperature gradients.

Assuming adiabaticity for liners is therefore acceptable when focusing on engine performances. On the contrary, adiabatic calculations underestimate the temperature drop close to the wall, which is critical when focusing on the wall temperature.

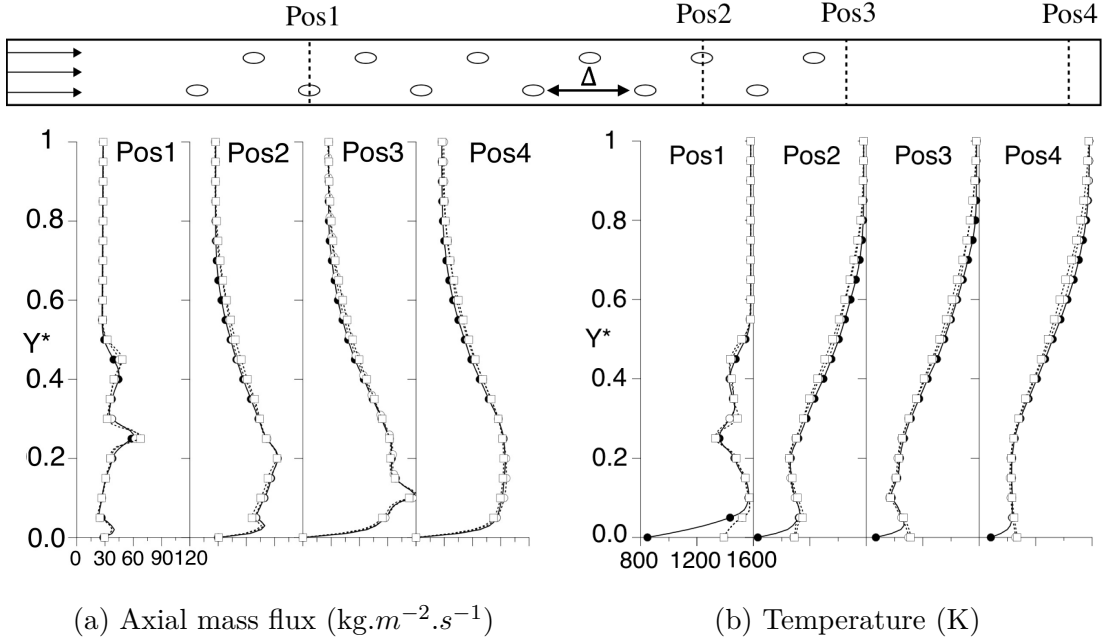


Figure 6.5: Comparison of the time average and laterally line averaged profiles for the different cases.  $\bullet$ : resolved coupled calculation,  $\square$ : resolved adiabatic calculation. The ordinate axis is the non-dimensional height  $Y^*$ , the ratio between the wall distance  $y$  and the inter-row distance  $\Delta$ .

According to Florenciano and Bruel [61], the Biot number of the Maveric plate is very small ( $\approx 0.013$ ), meaning that the temperature variation across the wall thickness is neglected. To first order, on both sides of the multi-perforated plate ( $T_{wall\ hot} = T_{wall\ cold} = T_{wall}$ ). In addition, in all this study, the wall temperature is averaged in the spanwise direction. Thus, the wall temperature depends only on the streamwise location,  $T_{wall} = T_{wall}(x)$ . As shown in Fig. 6.6, this approximation is indeed well supported by the resolved coupled simulation. The mean difference between  $T_{wall\ hot}$  and  $T_{wall\ cold}$  is about  $6.9\text{K}$ , which is less than 1% of the difference between  $T_{hot}$  and  $T_{cold}$ . In contrast, the resolved adiabatic simulation leads to adiabatic temperature distributions which are significantly different between the suction and injection sides of the plate. The adiabatic temperature on the suction side remains close to the cold temperature  $T_{ad\ cold} \approx T_{cold}$  (see Fig. 6.6).

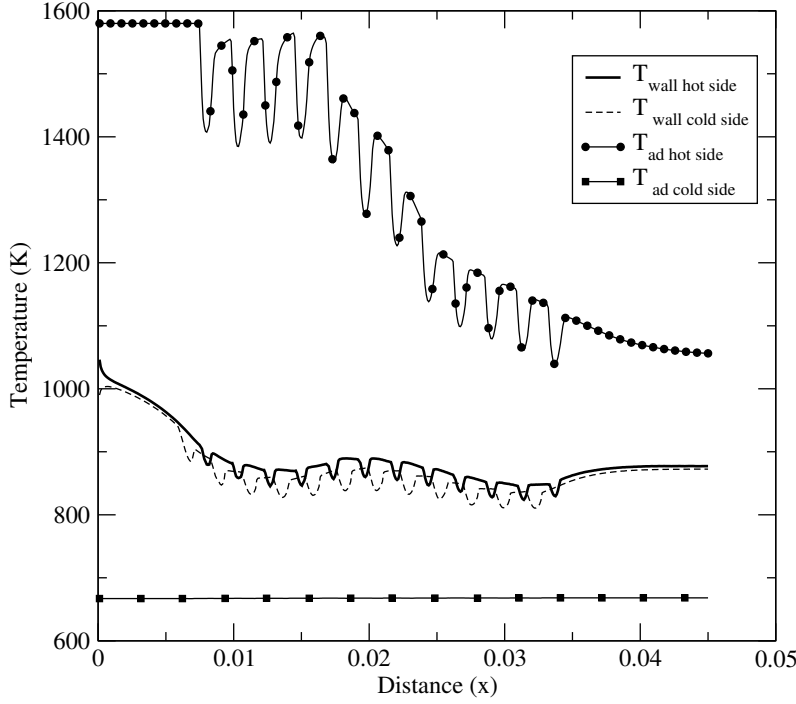


Figure 6.6: Evolution of the time and spanwise averaged temperature for the resolved coupled case and the resolved adiabatic case.

### 6.3.2 Energy balance from the coupled simulation

A proper methodology to assess the temperature of the plate under realistic conditions must account for the main contributors in the energy balance. A quantitative analysis of the heat transfers within the plate is achieved by considering the energy budget over two control volumes encompassing the perforated liner solid part and the fluid inside the apertures respectively, as shown in Figs. 6.7 and 6.8. The control volume for the solid medium starts at  $\Delta x/2$  upstream of the first row and finishes at  $\Delta x/2$  downstream of the last row of holes. The subscripts 1 and 2 refer to the injection and suction sides respectively. Denoting by  $s_1$  and  $s_2$  the hole outlet and inlet surfaces,  $\bar{s}_1$  and  $\bar{s}_2$  correspond to the liner surfaces in contact with the hot and cold crossflows respectively while  $s_u$  and  $s_d$  represent the upstream and downstream surfaces of the plate. The solid and fluid volumes of control can exchange heat through their common interface  $s_h$ , which is the inner surface of each aperture. Flux exchanged by the two media are recalled in Fig. 6.7 and Fig. 6.8 where the inward normal relative to the fluid and solid domains are denoted by  $\vec{n}_f$  and  $\vec{n}_s$  respectively.

The diffusive flux in the fluid is noted as  $\overrightarrow{q_{diff}}$ , the convective flux on each side of the plate as  $\overrightarrow{q_{conv}}$  (see Fig. 6.3). The fluid-solid flux through the aperture is noted as  $\overrightarrow{q_{hole}}$  while the same flux through the liner's surface is called  $\overrightarrow{q_{diff}^*}$ . The conductive

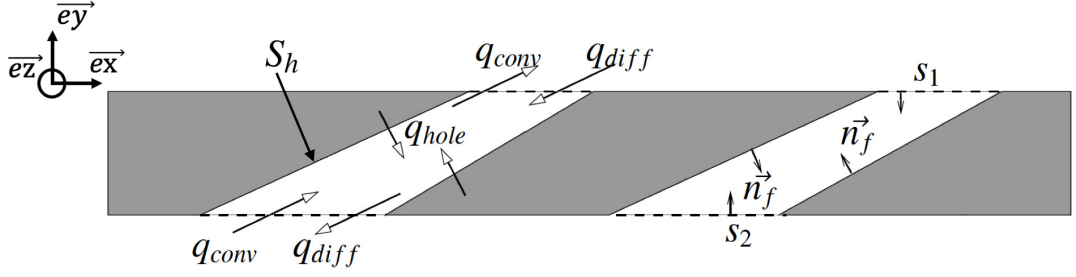


Figure 6.7: Representation of the different fluxes and the inward normal of the fluid control volume.

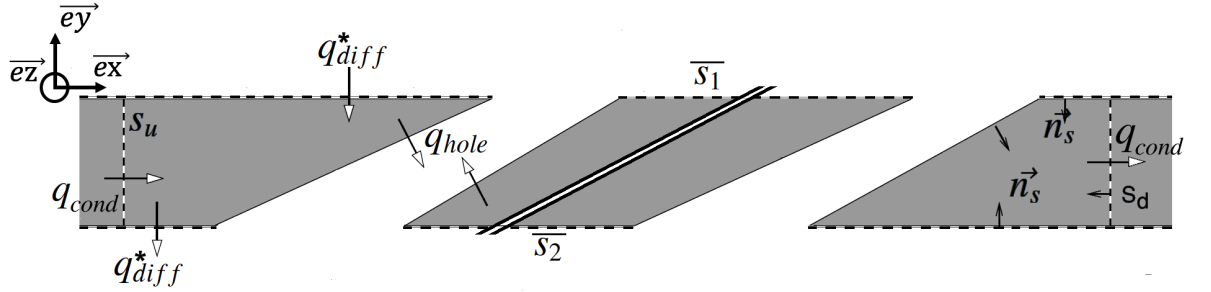


Figure 6.8: Representation of the different fluxes and the inward normal of the solid control volume.

flux within the solid is denoted by  $\overrightarrow{q_{cond}}$ . The fluid velocity vector is referred as  $\overrightarrow{V}$ , its components will be denoted  $U$ ,  $V$ ,  $W$  for the streamwise, normal, and spanwise directions respectively. The total energy ( $H_t = E_t + P/\rho$  where  $E_t$  is the total energy,  $P$  the pressure and  $\rho$  the density of the fluid) equation integrated over the control volumes and over time yields Eqs. 6.2 and 6.3 for the fluid and solid media, respectively:

Flux	Applicable surface	Expression	Modelling expression
$\overrightarrow{q_{conv}}$	$s_1, s_2$ (hole surface)	$\rho E_t \overrightarrow{V}$	N/A
$\overrightarrow{q_{diff}}$	$s_1, s_2$ (hole surface)	$-\lambda_s \overrightarrow{\nabla} T$	N/A
$\overrightarrow{q_{diff}^*}$	$\overline{s}_1, \overline{s}_2$ (wall surface)	$-\lambda_s \overrightarrow{\nabla} T$	$h \overrightarrow{\nabla} T$
$\overrightarrow{q_{hole}}$	$s_h$ (inner hole surface)	$-\lambda_s \overrightarrow{\nabla} T$	$h \overrightarrow{\nabla} T$
$\overrightarrow{q_{cond}}$	$s_u, s_d$ (plate surface)	$-\lambda_s \overrightarrow{\nabla} T$	N/A

Table 6.3: Definition of involved flux.

$$\int_{s_{1,2}} \rho E_t \vec{V} \cdot \vec{n}_f dS + \int_{s_{1,2}} P \vec{V} \cdot \vec{n}_f dS + \int_{s_{1,2}} \overrightarrow{q_{diff}} \cdot \vec{n}_f dS + \int_{S_h} \overrightarrow{q_{hole}} \cdot \vec{n}_f dS - \int_{s_{1,2}} (\bar{\tau} \cdot \vec{V}) \cdot \vec{n}_f dS = 0 \quad (6.2)$$

$$\int_{s_{u,s_d}} \overrightarrow{q_{cond}} \cdot \vec{n}_s dS + \int_{\overline{s_{1,2}}} \overrightarrow{q_{diff}^*} \cdot \vec{n}_s dS + \int_{s_h} \overrightarrow{q_{hole}} \cdot \vec{n}_s dS = 0 \quad (6.3)$$

The viscous tensor is defined as  $\bar{\tau} = 2\mu S - \frac{2}{3}\mu \text{tr}(S)\mathbb{I}$  where  $S = \frac{1}{2}(\nabla \vec{V} + \nabla \vec{V}^T)$  is the strain rate tensor and  $\mathbb{I}$  the  $3 \times 3$  identity matrix. The diffusive fluxes,  $\overrightarrow{q_{diff}}$  and the conductive flux,  $\overrightarrow{q_{cond}}$ , are modeled thanks to the Fourier's law ( $\vec{q} = -\lambda_s \nabla T$ ) where  $\lambda_s$  is the thermal conductivity of the appropriate medium. Splitting Eq. 6.2 into three parts in order to underline the contribution of each surface yields:

$$\int_{s_2} \left( \rho H_t \vec{V} - \lambda_s \nabla T - \bar{\tau} \vec{V} \right) \cdot \vec{n}_f ds + \int_{s_1} \left( \rho H_t \vec{V} - \lambda_s \nabla T - \bar{\tau} \vec{V} \right) \cdot \vec{n}_f ds + \int_{s_h} \overrightarrow{q_{hole}} \cdot \vec{n}_f dS = 0. \quad (6.4)$$

Since  $\vec{n}_f = \vec{e}_y$  on  $S_2$  and  $\vec{n}_f = -\vec{e}_y$  on  $s_1$ , Eq. 6.4 leads to:

$$\int_{s_2} \left( \rho H_t V - \lambda_s \frac{\partial T}{\partial y} - (\bar{\tau} \cdot \vec{V})_y \right) ds - \int_{s_1} \left( \rho H_t V - \lambda_s \frac{\partial T}{\partial y} - (\bar{\tau} \cdot \vec{V})_y \right) ds + \int_{s_h} \overrightarrow{q_{hole}} \cdot \vec{n}_f dS = 0, \quad (6.5)$$

where  $(\bar{\tau} \cdot \vec{V})_y = \tau_{xy}U + \tau_{yy}V + \tau_{zy}W$  is the normal component of  $(\bar{\tau} \cdot \vec{V})$ .

Note that the viscous contributions in the integral over  $s_1$  and  $s_2$ ,  $\lambda_s \frac{\partial T}{\partial y}$  and  $(\bar{\tau} \cdot \vec{V})_y$ , can be neglected in front of the inviscid contribution  $\rho H_t V$  (they represent less than 0.1%, not shown). Thus, Eq.6.5 becomes:

$$\int_{s_2} \rho H_t V ds - \int_{s_1} \rho H_t V ds + \int_{s_h} \overrightarrow{q_{hole}} \cdot \vec{n}_f dS = 0. \quad (6.6)$$

Table 6.4 displays the values of the three terms in Eq. (6.6) and shows that the energy budget over the aperture is reasonably well balanced. The absolute error is  $0.8W$  corresponding to 0.3% of the energy flux penetrating the hot flow. (10% when compared to the thermal power exchanged within the aperture). The figures in Table 6.4 also show that the fluid flowing through the apertures is slightly heated by the plate, the gain (the  $s_h$  integral term) being  $\approx 4\%$  of the total heat flux flowing through the plate. This contributes to the cooling of the plate, on top of the shielding effect often put forward.

The energy budget for the solid medium is also well balanced, as illustrated by the values of the contributions to Eq. 6.3 reported in Table 6.5. In a first approximation, the heat extracted within the apertures ( $\overline{s_h}$  integral term) is compensated

Expression	$\int_{s_2} \rho H_t V ds$	$\int_{s_1} \rho H_t V ds$	$\int_{s_h} \overrightarrow{q_{hole}} \cdot \overrightarrow{n_f} ds$
Contribution (W)	221.0	230.0	8.2

Table 6.4: Time averaged wall energy fluxes. Expression and values of the fluxes (in W) relevant to the fluid domain.

by the difference between the diffusive fluxes on both plate faces, as it would be the case for an infinitely long plate without side effect. The flux transferred to the fluid within the perforations ( $\int_{s_h} \overrightarrow{q_{hole}} \cdot \overrightarrow{n_f} ds$ ) represents about 44% of the flux entering the plate at the injection side ( $\int_{s_1} \overrightarrow{q_{diff}^*} \cdot \overrightarrow{n_s}$ ). This is in good agreement with Cottin's conclusion [45]. The longitudinal diffusion  $\overrightarrow{q_{cond}}$  is smaller than the normal diffusion  $\overrightarrow{q_{diff}^*}$  though not negligible at the ends of the plate and locally near the holes (not shown here). The perforated portion of the plate is the coldest part of the plate, explaining why the conductive heat flux at both ends of the plate  $q_{cond}$  is positive (contributions of  $s_d$  and  $s_u$  in Table 6.5).

Expression	$\int_{s_h} \overrightarrow{q_{hole}} \cdot \overrightarrow{n_s} ds$	$\int_{s_1} \overrightarrow{q_{diff}^*} \cdot \overrightarrow{n_s} ds$	$\int_{s_2} \overrightarrow{q_{diff}^*} \cdot \overrightarrow{n_s} ds$	$\int_{s_u} \overrightarrow{q_{cond}} \cdot \overrightarrow{n_s} ds$	$\int_{s_d} \overrightarrow{q_{cond}} \cdot \overrightarrow{n_s} ds$
Value (W)	-8.2	18.6	-11.7	0.9	0.4

Table 6.5: Flux contributions to the energy budget of heat equation in the solid medium. The first term is the opposite of the last column in Table 6.4.

For the operating point considered, the convective fluxes play a significant role. At the injection side, from the fluid point of view, the solid only contributes to 8.1% of the fluid energy flux ( $\int_{s_1} \overrightarrow{q_{diff}^*} \cdot \overrightarrow{n_s} ds$  in Table 6.5 compared to  $\int_{s_1} \rho H_t V ds$  in Table 6.4). Similar conclusions were drawn by Mendez and Nicoud [125] regarding the weak contribution of the viscous flux on the dynamics around the plate. For this range of operating point, a first order thermal model for effusion should focus on the inviscid part of the heat flux. The fact that the heat transfer through the solid represent less than 10% of the total energy exchanged between the cold and hot streams also justifies why the resolved adiabatic and coupled simulations lead to very similar results (see Section 6.3.1). This conclusion is obviously limited to the present operating point, M, J and geometry.

## 6.4 Low order modeling of the plate temperature

As showed in Sections 6.3.1 and 6.3.2, the heat transfer through the solid is moderate compared to the convective flux through the apertures. Therefore, an adiabatic computation provides a fair description of the flow field relevant to the coupled case. This shows that it might be possible to build a reasonable assessment of the wall temperature by analyzing an adiabatic computation. At steady state, the sum of the heat fluxes entering the multi-perforated plate are balanced. From Table 6.5,

the three main contributors to the heat budget are the diffusive heat fluxes over the cold and hot side of the plate and within the apertures. Thus, the following global relation for the plate should hold to first order without diffusion heat fluxes at extremities:

$$-\int_{\bar{s}_1} \overrightarrow{q_{diff}^*} \cdot \overrightarrow{n_s} ds \approx \int_{\bar{s}_2} \overrightarrow{q_{diff}^*} \cdot \overrightarrow{n_s} ds + \int_{s_h} \overrightarrow{q_{hole}} \cdot \overrightarrow{n_s} ds. \quad (6.7)$$

Introducing the heat transfer coefficients  $h_{hot}$ ,  $h_{cold}$  and  $h_{hole}$  to model these fluxes and considering that  $T_{ref\ hot} = T_{ad\ hot}$ ;  $T_{ref\ cold} = T_{cold}$  and  $T_{ref\ hole} = T_{cold}$  leads to:

$$h_{hot}(\overline{T_{wall}} - \overline{T_{ad\ hot}})\bar{s}_1 \approx (\overline{T_{cold}} - \overline{T_{wall}}) (h_{cold}\bar{s}_2 + h_{hole}s_h), \quad (6.8)$$

where  $\overline{T_{wall}}$  corresponds to the space averaged value of the wall temperature. The assumption  $T_{ref\ hole} = T_{cold}$  is justified by the fact that the boundary layer on the suction side is continuously sucked along the plate. Thus the solid is always exposed to  $T_{cold}$  on this side. This is well supported by the results of Fig. 6.6.

A simple model for assessing the temperature of the plate ( $\overline{T_{wall}^{model}}$ ) could thus have the form:

$$\overline{T_{wall}^{model}} = \frac{\overline{T_{cold}} + R_{th}\overline{T_{ad\ hot}}}{1 + R_{th}}, \quad \text{with} \quad R_{th} = \frac{h_{hot}\bar{s}_1}{h_{cold}\bar{s}_2 + h_{hole}s_h}. \quad (6.9)$$

Using Eq. 6.9 to assess the wall temperature requires the knowledge of  $R_{th}$  and  $\overline{T_{ad\ hot}}$ .  $R_{th}$  can be recovered from correlations and from geometrical parameters (function of the porosity). The following values for the heat transfer coefficients can be determined from Cottin [45] and Florenciano and Bruel [61]:  $h_{hot} = 498\ W\ m^{-1}\ K^{-1}$ ,  $h_{cold} = 582\ W\ m^{-1}\ K^{-1}$ ,  $h_{hole} = 1680\ W\ m^{-1}\ K^{-1}$ . Then, introducing the area of the geometrical surfaces of interest ( $\bar{s}_1 = 5,99\ 10^{-6}\ m^2$ ,  $\bar{s}_2 = 5,74\ 10^{-6}\ m^2$ ,  $s_h = 2,51\ 10^{-6}\ m^2$ ), one obtains a global value of  $R_{th} \approx 0.4$ .

The previous expression (Eq. 6.9) gives the global mean temperature (spatially averaged) of the wall but for more complex configurations where the heterogeneity of plate temperature is important for design, a local model for  $T_{wall}$  is mandatory.

To do so and considering an homogeneous solid medium, Eq. 6.7 can be written at a given axial position. Then using a 1D approximation in the context of an homogeneous multiperforated plate leads to:

$$T_{wall}(x) = \frac{T_{cold} + R_{th}(x)T_{ref\ hot}(x)}{1 + R_{th}(x)} \quad (6.10)$$

Considering that  $T_{ref\ hot}(x) = T_{ad\ hot}(x)$ , the adiabatic temperature from the adiabatic resolved computation,  $R_{th}(x)$  can be approximated as follow:

$$R_{th}(x) = \frac{T_{wall}(x) - T_{cold}}{T_{ad\ hot}(x) - T_{wall}(x)}. \quad (6.11)$$

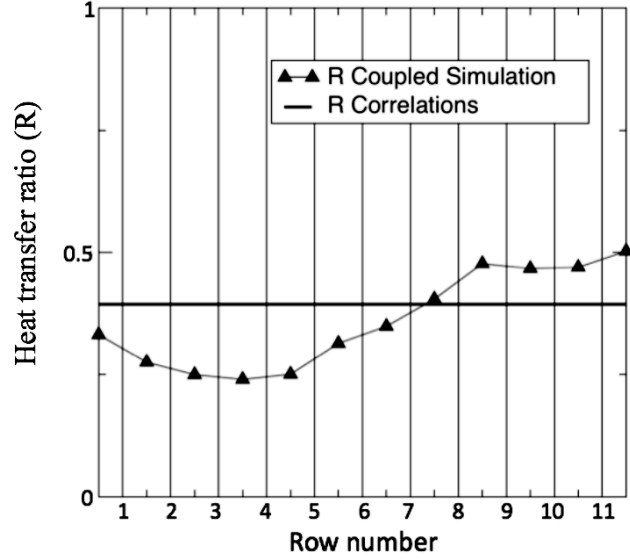


Figure 6.9: Ratio of heat transfer coefficients appearing in Eq. 6.9 estimated at each inter-row from the resolved coupled computation (▲) and from the correlations of Cottin [45] (—) recalled in Eqs. 2.10-2.14 .

Fig. 6.9 compares the evolution of  $R_{th}(x)$  along  $x$  evaluated at discrete positions (between two row of holes), with the global value of  $R_{th}$ . The mean value of  $R_{th}(x)$  is 0.36 which is close to  $R_{th}$ . Also this figure shows that whatever the position theses ratios are close, so  $R_{th}(x)$  can be approximated by the global ratio, and thus Eq.6.10 becomes:

$$T_{wall}(x) \approx \frac{T_{cold} + R_{th} T_{ref\ hot}(x)}{1 + R_{th}}, \quad (6.12)$$

The key point to determine  $T_{wall}$  is to define a reference temperature on the hot side of the plate ( $T_{ref\ hot}$ ). Cottin [45] suggested to take the temperature at the first computational node above the wall ( $T_{FN}$ ) as a surrogate of  $T_{ref\ hot}$ . However Berger *et al.* [23] and Lahbib [100] showed that this assumption is wrong when using the homogeneous model. Being the only affordable computations when dealing with industrial combustor, a specific work on the estimation of  $T_{ref\ hot}$  is mandatory.

## 6.5 Estimation of the adiabatic temperature of the boundary layer

An unresolved simulation of the Maveric plate, denoted "unresolved", where the effusion cooling is represented thanks to the adiabatic homogeneous model of Mendez and Nicoud [125] is performed. In this case, only the injection side is computed, the holes and the casing being represented by the boundary condition provided by the homogeneous model. The CPU cost, for each simulation is reported in table 6.6, taking the unresolved simulation as reference. Hole-resolved simulations require two orders of magnitude more CPU time than the simulation based on the homogeneous model for the perforated plate.

Simulation	Scaled CPU	Fluid cells mesh	Solid cells mesh	modeling
Resolved coupled	<b>200</b>	$5 \times 10^7$	$5 \times 10^6$	N/A
Resolved adiabatic	<b>100</b>	$5 \times 10^7$	N/A	N/A
Unresolved	<b>1</b>	$3 \times 10^6$	N/A	homogeneous

Table 6.6: Comparison of the scaled CPU costs.

The reference temperature on the hot side of the plate ( $T_{ref\ hot}$ ) results from the turbulent mixing between the hot cross flow ( $T_{hot}$ ) and the injected cold gas ( $T_{cold}$ ). The first node ( $T_{FN}$ ) leads to wrong result when the effusion cooling is modelled. Other possibilities to estimate  $T_{ref\ hot}$  have to be considered. A crude guess could be  $T_{ref\ hot} \approx T_{hot}$ , neglecting the near wall temperature decrease due to the cold gas injection. In this section, a more robust estimator of  $T_{ref\ hot}$  (denoted  $T_{mix}$ ) is proposed based on a local average over a relevant distance  $\delta$  in the normal direction to the perforated liner. Regarding the averaging procedure, three options were tested: spatial averaging (Eq. 6.13), velocity averaging (Eq. 6.14) and momentum averaging (Eq. 6.15).

$$T_{mix}^S(\delta) = \frac{\int_{\delta} \bar{T}(y) dy}{\delta}, \quad (6.13)$$

$$T_{mix}^V(\delta) = \frac{\int_{\delta} \bar{U}(y) \bar{T}(y) dy}{\int_{\delta} \bar{U}(y) dy}, \quad (6.14)$$

$$T_{mix}^M(\delta) = \frac{\int_{\delta} \bar{\rho}(y) \bar{U}(y) \bar{T}(y) dy}{\int_{\delta} \bar{\rho}(y) \bar{U}(y) dy}. \quad (6.15)$$

The corresponding non dimensional mixing temperatures,  $\theta_{mix}$ , may be defined as follows:

$$\theta_{mix} = \frac{T_{mix} - T_{cold}}{T_{hot} - T_{cold}}. \quad (6.16)$$

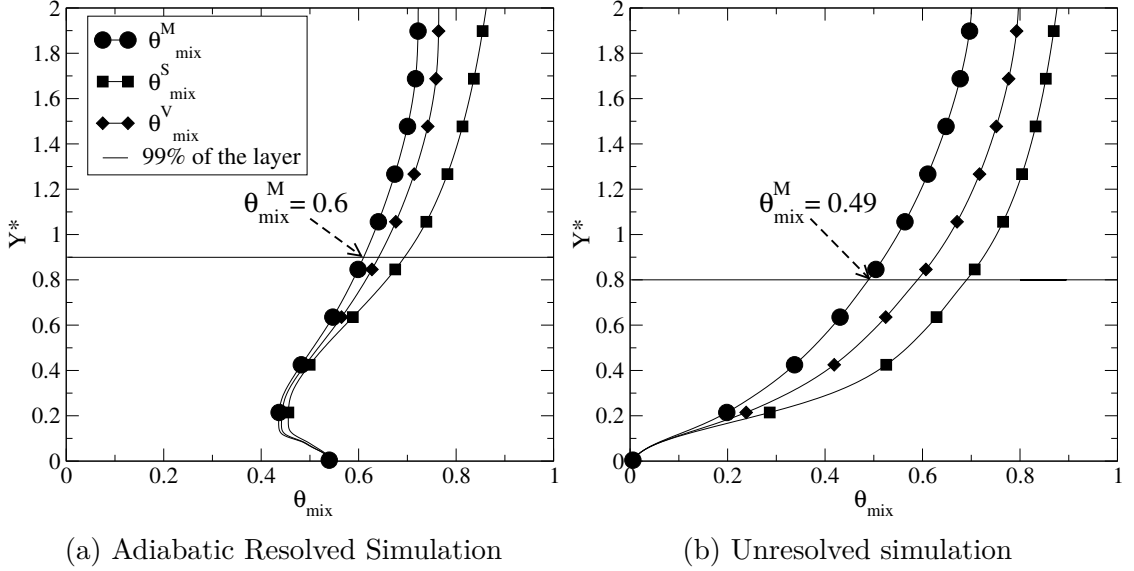


Figure 6.10: Evolution of the estimators defined in Eqs. 6.13, 6.14 and 6.15 scaled as in Eq. 6.16 with respect to the integration length  $\delta$  scaled by the inter-row distance  $\Delta$  for resolved (left) and unresolved (right) adiabatic simulations. Variables are space averaged in the spanwise direction. The horizontal line corresponds to the thermal boundary thickness  $\delta_{th}$ .

By post-processing the unresolved and the resolved adiabatic computations, profiles of the evolution of the non-dimensional mixing temperature with respect to the integration depth  $\delta$  are shown in Fig. 6.10 at the 9-10 inter-row position. The thermal boundary layer thickness,  $\delta_{th}$ , is taken as 99% of the non dimensional temperature. In the resolved case it is about 43% of the channel height and leads to  $Y^* = 0.9$  (horizontal line in Fig. 6.10a). In the unresolved case, it corresponds to  $Y^* = 0.8$ . Note that a variation of 10% on the integration length lead to a variation of 4% and 6% on resolved and unresolved case, respectively. From these results, in a simplification view, the integration length will be impose to  $Y^* = 0.9$  whatever the case.

On Fig. 6.11, results from the two simple reference temperature estimators ( $\theta_{hot}$  and  $\theta_{FN}$ ) and the three present estimators of the reference temperature ( $\theta_{mix}^M$ ,  $\theta_{mix}^V$ ,  $\theta_{mix}^S$ ) are compared for the two adiabatic cases. The integration depth is set to the thermal boundary layer thickness  $\delta_{th}$ . The results are scaled as follows:

$$\Theta_{mix} = \theta_{mix} / \theta_{ad\ hot}, \quad (6.17)$$

where  $\theta_{ad\ hot}$  corresponds to  $\theta_{FN}$  from the resolved adiabatic simulation. At

the beginning of the plate, all reference temperature estimators predict the same adiabatic plate temperature because  $\theta_{ref\ hot} = \theta_{hot}$ . However, reference temperature estimators are needed for unresolved simulations where the plate is modeled as a homogeneous boundary condition. In this case,  $\theta_{FN}$  does a poor job collapsing with the  $\theta_{cold}$  value. The momentum weighting  $\theta_{mix}^M$  gives the best values and trend for both cases. From now  $T_{mix}$  will denote  $T_{mix}^M(\delta_{th})$  which has been proved to be the best estimator of the reference temperature.

Since the proposed reference temperature estimator can be used on various effusion plates, it has been validated on another academical test case which has both different geometrical parameters and operating point. The result is presented on Appendix V.

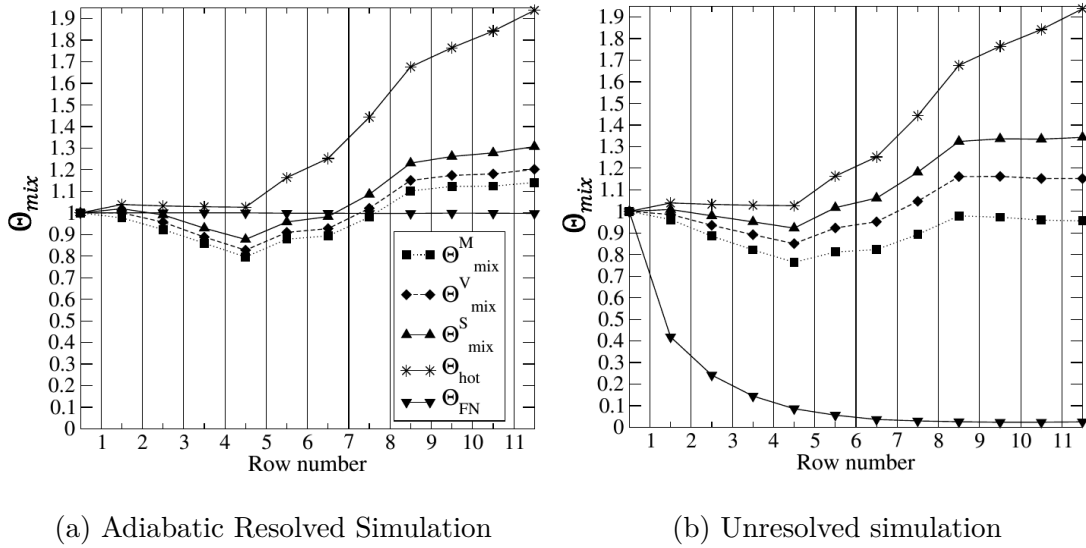


Figure 6.11: Comparison of different reference temperature estimators of  $\Theta_{ad\ hot}$ . The reference temperature estimators of Eqs. 6.13-6.15 are computed for  $\delta = \delta_{th}$  from the resolved (left) and unresolved (right) adiabatic simulations.

## 6.6 Comparison of heat transfer modelling strategies

Once  $R_{th}$  and  $T_{ref\ hot}$  have been assessed, Eq.6.12 can be used to compute  $T_{wall}^{model}$ , an estimator of the plate temperature. For a more practical comparison, a non dimensional estimation is computed as follows:

$$\theta_{wall}^{model} = \frac{T_{wall}^{model} - T_{cold}}{T_{hot} - T_{cold}}. \quad (6.18)$$

Different combinations have been tested as reported in Table 6.7. The performances of the different reference temperature estimators are displayed in Fig. 6.12 where they are compared to  $\theta_{wall}$ , the wall temperature computed from the resolved coupled simulation.  $\theta_{wall}^{model\ 1}$  to  $\theta_{wall}^{model\ 5}$  use  $R_{th}(x)$ , the heat transfer coefficient ratio calculated from the coupled computation which is variable in space and are thus expected to be more accurate. However, since the goal of the present study is to propose a low cost method for the industrial modeling routine, reference temperature estimators  $\theta_{wall}^{model\ 6}$  to  $\theta_{wall}^{model\ 10}$ , based on correlations for  $R_{th}$  with a global value are tested.

Name	Run type	$T_{ref\ hot}$ from	$R_{th}$ from
$\theta_{wall}$	Coupled resolved	/	/
$\theta_{wall}^{model\ 1}$	Uncoupled resolved	$T_{FN}$	$R_{th}(x)$ local from coupled simulations
$\theta_{wall}^{model\ 2}$	Uncoupled resolved	$T_{mix}$	
$\theta_{wall}^{model\ 3}$	Unresolved	$T_{FN}$	
$\theta_{wall}^{model\ 4}$	Unresolved	$T_{mix}$	
$\theta_{wall}^{model\ 5}$	No computation	$T_{hot}$	
$\theta_{wall}^{model\ 6}$	Uncoupled resolved	$T_{FN}$	$R_{th} = 0.4$ given by Correlations
$\theta_{wall}^{model\ 7}$	Uncoupled resolved	$T_{mix}$	
$\theta_{wall}^{model\ 8}$	Unresolved	$T_{FN}$	
$\theta_{wall}^{model\ 9}$	Unresolved	$T_{mix}$	
$\theta_{wall}^{model\ 10}$	No computation	$T_{hot}$	

Table 6.7: Tested combinations.

$\theta_{wall}^{model\ 1}$  computed with  $T_{FN}$  as a reference temperature on the resolved mesh and  $R_{th}(x)$  from the coupled simulation gives by construction the reference wall temperature. Note that the same reference temperature estimator on the unresolved case which requires the use of the homogeneous model [125] is far off the mark (see  $\theta_{wall}^{model\ 8}$  and  $\theta_{wall}^{model\ 3}$ ). When  $T_{hot}$  is used to model  $T_{ref\ hot}$ , the estimated wall temperature ( $\theta_{wall}^{model\ 5}$ ) is correct in the 5 first rows but difference with the reference value ( $\theta_{wall}$ ) increases downstream, once the film is established. Moreover, this reference temperature estimator combined with correlations ( $\theta_{wall}^{model\ 10}$ ) leads to an unacceptable overestimation of the wall temperature. The estimated wall temperature obtained when  $T_{mix}$  is used as a model for  $T_{ref\ hot}$  is in fair agreement with the reference wall temperature.  $\theta_{wall}^{model\ 2}$ ,  $\theta_{wall}^{model\ 4}$ ,  $\theta_{wall}^{model\ 7}$ ,  $\theta_{wall}^{model\ 9}$  show that the present reference temperature estimator,  $T_{mix}$ , is quite robust and can handle either resolved computations where holes are present or unresolved computations based on the homogeneous model of Mendez and Nicoud [125]. Among these reference temperature estimators, the most attractive for CPU cost reasons is  $\theta_{wall}^{model\ 9}$  which comes from an unresolved computation combined with correlations and produces a small error on the estimated wall temperature.

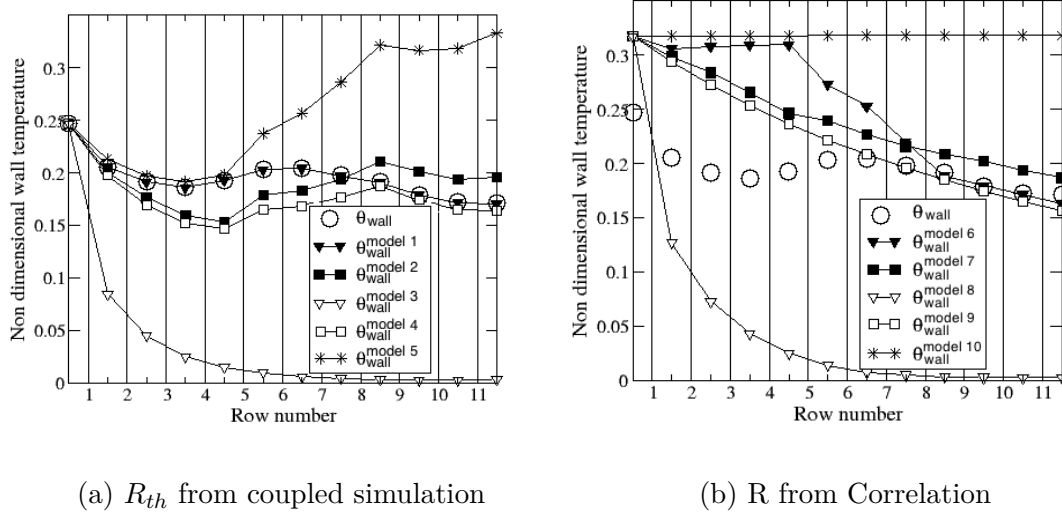


Figure 6.12: Wall temperature estimated from adiabatic simulations using heat transfer coefficient from coupled simulation (right) or from correlations (left).

## 6.7 A low-cost heat transfer modelling

Two resolved simulations of the flow around a multi-perforated plate were compared; a thermally coupled and an adiabatic one. From an aerodynamic point of view, the two simulations lead to very similar solutions. A global energy balance was computed to check quantitatively the accuracy of the numerical database as well as for identifying the main contributions to the phenomena controlling the temperature of the liner. The analysis showed that when the heat flux through the solid is marginal, which is the case for the usual engine operating conditions, it is possible to assess the wall temperature with both heat transfer coefficients from correlation and the aerodynamic field from an adiabatic computation. A robust estimator of the reference temperature  $T_{ref\ hot}$ , which gives fair result whatever the grid and modelling strategy, has been proposed. This estimator corresponds to an integral over the thermal mixing layer. Thanks to the use of a momentum averaging this estimator can be used on effusion cooling simulation modelled by homogeneous or heterogeneous methods as well as on hole resolved simulations. In other words, it allows independence from the grid and modelling strategy. Moreover, from a practical point of view, this quantity allows the direct comparison of RANS, LES, DNS simulations, either coupled or adiabatic. This method, named Adiab2colo, is affordable for industrial applications, unlike brute force resolved coupled simulations. In the present academic test case, the CPU cost was divided by about two hundred, disregarding the savings in terms of meshing time and setup time. The following chapter is an application to a helicopter combustor.

Chapter 7

**Application to a Safran's  
combustion chamber**

The method proposed in the last chapter, is now used by Safran's engineers to design and enhance their engines. An application of this unresolved adiabatic simulation of a real combustor is presented in the following chapter. Results are compared to experimental thermocolor paint provided by Safran Helicopter Engine (SHE).

**7.1 Application of the low-order model to a helicopter  
combustor . . . . . 109**

## 7.1 Application of the low-order model to a helicopter combustor

In this chapter, a turboshaft reverse flow combustion chamber, already presented in chapter 5.1, is considered (see Fig. 7.1). A reactive simulation with adiabatic walls, in which effusion cooling is accounted for thanks to the homogeneous model [125], has been performed with the LES solver AVBP. Such adiabatic simulation using modeled multiperforated plate is the standard in industry for predicting the combustor exit temperature profile or pollutant emissions. The objective of this section is to evaluate the low-order method, described in Section 6.4, for extracting the combustor liner temperature field from this computation. The  $\theta_{wall}^{model}$  estimator (see Table 6.7) was selected for this purpose.

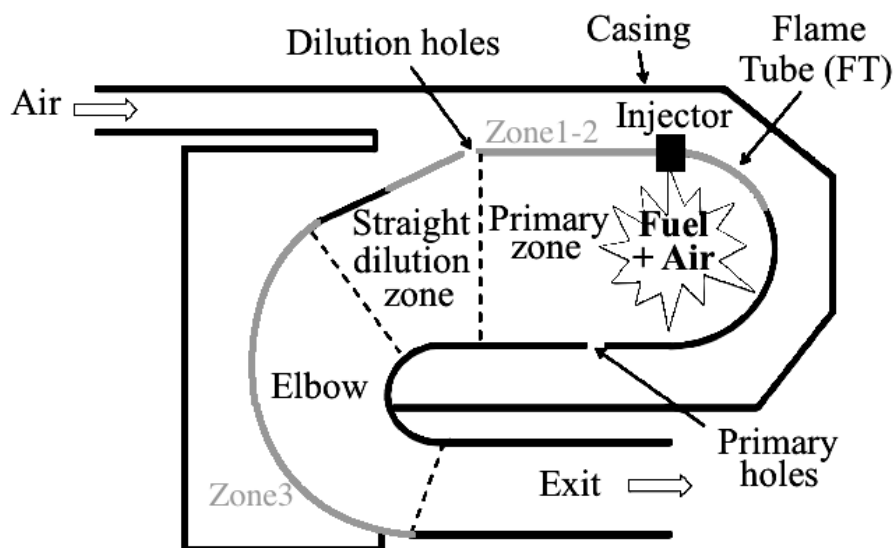


Figure 7.1: Schematic view of the combustor. Zones 1,2 and 3 are used in Fig.7.4 for comparison purposes. Zones 1 and 2 correspond to the external envelope of the flame tube at two azimuthal positions. Zone 3 corresponds to the external elbow.

The combustor simulation was averaged in time to obtain mean velocity and temperature fields within the flame tube and in the combustor casing (see Fig. 7.2). On the one hand, these fields were post-processed to compute locally the heat-transfer coefficients using the correlations from Cottin [45] on the cold side, within the holes and the one from Florenciano and Bruel [61] on the hot side. This led to a global value of the  $R_{th}$  coefficient, still local to each multiperforated patch since each patch is modeled by a homogeneous boundary condition. On the other hand, temperature and velocity fields were post-processed to estimate the corresponding adiabatic exchange temperature  $T_{mix}$  thanks to Eq. 6.15. The overall methodology is sketched Fig. 7.3.

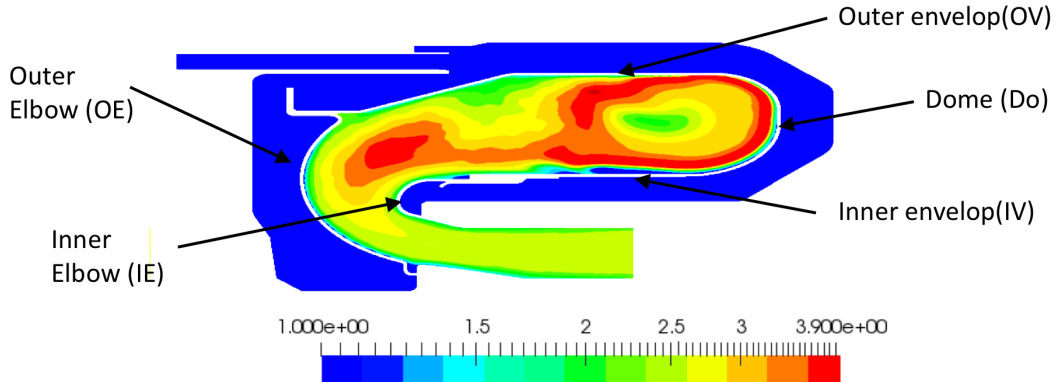


Figure 7.2: Non-dimensional mean fluid temperature field. Results from an adiabatic unresolved simulation using the homogeneous model. The name of each part is also given.

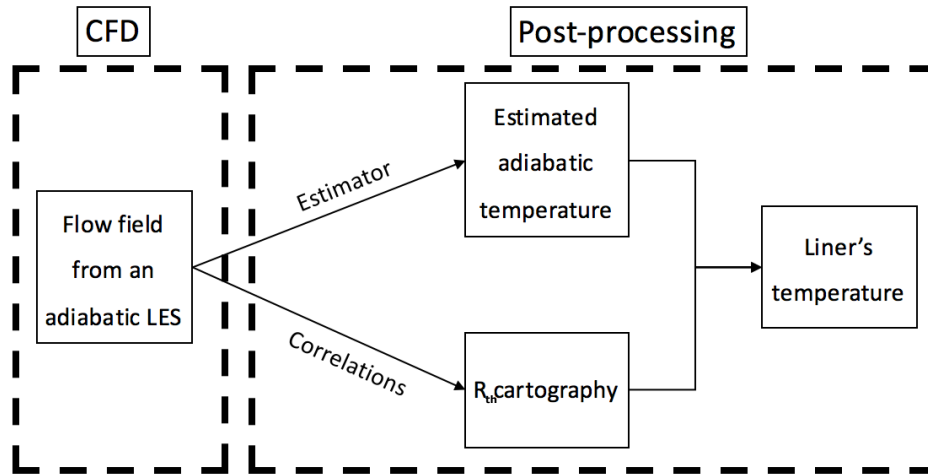


Figure 7.3: Block diagram of the whole proposed adiab2colo strategy.

The steady-state wall temperature field was then obtained thanks to Eq. 6.9. It should be noticed that transverse conduction within the liner is neglected in this approach, consistently with the findings of Berger *et al.* [24]. Figure 7.4 presents comparisons between the low-order temperature assessment and experimental data from thermo-color tests. Such tests are based on the use of thermo-sensitive paints, which color evolves depending on the wall temperature. The  $\theta_{wall}^{model}$  estimator leads to a fair prediction of the wall temperature levels. It also allows to localize the main hot and cold spots even if on both Zones 1 and 2, the hot part is not as wide as in

experiments. Indeed, in Zone 1, the B color spot on the left is well identified, like the very hot zone on the top of the picture. In Zone 2, the “D” temperature zone is also well retrieved. Finally, the homogeneous temperature field of Zone 3 is fairly reproduced.

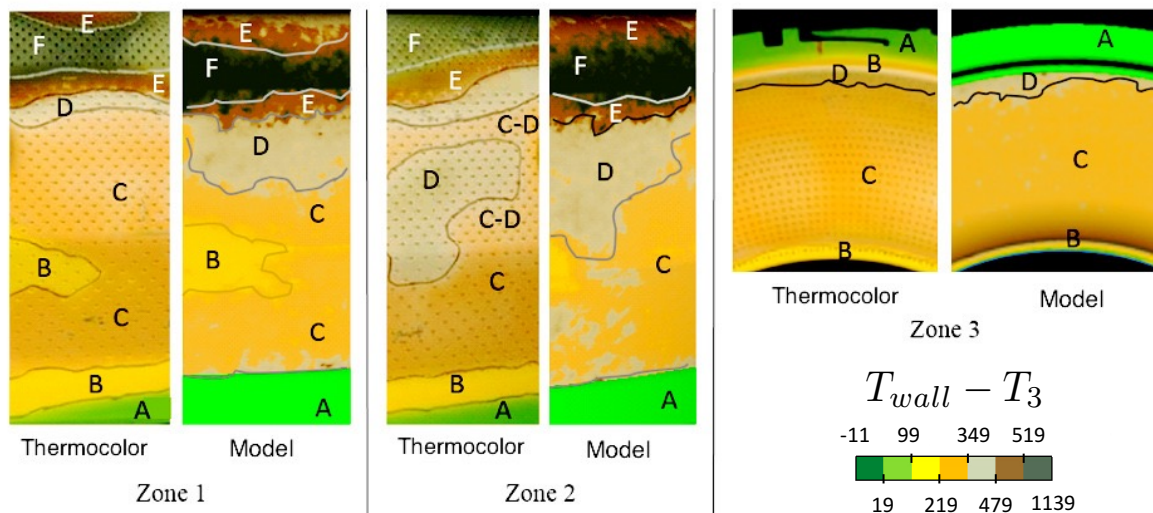


Figure 7.4: Comparison between temperature fields obtained from thermo-color tests and the low-order model with  $\theta_{wall}^{model}$  <sup>9</sup> reference temperature estimator on three regions characteristic of the combustor. Zones 1 and 2 correspond to the external envelope of the flame tube at two azimuthal positions. Zone 3 corresponds to the external elbow. See Fig. 7.1 for the location of zones 1-3.

The thermo-color technique gives access to the whole combustor liner temperature field topology but is characterized by a large range of uncertainties. Indeed, one color corresponds to a range of temperature and not to a given value. That is why more-detailed comparisons should take such uncertainties into account and focus on specific temperature profiles. Figure 7.6 shows a comparison between numerical and experimental data as a function of the axial position ( $x$ ) for two lines defined in Figure 7.5. The agreement is quantitatively very good on both lines when considering error bars from the tests. The temperature levels are correctly predicted from the outer-elbow (OE) to the combustor dome (Do).

An experimental method using thermocolor paint is usually used for the certification of an engine, but it is too costly and slow for the design stage. Numerical methods resolving inner hole’s flow and all the thermal exchange processes would be the best alternative but it is currently unreachable in terms of computational power. The present heat transfer modelling approach (adiab2colo) is giving a fast and cheap response to design variation. With this favorable trade-off between simplicity and accuracy, this methodology is now a classical method used by Safran

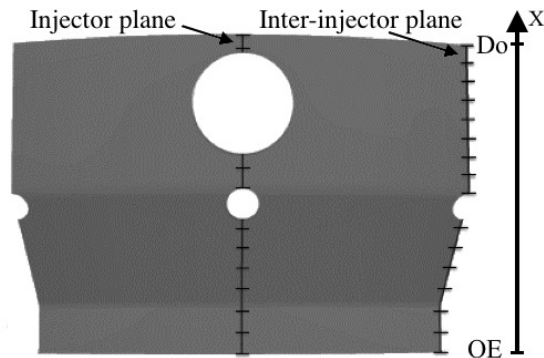


Figure 7.5: Definition of the injector plane and inter-injector plane lines on a 2D map extract from Fig. 7.2.

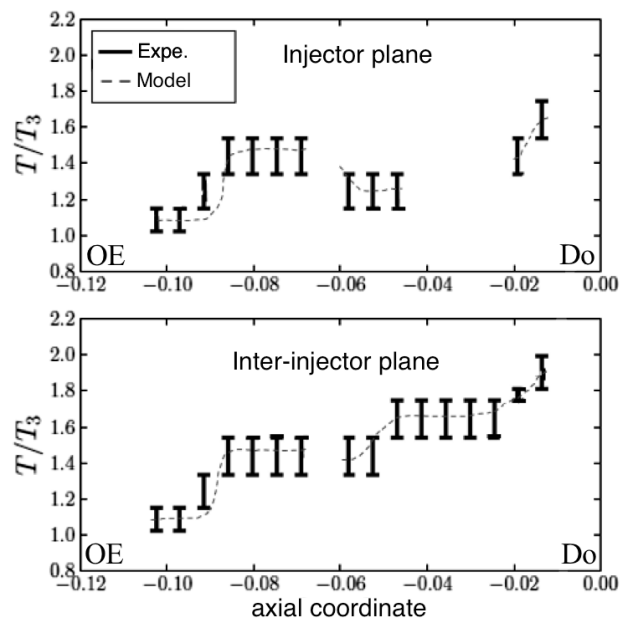


Figure 7.6: Comparison between experimental and predicted ( $\theta_{wall}^{model}$  estimator) temperatures on two lines along the engine axis (x) in the injector plane (top) and inter injector plane (bottom). Data is scaled by  $T_3$  which corresponds to the combustor inlet temperature.

Helicopter Engine during the design phases of their engines. Indeed, it is useful in the first design iterations to identify possible hot spots to be removed. Note however that radiation is not taken into account, and should smooth the temperature gradients as observed on Berger *et al.*[24] and Koren *et al.* [95].

## Part IV

# Toward high resolution LES of effusion cooling

## Chapter 8

# Mesh local refinement to enhance effusion cooling models

In this chapter, an adaptive mesh refinement criterion is suggested in order to enhance results of modelled effusion cooling while keeping reasonable simulation costs. Two adaptive criteria are proposed and their results on mesh and aerodynamic fields are compared to the initial results presented in chapter 4 on the Maveric test case. The two models can be used together as it is presented at the end of this chapter on a real combustor. These results will be presented during the international ETMM/ERCOFTAC conference in September 2018 [28]. Time averaged solutions on real combustor with the finest resolutions are not available yet but they soon will be thanks to a challenge allocated by CEA on TERA 1000-2. The end of chapter presents how the second criterion paved the way to hole resolved LES of an industrial combustor.

<b>8.1</b>	<b>Motivation</b>	<b>115</b>
<b>8.2</b>	<b>Aerodynamic prediction improvement: adaptive mesh refinement criterion</b>	<b>115</b>
8.2.1	The two criterion	115
8.2.2	Academical test case	116
8.2.3	Feasibility and CPU impact on a real combustor	119
<b>8.3</b>	<b>Relevance of the mesh adaption</b>	<b>122</b>
<b>8.4</b>	<b>An affordable LES including the meshing of effusion holes.</b>	<b>123</b>

## 8.1 Motivation

The thickened-hole model shares the properties of the homogeneous model when the grid is coarse. However, if the mesh cell size  $\Delta x$  is sufficiently fine at the wall, local effects can be captured. The  $R$  ratio defined in section 3.1 quantifies the mesh resolution with respect to the holes diameter:  $R = d/\Delta x$ . The thickened-hole model begins to show locally non-stationary phenomena with  $R$  values greater than unity ( $R = 4$ ) but much smaller than the resolution needed for a LES to correctly solve a jet-in-crossflow situation ( $R = 20 - 30$ ). However, the actual practice in gas turbine manufacturers like Safran Helicopter Engines is to perform LES of combustors with grids corresponding to  $R$  close to unity, making the result of the thickened-hole model [29] equivalent, but not significantly better than homogeneous model. To increase the  $R$  ratio, a finer mesh is needed, but out of reach *a priori*: going to a mesh at  $R = 4$  would increase the cost of an explicit simulation by at least a factor of 32.

The purpose of this chapter is to propose an alternative solution using adaptive mesh refinement in order to achieve better results with an affordable over-cost. Usual criteria, such as the second derivative of momentum (Habashi *et al.* [75]), require a fair description of the flow; a proper description of the mixing layers, for example. These elements are missing when dealing with flow features of the size of the mesh. New criteria, compatible with the early stages of a mesh adaptation, are therefore needed.

The two adaptive criteria, MLR1 and MLR2 (Mesh Local Refinement) are first described, then the academic test case is presented with particular attention to the mesh and properties resulting from each method. Finally, both methods are applied to an industrial case.

## 8.2 Aerodynamic prediction improvement: adaptive mesh refinement criterion

### 8.2.1 The two criterion

Hip ([www.cerfacs.fr/avbp7x/hip.php](http://www.cerfacs.fr/avbp7x/hip.php)) and MMG3D [52] libraries were used to adapt the mesh. For the MLR1 criteria, only the cells at a distance lower than 3 diameters of the hole were refined leading to a cell size divides by two in this area. The sensor is defined as:

$$\begin{aligned} dist_{axis}(i) \leq 3d, MLR1 &= 0.5 \\ dist_{axis}(i) > 3d, MLR1 &= 1 \end{aligned} \tag{8.1}$$

$i$  corresponds to the hole number and  $dist_{axis}$  the distance from its axis. This MLR1 criterium requires a priori exhaustive knowledge of each hole position with respect to the mesh frame. MLR1 is therefore a simple and robust way to refine but need a huge amount of case specific data. This data is not always available especially when dealing with hole-resolved CADs.

A second adaptation (MLR2), based on physical quantities can be proposed. The first aim of this MLR2 criterium is to refine effusion jets without geometrical knowledge, by focusing on their most prominent feature: a high velocity cold jet in a hot flow. The sensor is defined as follows:

$$\xi = \max \left( \min \left( \frac{\|u\| - U_{seuil}}{U_0 - U_{seuil}}, 1 \right), 0 \right) \times \max \left( \min \left( \frac{T_{hot} - T}{T_{hot} - T_{cold}}, 1 \right), 0 \right), \quad (8.2)$$

$U_{seuil}$  and  $U_0$  are case-dependent and are set to 20  $m/s$  and 100  $m/s$  respectively.  $T_{hot}$  and  $T_{cold}$  corresponds to the hot and cold temperature respectively. Then MLR2 can be recovered with the following formula:

$$MLR2 = 1 - 0.5 \xi. \quad (8.3)$$

The MLR2 criterion range is  $[0.5, 1]$ .

## 8.2.2 Academical test case

These methods are first evaluated on an academic test case, the Maveric plate studied in several papers [61, 131, 147, 30] and already presented in chapter 4.1.1. A hole resolved simulation where both sides of the multi-perforated plate are computed is considered as the reference. Extracting the mass flux from this simulation allows computing only the injection side in the simulations with the effusion cooling model. In chapter 4, it has been shown that the result is highly dependent on the  $R$  ratio. With  $R = 2$  jets from the aperture do not penetrate enough whereas with  $R = 4$  the results are very close to those obtained by the resolved simulation. In addition, jets and inter-rows profiles are distinct with  $R = 4$  which is not the case when  $R = 2$ . Going from  $R = 2$  to  $R = 4$  leads to a huge improvement on the result, in return to a much higher cost. A local mesh adaptation where only the key areas are refined would reduce the cost. Two uniform meshes corresponding to  $R = 2$  and  $R = 4$  and two adapted meshes MLR1 and MLR2 (named by the adaptive method used to obtain the corresponding mesh) are presented in Fig. 8.1. Both MLR1 and MLR2 meshes comes from the uniform mesh at  $R = 2$ . Since the MLR2 method needs temperature and velocity as input, the second adapted mesh (MLR2) is based on physical quantities from MLR1's solution. This doesn't influence the computational effort since only a short physical time is needed to assess the instantaneous field of

the effusion jets required for the process. Note that, in the MLR2 case, an additional coarsening is introduced as:

$$MLR2 > 0.90, MLR2 = 2 \quad (8.4)$$

This MLR2 strategy leads to a drastic reduction of the total number of nodes and thus reduces the over-cost. The main properties of the cases are presented in Table 8.1 where  $CPU_{adim}$  time is the cost to simulate a typical physical time of the configuration, taking the  $R = 2$  case as the reference.  $\sigma_n$  stands for the ratio between the real geometrical hole surface and its numerical counterpart. Note that on both adapted mesh, MLR1 and MLR2, no thickening is applied because in this zone  $R=4$ .

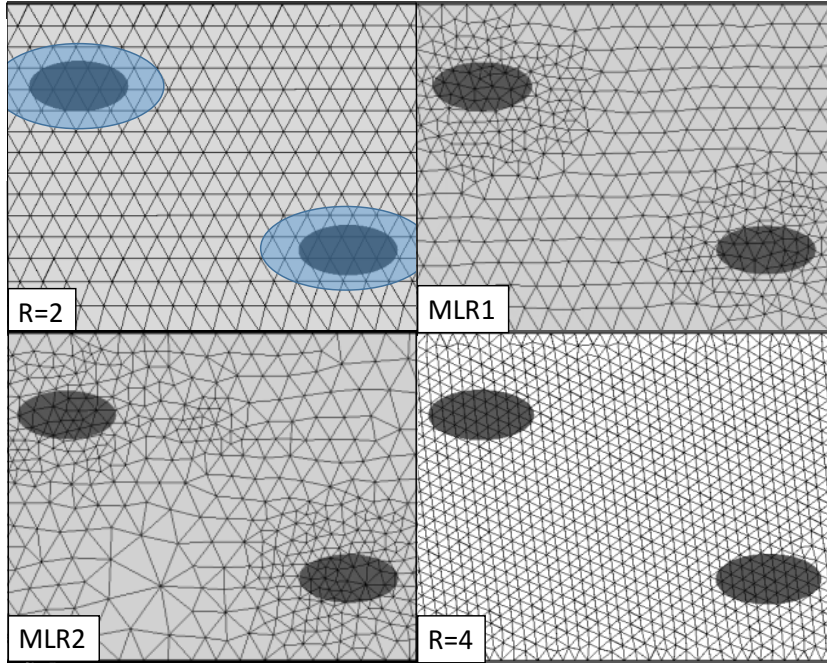


Figure 8.1: Superposition of real size multiperforation holes (black ellipse) on the wall for different grids ratio:  $R = 2$ ;  $R = 2$  with MLR1 adaptation;  $R = 2$  with MLR2 adaptation;  $R = 4$ . The enlarged holes are also highlighted on the  $R = 2$  case (light blue ellipse). No enlargement was used for the other cases since the mesh corresponds for  $R=4$  in these cases.

The results on the Maveric test case are presented in Fig 8.2. The  $R = 2$  field of temperature shows no fluctuation and mostly looks like a laminar flow. On the contrary, for the  $R = 4$  case, temperature variations are visible and small structures appear. When using either MLR1 or MLR2, results are quite similar and in both cases jets and inter jets areas can be distinguished. Wall temperature is also better

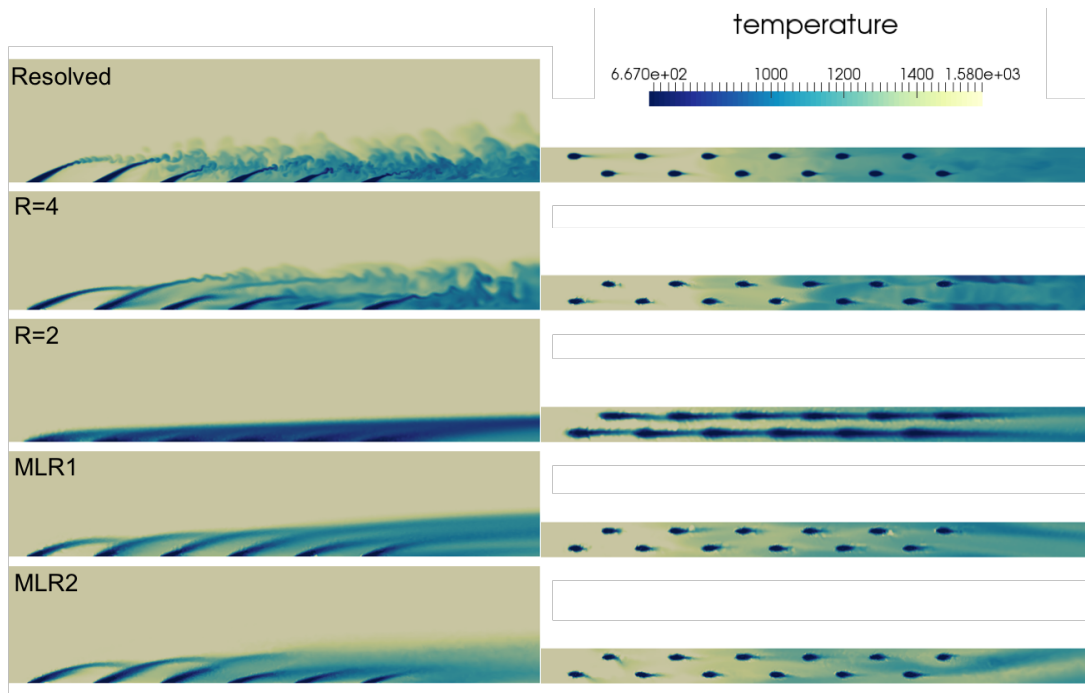


Figure 8.2: Instantaneous temperature fields through one row of holes (left) and on the wall (right) for each case.

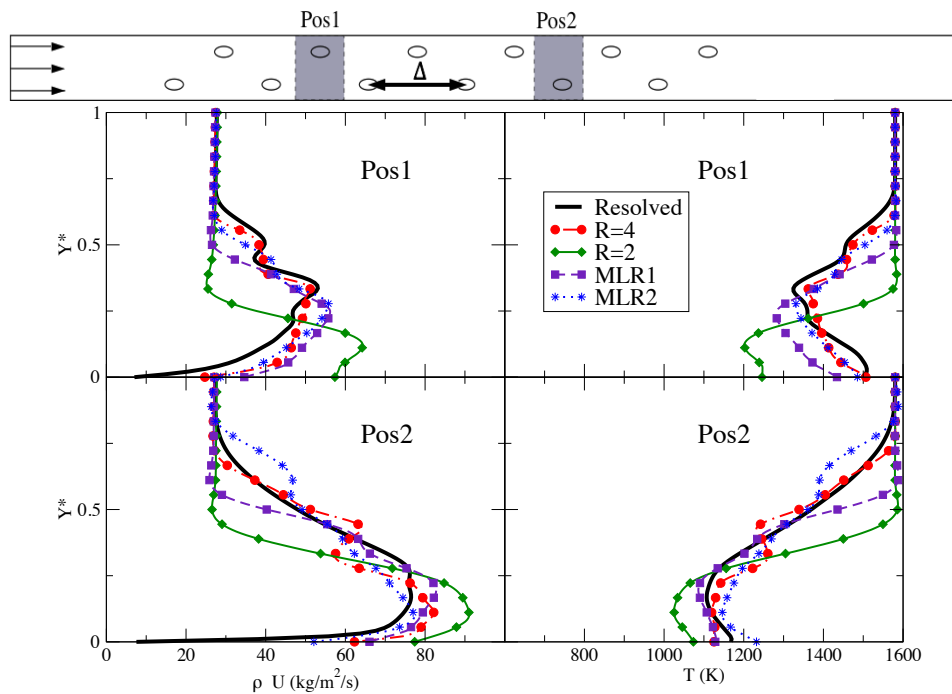


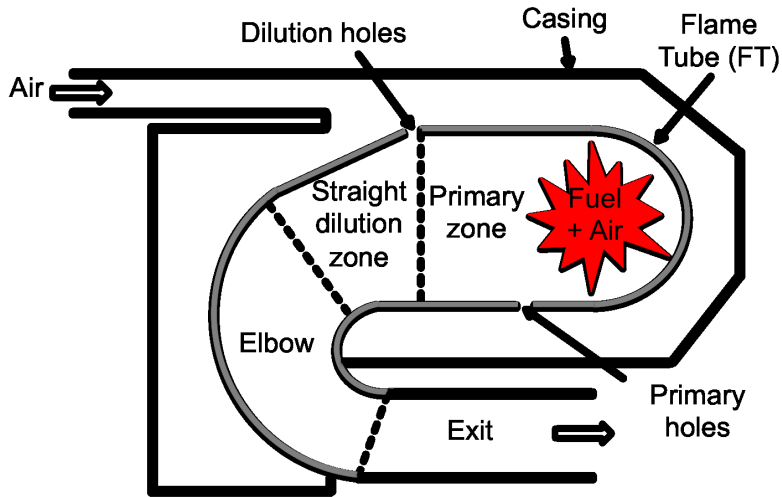
Figure 8.3: Streamwise mass flow-rate (left) and temperature (right) profiles are presented for 2 plate positions: Pos1 (upper part) and Pos2 (lower part).

Case	$R$ at the aperture	Cells	$\sigma_n$	$CPU_{adim}$
$R = 2$	2	858 459	0.48	1
MLR1	4	874 652	1	2.4
MLR2	4	405 343	1	1.2
$R = 4$	4	6 705 379	1	14.9
Resolved	16	51 077 506	1	510

Table 8.1: Characteristics of the meshes.

predicted than for the  $R=2$  case. In Fig. 8.3, temperature and axial mass flow-rate profiles are presented. 3D data is temporally and spatially averaged in the spanwise direction and presented as a function of  $Y^*$ , the distance from the plate normalised by the inter-row distance  $\Delta$  defined in Fig. 8.3 ( $\Delta = 11.68d$ ). Results are presented for 2 positions. The  $R = 2$  case does not recover the same shape as the reference solution and the jets penetrate 40% less than for the resolved case. In adapted cases results are closer (24% less for MLR1 and 8% more penetration for MLR2). In short, MLR2 provides results similar to  $R = 4$  for less than one tenth the price of the computation. It also outperforms  $R = 2$  for only 20% CPU cost increase.

### 8.2.3 Feasibility and CPU impact on a real combustor

Figure 8.4: Schematic view of the combustor extracted from Berger *et al.* [25].

These MLR methods have been applied to one sector of a turboshaft reverse flow combustion chamber (see Fig 8.4) already studied in [25, 30] and presented in chapter 5.1. The applied strategy is described in Fig. 8.5. Since the initial mesh ( $M_0$ ) comes with a very low  $R$  resolution a first MLR1 adaptation has been performed which lead to  $M_1$ . Note also that cells located on the wall and between

jets are coarsened. A second MLR1 has been performed in order to obtain  $M_2$ . Thanks to the results from  $M_2$ , a  $M_{2bis}$  mesh has been obtained using the so-called MLR2 method. A  $M_3$  has been created from the  $M_2$  mesh using MLR1 method in order to have a relative convergence comparison. Properties of different meshes are provided in Table 8.2.

Case	Refinement method	$R$ at the aperture	Cells	$\sigma_n$
$M_0$	N/A	0.75	45 892 340	0.06
$M_1$	MLR1 from $M_0$	2.25	54 417 508	0.56
$M_2$	MLR1 from $M_1$	4.5	115 523 143	1
$M_{2bis}$	MLR2 from $M_1$	4.5	72 484 864	1
$M_3$	MLR1 from $M_2$	6	242 437 477	1

Table 8.2: Characteristics of the meshes for the real combustor.

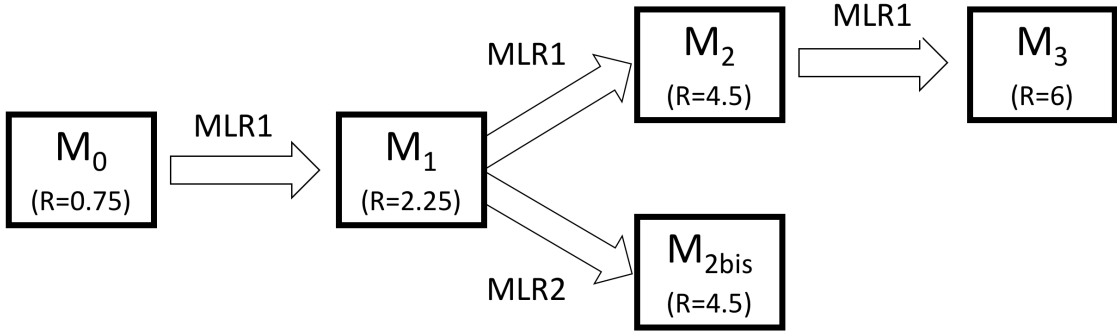


Figure 8.5: Description of the applied methodology.

Case	$CPU_{adim}$
$M_0$	1
$M_1$	2.8
$M_2$	14.6
$M_{2bis}$	4.0
$M_3$	31.1

Table 8.3: Characteristics of the CPU time for the real combustor.

On Fig. 8.6, a zoom on the wall of the combustor shows the evolution of the injected surface (dark grey) in function of the grid resolution. Thickening due to the modelling is visible on  $M_0$  and  $M_1$  while it is not the case for other cases. Note that the  $R$  ratio corresponds to the number of cells into the aperture's diameter (smaller diameter of the minor axis of the ellipse), however, since the grid is non-uniform, more cells can be counted.

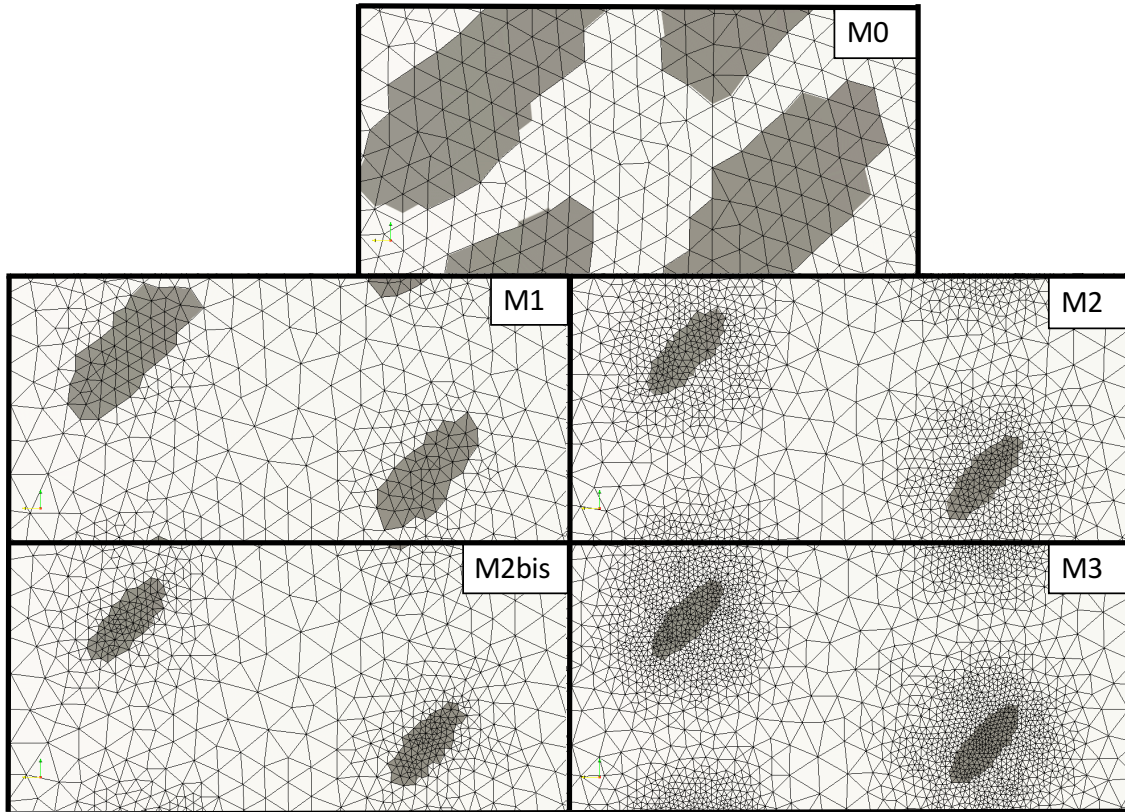


Figure 8.6: Boundary with the projection of the multiperforated holes with the thickened-hole model.

The  $CPU_{adim}$  corresponds to the CPU cost normalized by the CPU cost of the  $M_0$  case is given in Table 8.3. To give an idea, the cost of the  $M_0$  simulation is 40 000 CPU hours for 30ms of physical time. The  $M_2$  and the  $M_{2bis}$  have a very different CPU cost explained by the refinement method. With the MLR2 method, only key zones are refined and therefore the number of cells is much lower.

On Fig. 8.7, the inner mesh is visible, the temperature field from the corresponding instantaneous simulation is displayed. The aerodynamic field is very different, similar conclusion as on the Maveric test case can be drawn: on the  $M_0$  case, the cold layer is uniform while in the  $M_3$  case a jet is visible.  $M_2$  and  $M_{2bis}$  give very close results and allow to capture the jet induced by the effusion holes while in terms of CPU cost the  $M_{2bis}$  case is less expensive. In this case, only key zones of the jet are refined.

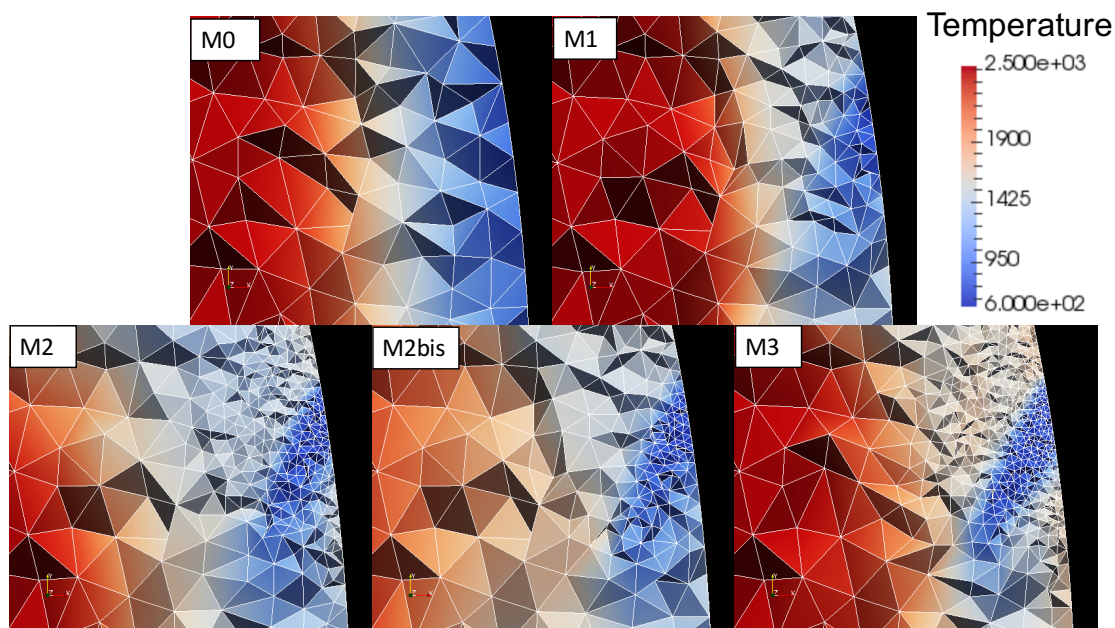


Figure 8.7: Cut through a hole. Visualization of the jet resulting from the corresponding instantaneous simulations.

### 8.3 Relevance of the mesh adaption

The present study shows how mesh adaptation combined with the thickened-hole model of effusion cooling can yield significant improvement of industrial Large Eddy Simulations (LES) for the design process of modern combustors. To our knowledge this is the first attempt of mesh adaptation focused specifically on modelling effusion cooling. The thickened-hole model can benefit from a higher mesh resolution, but the computational power available nowadays does not allow to achieve a significant breakthrough with usual meshing techniques. Indeed, the benefits given by the heterogeneity of the thickened-hole model need a wall  $R$  ratio larger than 4 while it is still lower than one in today meshes. With a brute force global refinement, such resolution will not be achieved before 10 years. Mesh adaptation allows to reach local wall  $R$  ratios of 4 while keeping meshes compatible with the present computational power. The present study shows on an academic test case how to define a refinement metric satisfying both a resolution requirement near the jets and a satisfactory mesh coarsening between holes. As a result, adapted meshes exhibits features similar to brute force meshes, yet for a much more affordable CPU over-cost. The same approach was also tested on a complex case with thousands of holes, with results significantly improved for both local effects and global trends.

The next step is to use the second adaptive method on a hole-resolved mesh to decrease the cost of the simulation.

## 8.4 An affordable LES including the meshing of effusion holes.

During the design process, engineers often need a high-precision simulation to give insight on a specific issue. In this view, hole-resolved computation are performed using RANS solvers, because unreachable in LES. However, the adaptive mesh criterion proposed in section 8 paves the way for such computations. LES on real geometries, including meshed holes has never been executed before and is a current axis of research. A major improvement would be the natural pressure coupling of each hole, allowing acoustic response from the liner. Also, such simulation could enable a direct thermal coupling without the uncertainties of correlations and mixing temperature estimator. Moreover, take into account this coupling would allow the pre-heating of the casing flow induced by conduction. This last phenomenon is totally neglected by adiabatic simulation.

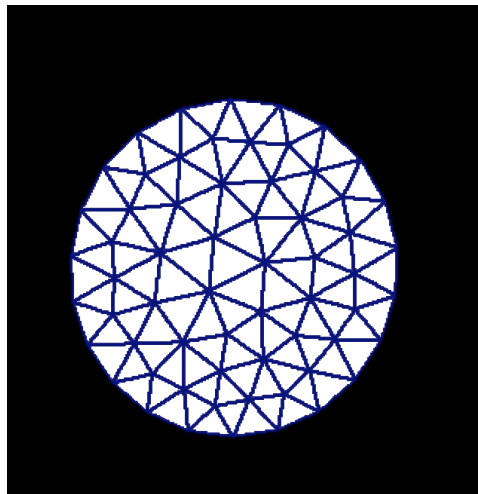


Figure 8.8: Mesh resolution inside the aperture on a hole-meshed real combustor.

The hole resolution on current hole-resolved meshes is presented on Fig.8.8 and shows about 7 cells in the hole diameter. With this mesh, Large Eddy simulations will not be able to solve the jets and it cannot be considered as a fully hole resolved case, only as a "hole meshed" case. Nevertheless it already contains about 500 million elements leading to a simulation at least 30 times more expensive than a modelled LES. However, the mesh being uniform, the resolution in some zones could be decreased. A mesh adaptation based on the MLR2 criterion is probably a good first step.

One should keep in mind that the flow repartition will be wrong in the first attempts, since LES cannot reproduce the correct pressure drop of an under-resolved diaphragm. As the main part of the fresh air is injected by effusion, this will dramatically alter the operating point. These meshes will probably need mesh adaptation focuses on pressure drop, such as Daviller *et al.* [50].

Note that this is a work in progress which is currently performed by the team from Safran helicopter Engine and CERFACS.

Chapter 9

**Combination between thickened-hole model and heat transfer method**

This chapter presents the combination of thickened hole model (instead of the homogeneous model) with the Adiab2colo methodology to predict the wall temperature. This evolution of the adiab2colo method, already used by Safran, is then applied to a typical helicopter engine. At the same time the benefit of the adaptive mesh refinement on the wall temperature prediction is given.

---

<b>9.1 Thermal prediction improvement</b>	<b>126</b>
9.1.1 Adiab2colo used with the thickened-hole model	126
9.1.2 Application on real combustor	127
9.1.3 Conclusion	129

---

## 9.1 Thermal prediction improvement

In part II and part III two independent models, thickened-hole and adiab2colo models, have been presented. The first one deals with the aerodynamic field and allows to model the effects of effusion cooling. The second one deals with the thermal field and allows to obtain the solid wall temperature. In part III, since the adiabatic aerodynamic field is required to feed adiab2colo, the homogeneous model has been used. However, the thickened-hole model, presented in part II, has been proven to give better results. Combining both methods is thus a natural idea.

### 9.1.1 Adiab2colo used with the thickened-hole model

As presented in Part III, the Adiab2colo model needs an adiabatic aerodynamic field. In chapter 7.1, the application of the model on a real combustor was presented using an aerothermal field from an unresolved numerical simulation using the homogeneous model for the effusion cooling but in fact, this field can come from any adiabatic computation (modelled or not). The same methodology can be used with an unresolved numerical simulation using the thickened-hole model, without any modification. However, in order to benefit from all the improvement brought by the thickened hole model such as the possible heterogeneity of the pattern, modifications have been added to the original Adiab2colo methodology.

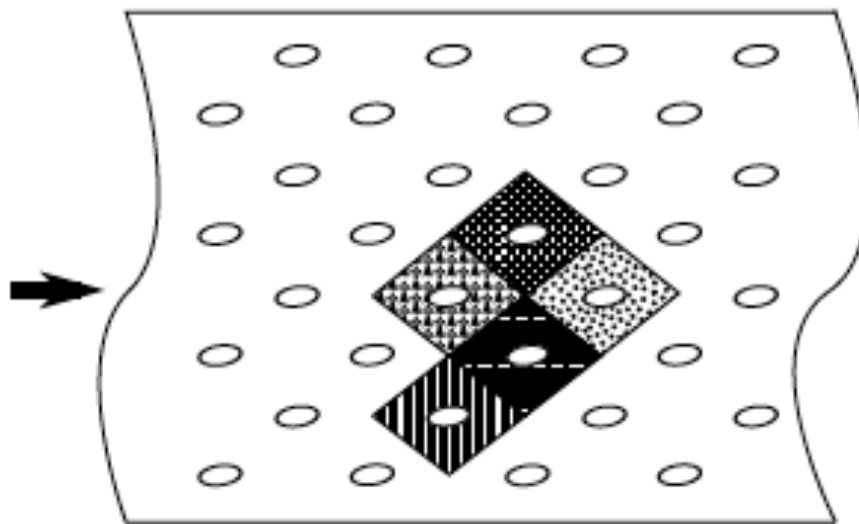


Figure 9.1: Representation of the diamond pattern. Figure extracted from the PhD of Arroyo [20]

The first step is to compute the surface of influence for each hole which cor-

responds to a diamond pattern as presented on Fig 9.1. Then each quantity is computed over it, instead of the whole effusion plate as presented on Part III. At the end, the averaging is more local because physical values are extracted over each hole, which gives a value of the heat transfer coefficients for each hole. Then the R ratio relevant to the  $i^{th}$  hole can be computed as follows.

$$R_{th,i} = \frac{h_{hot,i} \overline{s_{1,i}}}{h_{cold,i} \overline{s_{2,i}} + h_{hole,i}}. \quad (9.1)$$

Then instead of Eq. 6.12, the wall temperature equation becomes:

$$T_{wall}(x) = \frac{T_{cold} + R_{th,i} T_{ref\ hot}(x)}{1 + R_{th,i}} \quad (9.2)$$

### 9.1.2 Application on real combustor

The application of the improved Adiab2colo methodology is presented in the following section. At the same time, the improvement brought by the adaptive mesh refinement technic is presented.

#### Adiab2colo and mesh local refinement

In this section, the turboshaft reverse flow combustion chamber from Safran Helicopter Engine already presented in chapters 5.1, 7.1 and 8.2 and published in [25, 28, 30] has been chosen to test the applicability of the new Adiab2colo method on complex geometries. At the same time, the improvement brought by local mesh refinement on the wall temperature prediction is validated.

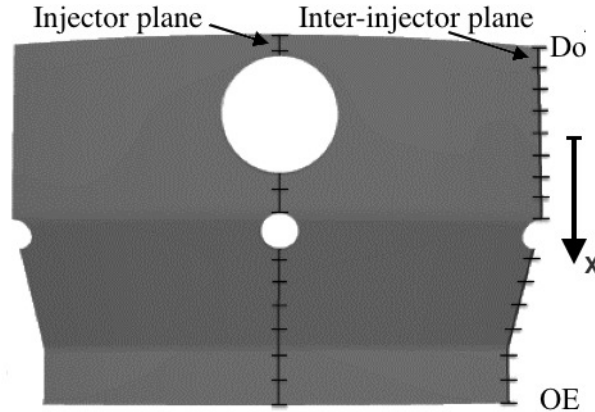
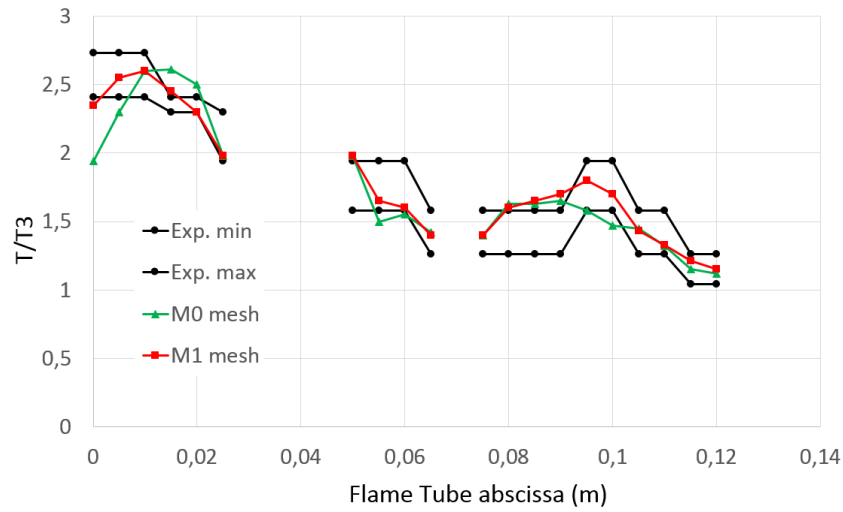
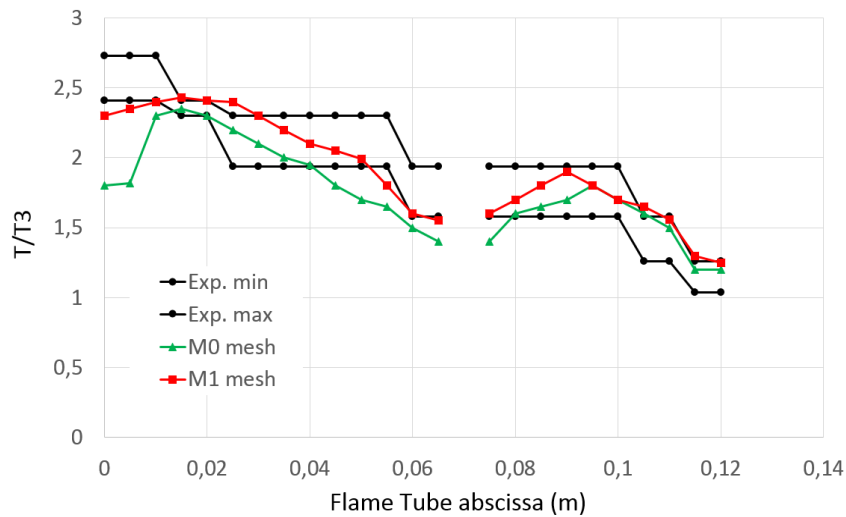


Figure 9.2: Definition of the injector plane and inter-injector plane lines.



(a) Injector plane.



(b) inter injector plane

Figure 9.3: Comparison between experimental thermocolor measurements and results from  $M_0$  and  $M_1$ .

Temperature of the liner is compared to experimental measurements in Fig. 9.3. However a large computational time is required to assess time averaged solution and thus only the  $M_0$  and the  $M_1$  cases are available so far (see Table 8.2). The provided experimental data comes from thermocolor tests as described in [25, 30]. This explains the broad range of experimental data at a given location. Thermocolor indeed give only access to a temperature range, but has the advantage of allowing to

characterize the whole combustor temperature field. Since the computation is adiabatic, the simulations are averaged in time to obtain mean velocity and temperature fields and are then post processed using the "Adiab2colo" methodology presented in chapter 6.

Figure 9.3 shows a comparison between numerical and experimental data as a function of the axial position ( $x$ ) for two lines defined in Fig. 9.2. Both numerical simulations are very close to the experimental results. However the  $M_1$  simulation gives closer results. It highlights the fact that the thickened-hole model combined with an adaptive mesh refinement methods increases the efficiency of the wall temperature prediction for aeronautical combustors. In particular, the hot zone close to the combustor dome (low flame tube abscissa, noted Do on Fig. 9.2) is better captured by mesh  $M_1$ . In the same way, temperature levels in the range of abscissa [0.04-0.08] is in better agreement with experiments for this mesh. In addition, the temperature level is higher and better predicted with adapted mesh than with the standard mesh ( $M_0$ ), demonstrating that a less coherent cooling film is directly resolved, as shown on the academic case.

### 9.1.3 Conclusion

Combination of an improved aerodynamic model, the thickened-hole model, with the `adiab2colo` methodology developed during this thesis and described in Part III has been tested on a complex industrial burner. The  $M_0$  simulation presented just before is the classical resolution and precision currently reached by Safran. In this section, the wall temperature prediction enhancement that can be expected in the incoming years thanks to the increasing computational power has been presented. However, using a classical homogeneous mesh, regarding the computational power evolution, the wall prediction would be sticking to such result for 10 years. In that sense, when combined with the adaptive mesh refinement method proposed during this thesis, the updated method allows to reach better results within a few years ( $M_1$  already accessible today).

## Part V

# Final conclusions and perspectives

## Conclusion and perspectives

The effusion technology pattern is crucial in the design of a motor, however, according to the current computational power and the complexity of a real engine no model allow to take into account the effusion cooling in a simulation of a full engine. Manufacturers are therefore unable to accurately optimize it. The work performed during this thesis allowed to improve both design and validation phases.

The design phases, where many combustor variations are tested, requires for each simulation a very short time of response. During this thesis, a low-cost method which takes into account the heterogeneous perforation pattern has been proposed. This method relies on two numerical sub-models, an aerodynamic one called thickened-holes model [29, 27] and a thermal one [30, 31]. These two models have been used by Safran Helicopter Engine on various engines and are now part of the design chain. To go further and enhance this methodology, a local mesh refinement strategy was also developed [28].

Developments relevant to the final validation phase were also done within the framework of this thesis. Experimental tests are used for a long time but do not give access to the full information and validation. That is why hole resolved RANS simulations are also performed by the engine manufacturers. On this configuration, where holes are meshed, a LES is not reachable but would give more information on the unsteadiness. During this thesis a work on the mesh has been proposed allowing to reduce the cost of such LES making it reachable with the current computational power.

The aerodynamic model proposed during this thesis is not limited to combustor liners. The thickened-hole model [29, 27] can be applied for cooling holes on turbine blades (see Harnieh *et al.* [79]). In this case, results are encouraging and permits both an important CPU time saving and a design process enhancement since many hole layouts can be easily tested using a single mesh of the blade.

Perspectives have been risen during this PhD thesis. The first one is the extension of the thickened hole model so that the flowrate through each aperture is deduced from the pressure drop across the liner instead of being imposed *a priori* by the user. The second one is the study of the radiations. A work on its effect has

---

to be performed in order to take into account its contribution. In that case, a radiative solver could be added and the work of Berger (a 3CR simulation: combined combustion, conduction, radiation) could be (re)performed using the thickened-hole model and the estimator of the adiabatic temperature.

The work achieved during this PhD thesis has been promoted thanks to 6 external communications: 2 journal [29, 30], 2 national conferences [31, 27], 1 international conference [28], and an in-collaboration international conference [79].

# Appendices

## Pertinence of the Mendez and Nicoud momentum correction on high resolution

In 2015, D. Taieb (from CORIA) performed a first heterogeneous simulation on an effusion plate, without momentum correction. In the thickened-hole model the momentum compensation of Mendez and Nicoud vanished with the hole resolution. A legitimate question is: do we need momentum compensation on 2018 meshes ?

On Figs. 4 5 6, the same post processing as in chapter 4 has been performed. Two additional computations have been made in order to check the influence of the Mendez's assumption. The Mendez's assumption consists in a modification of the injection angle in order to keep the same streamwise momentum flux between modelled simulation and real one. This is achieved thanks to an application of the porosity factor on the normal velocity solely. (See Eqs. 2.5 and 2.5). The blue diamond curve is different from the thickened-hole model's curve (Dashed black dotted curve) when  $R = 2$  while it is close when  $R = 4$ . This highlights the importance of Mendez's model when the resolution is low whereas it becomes useless when  $R$  is high. Indeed, when  $R = 2$ , the thickened-hole model gives better results.

One should not attempt a hole imprinting method in LES without momentum correction, unless  $R > 4$ .

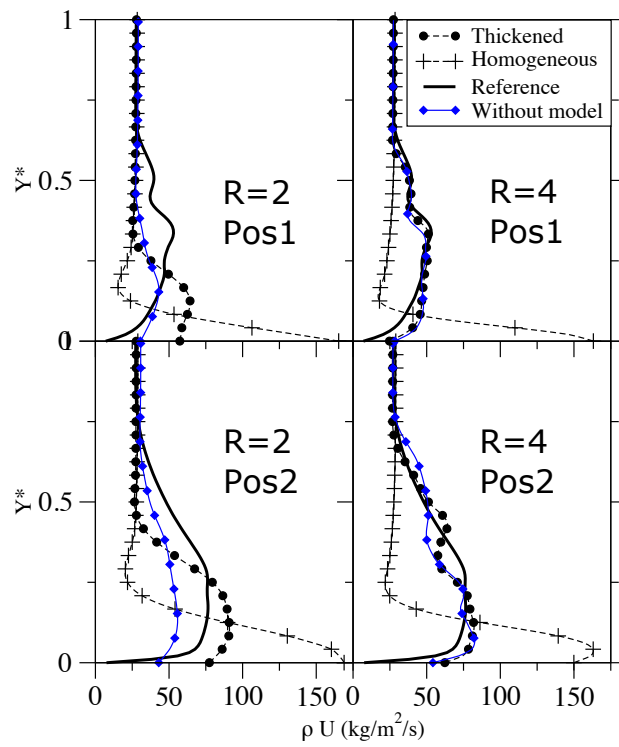


Figure 4: Spatially and temporally averaged streamwise momentum  $\rho U$  at positions Pos1 (top) and Pos2 (bottom), for ratios R=2 and R=4 (from left to right) already presented in Fig. 4.8. "Without model" corresponds to the result from a thickened computation without Mendez's model.

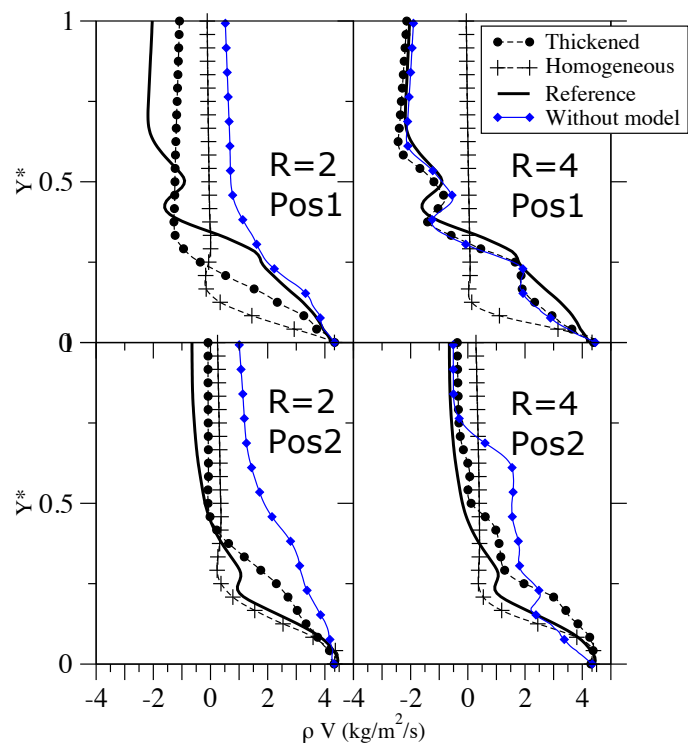


Figure 5: Spatially and temporally averaged normal momentum  $\rho V$  at positions Pos1 (top) and Pos2 (bottom), for ratios R=2 and R=4 (from left to right) already presented in Fig. 8.2. "Without model" corresponds to the result from a thickened computation without Mendez's model.

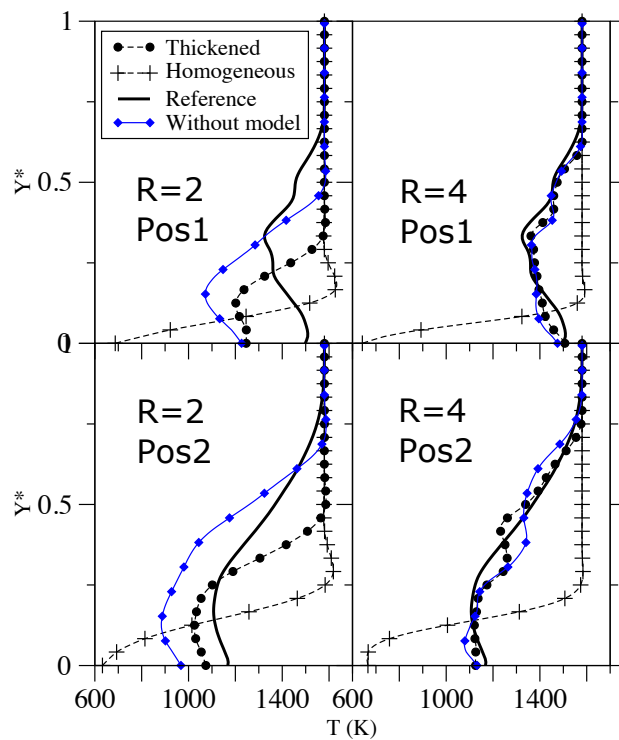


Figure 6: Spatially and temporally averaged temperature profiles  $T$  at positions Pos1 (top) and Pos2 (bottom), for ratios  $R=2$  and  $R=4$  (from left to right) already presented in Fig. 4.10. "Without model" corresponds to the result from a thickened computation without Mendez's model.

## Validation of the reference temperature estimator on an academic configuration

In the process of publication, a reviewer asked to test the temperature estimator on an other academic case. In this section the reference temperature estimator has been applied on the KIAI (Knowledge for Ignition, Acoustics and Instabilities) setup developed during the 7th Framework Programme of an EU funded Research Project (see Fig. 7). This configuration has been studied and detailed in [122, 9, 10, 18]. For the present study, the Blowing and Density ratio used are  $M = 3$  and  $D_R = 1$  respectively. The geometry denoted G2 in [122, 9, 10, 18] has been retained. Geometrical characteristics are given in the table 1.

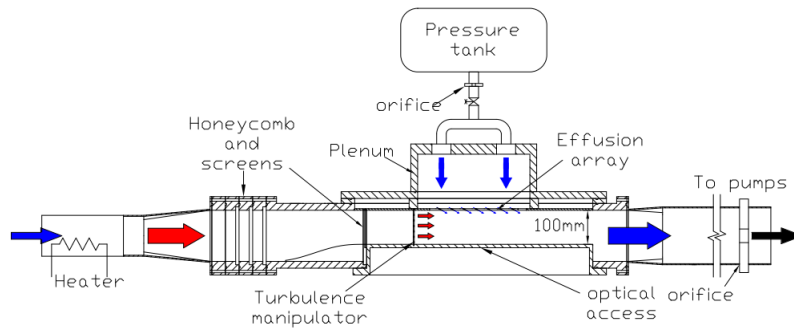


Figure 7: KIAI experimental setup.

Diameter (d)	Number of rows	L/d	$\alpha$	$\Delta x$	$\Delta z$	$\sigma$
1.50	18	6.25	30	9.15	7.37	2.32

Table 1: Geometry of the plate of interest.

Since the flow is considered fully turbulent, a turbulent profile was imposed at the inlet, however no turbulence fluctuations were added. The multiperforated

plate was modelled using the homogeneous model [125] (note that the porosity is calculated considering the effusion angle which leads to a value of  $\sigma = 2.32$ .) The adiabatic efficiency is presented on Figure 8. On this Figure, the experimental, the first node, the adiabatic estimated temperature and the result from Mazzei [122] are presented. For the adiabatic estimator of the temperature, the integration high was taken as 99% of the thermal thickness on the last hole position, which has been extracted from the simulation. The same conclusion as previous has been obtained. The temperature directly extracted using the first node method failed to assess the adiabatic efficiency. On the contrary the reference temperature from the  $T_{mix}$  predicts the correct trends even if the adiabatic efficiency is overpredicted for the last rows.

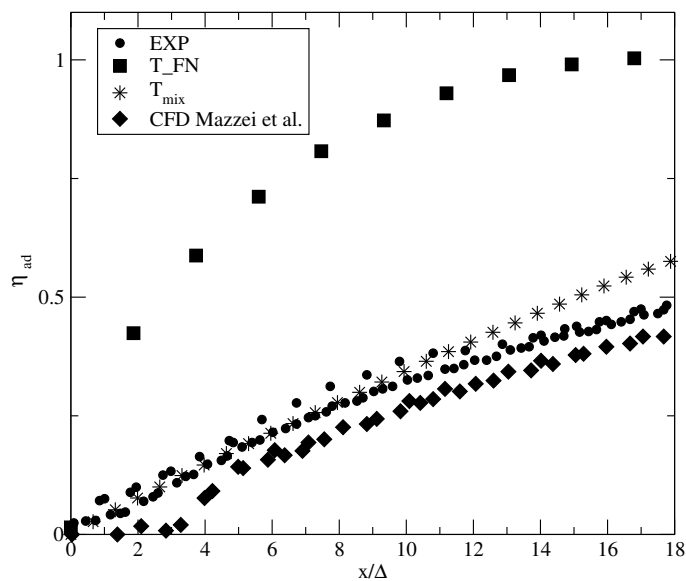


Figure 8: Results in terms of adiabatic efficiency. Experimental and hole resolved CFD results are extracted from Mazzei *et al.* [122].  $T_{FN}$  and  $T_{mix}$  corresponds to the adiabatic wall temperature computed from the present simulation using First Node or estimator method respectively.



## Bibliography

- [1] *FLUENT, ANSYS. 17.0 udf manual. ANSYS Inc., 2016.* *Cité page 43*
- [2] Gyrotory combustion chamber from SHE awarded by safran group. *Cité page 17*
- [3] Integrated hybrid rans/les of a realistic gas turbine engine (<https://ctr.stanford.edu/integrated-hybrid-ransles-realistic-gas-turbine-engine-0>). *Cité page 5*
- [4] A. T. A. Piacentini, T. Morel and F. Duchaine. Open-palm: an open source dynamic parallel coupler. In *In IV International Conference on Computational Methods for Coupled Problems in Science and Engineering*, 2011. *Cité page 91*
- [5] P. Aillaud, F. Duchaine, L. Gicquel, and S. Didorally. Secondary peak in the nusselt number distribution of impinging jet flows: A phenomenological analysis. *Physics of Fluids*, 28(9):095110–1– 095110–22, 2016. *Cité page 7*
- [6] P. Aillaud, F. Duchaine, L. Gicquel, and S. Didorally. Characterization of the surface curvature effect using les for a single round impinging jet. In *Proceedings of ASME Turbo Expo 2017: Turbine Technical Conference and Exposition*, pages GT2017–64159, Charlotte, NC, USA, 2017. *Cité page 7*
- [7] J. Amaya, E. Collado, B. Cuenot, and T. Poinso. Coupling les, radiation and structure in gas turbine simulations. In N. A. U. Center for Turbulence Research, editor, *Proc. of the Summer Program* , volume in press, 2010. *Cité page 91*
- [8] H. D. Ammari, N. Hay, and D. Lampard. The effect of density ratio on the heat transfer coefficient from a film-cooled flat plate. *J. Turbomach.* , 112:444–450, 1990. *Cité page 18*
- [9] L. Andrei, A. Andreini, C. Bianchini, G. Caciolli, B. Facchini, L. Mazzei, A. Picchi, and F. Turrini. Effusion cooling plates for combustor liners: ex-

- perimental and numerical investigations on the effect of density ratio. *Energy Procedia*, 45:1402–1411, 2014. Cité page 138
- [10] L. Andrei, A. Andreini, C. Bianchini, B. Facchini, and L. Mazzei. Numerical analysis of effusion plates for combustor liners cooling with varying density ratio. In *ASME Turbo Expo 2013: Turbine Technical Conference and Exposition*, pages V03CT17A007–V03CT17A007. American Society of Mechanical Engineers, 2013. 2 citations pages 20 et 138
- [11] L. Andrei, L. Innocenti, A. Andreini, B. Facchini, and L. Winchler. Film cooling modeling for gas turbine nozzles and blades: Validation and application. *Journal of Turbomachinery*, 139(1):011004, 2017. 2 citations pages 32 et 33
- [12] A. Andreini, R. Becchi, B. Facchini, A. Picchi, and A. Peschiulli. The effect of effusion holes inclination angle on the adiabatic film cooling effectiveness in a three-sector gas turbine combustor rig with a realistic swirling flow. *International Journal of Thermal Sciences*, 121:75–88, 2017. Cité page 20
- [13] A. Andreini, G. Caciolli, B. Facchini, L. Tarchi, D. Coutandin, A. Peschiulli, and S. Taddei. Density ratio effects on the cooling performances of a combustor liner cooled by a combined slot/effusion system. In *ASME Turbo Expo 2012: Turbine Technical Conference and Exposition*, pages 903–914. American Society of Mechanical Engineers, 2012. Cité page 20
- [14] A. Andreini, J. L. Champion, B. Facchini, E. Mercier, and M. Surace. Advanced liner cooling numerical analysis for low emission combustors. In *25TH International Congress Of The Aeronautical Sciences*, 2006. 2 citations pages 20 et 41
- [15] A. Andreini, R. Da Soghe, B. Facchini, and L. Mazzei. Local source based CFD modeling of effusion cooling holes : validation and application to an actual combustor test case. *Proceedings of GT2013*, 2013. 2 citations pages 32 et 33
- [16] A. Andreini, R. Da Soghe, B. Facchini, L. Mazzei, S. Colantuoni, and F. Turrini. Local source based cfd modeling of effusion cooling holes: Validation and application to an actual combustor test case. *Journal of Engineering for Gas Turbines and Power*, 136(1):011506, 2014. Cité page 41
- [17] A. Andreini, B. Facchini, L. Mazzei, L. Bellocci, and F. Turrini. Assessment of aero-thermal design methodology for effusion cooled lean burn annular combustors. In *ASME Turbo Expo 2014: Turbine Technical Conference and Exposition*, pages V05CT18A012–V05CT18A012. American Society of Mechanical Engineers, 2014. 2 citations pages 41 et 42
- [18] A. Andreini, B. Facchini, A. Picchi, L. Tarchi, and F. Turrini. Experimental and theoretical investigation of thermal effectiveness in multiperforated plates for combustor liner effusion cooling. *Journal of Turbomachinery*, 136(9):091003, 2014. 2 citations pages 20 et 138

- 
- [19] J. Andreopoulos and W. Rodi. Experimental investigation of jets in a cross-flow. *J. Fluid Mech.*, 138:93–127, 1984. *Cité page 27*
- [20] G. Arroyo-Callejo. *Modélisation thermique avancée d’une paroi multiperforée de chambre de combustion aéronautique avec dilution giratoire*. PhD thesis, INSTITUT SUPERIEUR DE L’AERONAUTIQUE ET DE L’ESPACE (ISAE), 2016. *3 citations pages 16, 22, et 126*
- [21] G. Arroyo-Callejo, E. Laroche, P. Millan, F. Leglaye, and F. Chedeveigne. Numerical investigation of compound angle effusion cooling using differential reynolds stress model and zonal detached eddy simulation approaches. *Journal of Turbomachinery*, 138(10):101001, 2016. *Cité page 16*
- [22] T. auf dem Kampe and S. Volker. A model for cylindrical hole film cooling: Part ii—model formulation, implementation and results. In *ASME Turbo Expo 2010: Power for Land, Sea, and Air*, pages 1551–1560. American Society of Mechanical Engineers, 2010. *2 citations pages 32 et 33*
- [23] S. Berger. *Implementation of a coupled computational chain to the combustion chamber’s heat transfer*. Phd thesis, Université de Toulouse, INPT, 6 2016. *Cité page 102*
- [24] S. Berger, S. Richard, F. Duchaine, G. Staffelbach, and L. Gicquel. On the sensitivity of a helicopter combustor wall temperature to convective and radiative thermal loads. *Applied Thermal Engineering*, 103:1450–1459, 2016. *6 citations pages 42, 43, 82, 93, 110, et 112*
- [25] S. Berger, S. Richard, S. G., F. Duchaine, and L. Gicquel. Aerothermal prediction of an aeronautical combustion chamber based on the coupling of large eddy simulation, solid conduction and radiation solvers. GT2015-42457, June 2015. *4 citations pages 43, 119, 127, et 128*
- [26] R. Bizzari and A. Dauplain. Simulation aux grandes échelles du blocage dans un moteur à détonation tournante. working note, ENSEEIHT - CERFACS Toulouse, France, September 2015. *Cité page 3*
- [27] R. Bizzari, A. Dauplain, L. Gicquel, and F. Nicoud. A thickened-hole model for les over multiperforated liners. In *4e Colloque du réseau d’INitiative en Combustion Avancée (INCA)*, Palaiseau, France, October 2017. SAFRAN TECH. *3 citations pages 46, 131, et 132*
- [28] R. Bizzari, M. Ferand, A. Dauplain, G. Staffelbach, S. Richard, J.-D. Mueller, T. Ogier, G. Exilard, and F. Nicoud. Mesh local refinement to enhance effusion cooling models. In ERCOFTAC, editor, *12th International Symposium on Engineering Turbulence Modelling and Measurements (ETMM12)*, Montpellier (France), September 2018. *4 citations pages 114, 127, 131, et 132*

- [29] R. Bizzari, D. Lahbib, A. Dauplain, F. Duchaine, L. Gicquel, and F. Nicoud. A thickened-hole model for large eddy simulations over multiperforated liners. *Flow Turbulence and Combustion*, Online First Articles:1–13, 2018. *16 citations pages [iii](#), [46](#), [48](#), [49](#), [51](#), [52](#), [63](#), [68](#), [71](#), [72](#), [82](#), [83](#), [85](#), [115](#), [131](#), et [132](#)*
- [30] R. Bizzari, D. Lahbib, A. Dauplain, F. Duchaine, S. Richard, and F. Nicoud. Low order modeling method for assessing the temperature of multi-perforated plates. *International Journal of Heat and Mass Transfer*, 127:727–742, july 2018. *8 citations pages [52](#), [90](#), [116](#), [119](#), [127](#), [128](#), [131](#), et [132](#)*
- [31] R. Bizzari, D. Lahbib, A. Dauplain, F. Duchaine, S. Richard, and F. Nicoud. A model able to assess multiperforated liner’s temperature from an unresolved adiabatic simulation. In *Journée SFT Numérique et couplage thermique*, Espace Hamelin, Paris, March 2018. SFT. *3 citations pages [90](#), [131](#), et [132](#)*
- [32] M. Boileau, G. Staffelbach, B. Cuenot, T. Poinsot, and C. Bérat. LES of an ignition sequence in a gas turbine engine. *Combust. Flame*, 154(1-2):2–22, 2008. *Cité page [11](#)*
- [33] R. Bourguet, M. Braza, G. Harran, and R. El Akoury. Anisotropic organised eddy simulation for the prediction of non-equilibrium turbulent flows around bodies. *Journal of Fluids and Structures*, 24(8):1240–1251, 2008. *Cité page [12](#)*
- [34] A. M. Briones, B. A. Rankin, S. D. Stouffer, T. J. Erdmann, and D. L. Burrus. Parallelized, automated, and predictive imprint cooling model for combustion systems. *Journal of Engineering for Gas Turbines and Power*, 139(3):031505, 2017. *3 citations pages [31](#), [32](#), et [35](#)*
- [35] P. Bruel and J. Florenciano. Report on the experimental velocity database, with acoustic forcing for multi-hole plate, deliverable D3.1.5, European program KIAI, [www.kiai-project.eu](http://www.kiai-project.eu). 2012. *Cité page [54](#)*
- [36] A. L. Brundage, M. W. Plesniak, and S. Ramadhyani. Influence of coolant feed direction and hole length on film cooling jet velocity profiles. *ASME Paper 99-GT-035*, 1999. *2 citations pages [25](#) et [26](#)*
- [37] A. Burdet, R. S. Abhari, and M. G. Rose. Modeling of Film Cooling—Part II: Model for Use in Three-Dimensional Computational Fluid Dynamics. *Journal of turbomachinery*, 129(2):221–231, 2007. *Cité page [32](#)*
- [38] A. Byerley, P. Ireland, T. Jones, and S. Ashton. Detailed heat transfer measurements near and within the entrance of a film cooling hole. In *ASME 1988 International Gas Turbine and Aeroengine Congress and Exposition*, pages V004T09A023–V004T09A023. American Society of Mechanical Engineers, 1988. *Cité page [22](#)*

- 
- [39] G. A. Callejo, E. Laroche, P. Millan, and F. Leglaye. A wall-function based model for multi-perforated walls. In *ASME Turbo Expo 2015: Turbine Technical Conference and Exposition*, pages V05BT12A002–V05BT12A002. American Society of Mechanical Engineers, 2015. *Cité page 16*
- [40] J.-L. Champion and S. Rouvreau. Plif analysis of mixing phenomena inside an effusion cooling film. *Eurotherm series*, pages 193–198, 2002. *2 citations pages 18 et 54*
- [41] A. P. Colburn. A method of correlating forced convection heat-transfer data and a comparison with fluid friction. *International Journal of Heat and Mass Transfer*, 7(12):1359–1384, 1964. *2 citations pages 39 et 40*
- [42] O. Colin, F. Ducros, D. Veynante, and T. Poinsot. A thickened flame model for large eddy simulations of turbulent premixed combustion. *Phys. Fluids*, 12(7):1843–1863, 2000. *Cité page 82*
- [43] O. Colin and M. Rudgyard. Development of high-order taylor–galerkin schemes for les. *Journal of Computational Physics*, 162(2):338–371, 2000. *Cité page 56*
- [44] L. Cortelezzi and A. R. Karagozian. On the formation of the counter-rotating vortex pair in transverse jets. *J. Fluid Mech.*, 446:347–373, 2001. *Cité page 27*
- [45] G. Cottin, E. Laroche, N. Savary, and P. Millan. Modeling of the heat flux for multi-hole cooling applications. In *ASME 2011 Turbo Expo: Turbine Technical Conference and Exposition*, pages 1955–1965. American Society of Mechanical Engineers, 2011. *8 citations pages 20, 21, 39, 40, 100, 101, 102, et 109*
- [46] M. E. Crawford, W. M. Kays, and R. J. Moffat. Full-coverage film cooling. part I: Comparison of heat transfer data for three injection angles. *J. Eng. Gas Turb. and Power*, 102:1000–1005, 1980. *Cité page 15*
- [47] M. E. Crawford, W. M. Kays, and R. J. Moffat. Full-coverage film cooling. part II: Heat transfer data and numerical simulation. *J. Eng. Gas Turb. and Power*, 102:1006–1012, 1980. *Cité page 32*
- [48] P. I. Crumpton, J. A. Mackenzie, and K. W. Morton. Cell vertex algorithms for the compressible navier-stokes equations. *J. Comput. Phys.*, 109:1–15, 1993. *Cité page 56*
- [49] R. Da Soghe, A. Andreini, B. Facchini, and L. Mazzei. Heat transfer enhancement due to coolant extraction on the cold side of effusion cooling plates. *Journal of Engineering for Gas Turbines and Power*, 137(12):122608, 2015. *Cité page 39*

- [50] G. Daviller, M. Brebion, P. Xavier, G. Staffelbach, J.-D. Müller, and T. Poinso. A mesh adaptation strategy to predict pressure losses in les of swirled flows. *Flow, Turbulence and Combustion*, 99(1):93–118, Jul 2017. *Cité page 124*
- [51] S. Deck. Numerical simulation of transonic buffet over a supercritical airfoil. *AIAA journal*, 43(7):1556–1566, 2005. *Cité page 12*
- [52] C. Dobrzynski and P. Frey. Anisotropic delaunay mesh adaptation for unsteady simulations. In *Proceedings of the 17th international Meshing Roundtable*, pages 177–194. Springer, 2008. *Cité page 115*
- [53] J. Donéa, B. Roig, and A. Huerta. High-order accurate time-stepping schemes for convection-diffusion problems. *Comput. Methods Appl. Mech. Eng.* , 182:249–275, 2000. *Cité page 91*
- [54] F. Duchaine, A. Corpron, L. Pons, V. Moureau, F. Nicoud, and T. Poinso. Development and assessment of a coupled strategy for conjugate heat transfer with large eddy simulation: Application to a cooled turbine blade. *Int. J. Heat Fluid Flow* , 30(6):1129–1141, 2009. *2 citations pages 42 et 43*
- [55] F. Duchaine, S. Jauré, D. Poitou, E. Quémerais, G. Staffelbach, T. Morel, and L. Gicquel. Analysis of high performance conjugate heat transfer with the openpalm coupler. *Computational Science & Discovery*, 8(1):015003, 2015. *2 citations pages 91 et 93*
- [56] F. Duchaine, N. Maheu, V. Moureau, G. Balarac, and S. Moreau. Large-eddy simulation and conjugate heat transfer around a low-mach turbine blade. *Journal of Turbomachinery*, 136(5):051015, 2014. *Cité page 93*
- [57] R. K. Dybvig. *The SCHEME programming language*. Mit Press, 2009. *Cité page 43*
- [58] V. L. Eriksen and R. J. Goldstein. Heat transfer and film cooling following injection through inclined circular tubes. *J. Heat Trans.* , 96:239–245, 1974. *2 citations pages 18 et 54*
- [59] M. Errera and S. Chemin. A fluid-solid thermal coupling applied to an effusion cooling system. In *34th AIAA Fluid Dynamics Conference and Exhibit*, Portland, Oregon, 2004. *Cité page 20*
- [60] J. Florenciano. *Etude de la réponse d’un écoulement avec transfert pariétal de masse à un forçage acoustique*. PhD thesis, Université de Pau, 2013. *3 citations pages 20, 21, et 52*
- [61] J.-L. Florenciano and P. Bruel. LES fluid–solid coupled calculations for the assessment of heat transfer coefficient correlations over multi-perforated walls. *Aerospace Science and Technology*, 53:61 – 73, 2016. *8 citations pages 20, 39, 40, 91, 96, 101, 109, et 116*

- 
- [62] J.-L. Florenciano and P. Bruel. Les fluid–solid coupled calculations for the assessment of heat transfer coefficient correlations over multi-perforated walls. *Aerospace Science and Technology*, 2016. *Cité page 42*
- [63] J. Fourier. *Theorie analytique de la chaleur, par M. Fourier*. Chez Firmin Didot, père et fils, 1822. *Cité page 38*
- [64] R. Fransen. *LES based aerothermal modeling of turbine blade cooling systems*. PhD thesis, CERFACS - Centre Européen de Recherche et de Formation Avancée en Calcul Scientifique, 2013. *Cité page 11*
- [65] B. Franzelli, E. Riber, M. Sanjosé, and T. Poinsot. A two-step chemical scheme for Large-Eddy Simulation of kerosene-air flames. *Combust. Flame*, 157(7):1364–1373, 2010. *Cité page 82*
- [66] V. Frayssé, L. Giraud, S. Gratton, and J. Langou. A set of GMRES routines for real and complex arithmetics on high performance computers. *ACM Trans. Math. Softw.*, 31(2):228–238, 2005. *Cité page 91*
- [67] T. F. Fric and A. Roshko. Vortical structure in the wake of a transverse jet. *J. Fluid Mech.*, 279:1–47, 1994. *4 citations pages 17, 18, 27, et 28*
- [68] J. Fröhlich and D. Von Terzi. Hybrid les/rans methods for the simulation of turbulent flows. *Progress in Aerospace Sciences*, 44(5):349–377, 2008. *Cité page 12*
- [69] S. Fu, W. Haase, S.-H. Peng, and D. Schwamborn. *Progress in Hybrid RANS-LES Modelling: Papers Contributed to the 4th Symposium on Hybrid RANS-LES Methods, Beijing, China, September 2011*, volume 117. Springer Science & Business Media, 2012. *Cité page 12*
- [70] J. W. Gibbs. *The scientific papers of J. Willard Gibbs*, volume 1. Longmans, Green and Company, 1906. *Cité page 56*
- [71] R. J. Goldstein. Film cooling. *Advances in heat transfer*, 7:321–379, 1971. *Cité page 8*
- [72] P. Grenard and D. Scherrer. A modified wall boundary condition for multi-perforated walls. *International Journal of Heat and Mass Transfer*, 67:16–24, 2013. *2 citations pages 39 et 40*
- [73] F. Grossi, M. Braza, and Y. Hoarau. Prediction of transonic buffet by delayed detached-eddy simulation. *AIAA Journal*, 52(10):2300–2312, 2014. *Cité page 12*
- [74] K. M. B. Gustafsson. *Experimental Studies of Effusion Cooling*. Phd thesis, Chalmers University of Technology. Goteborg, 2001. *3 citations pages 18, 28, et 29*

- [75] W. G. Habashi, J. Dompierre, Y. Bourgault, D. Ait-Ali-Yahia, M. Fortin, and M.-G. Vallet. Anisotropic mesh adaptation: towards user-independent, mesh-independent and solver-independent cfd. part i: general principles. *International Journal for Numerical Methods in Fluids*, 32(6):725–744, 2000. *Cité page 115*
- [76] C. A. Hale, M. W. Plesniak, and S. Ramadhyani. Film cooling effectiveness for short film cooling holes fed by a narrow plenum. *J. Turbomach.* , 122:553–557, 2000. *Cité page 15*
- [77] C. A. Hale, M. W. Plesniak, and S. Ramadhyani. Structural features and surface heat transfer associated with a row of short-hole jets in crossflow. *Int. J. Heat Fluid Flow* , 21:542–553, 2000. *Cité page 28*
- [78] J. Han, S. Dutta, and S. Ekkad. *Gas turbine heat transfer and cooling technology*. CRC Press, 2012. *Cité page 21*
- [79] M. Harnieh, M. Thomas, R. Bizzari, L. Gicquel, and F. Duchaine. Assessment of a coolant injection model on cooled high-pressure vanes in large eddy simulation - invited conference. In ERCOFTAC, editor, *12th International Symposium on Engineering Turbulence Modelling and Measurements (ETMM12)*, Montpellier, France, September 2018. *5 citations pages 81, 86, 87, 131, et 132*
- [80] M. K. Harrington, M. A. McWaters, D. G. Bogard, C. A. Lemmon, and K. A. Thole. Full-coverage film cooling with short normal injection holes. *ASME TURBOEXPO 2001. 2001-GT-0130*, 2001. *Cité page 20*
- [81] J. D. Heidmann and S. D. Hunter. Coarse grid modeling of turbine film cooling flows using volumetric source terms. In *ASME Turbo Expo 2001: Power for Land, Sea, and Air*, pages V003T01A023–V003T01A023. American Society of Mechanical Engineers, 2001. *Cité page 32*
- [82] J. C. R. Hunt, A. A. Wray, and P. Moin. Eddies, streams, and convergence zones in turbulent flows. In *Proc. of the Summer Program* , pages 193–208. Center for Turbulence Research, NASA Ames/Stanford Univ., 1988. *Cité page 23*
- [83] I. V. Iourokina and S. K. Lele. Large eddy simulation of film-cooling above the flat surface with a large plenum and short exit holes. In *44th Aerospace Sciences Meeting and Exhibit*, 2006. *2 citations pages 24 et 25*
- [84] F. Jaegle, O. Cabrit, S. Mendez, and T. Poinso. Implementation methods of wall functions in cell-vertex numerical solvers. *Flow, turbulence and combustion*, 85(2):245–272, 2010. *Cité page 48*
- [85] A. Jameson, W. Schmidt, and E. Turkel. Numerical solution of the euler equations by finite volume methods using runge-kutta time stepping schemes.

- 
- In A. p. 81-1259, editor, *14th Fluid and Plasma Dynamic Conference*, Palo Alto, 1981. *Cité page 56*
- [86] S. Jauré. *Methodology for conjugate heat transfer simulations relying on Large Eddy Simulations in massively parallel environments*. PhD thesis, Université de Toulouse, 2012. *2 citations pages 42 et 92*
- [87] S. Jauré, F. Duchaine, and L. Gicquel. Comparisons of coupling strategies for massively parallel conjugate heat transfer with large eddy simulation. In *In IV International Conference on Computational Methods for Coupled Problems in Science and Engineering*, Kos Island, Greece, 2011. *2 citations pages 42 et 93*
- [88] S. Jauré, F. Duchaine, G. Staffelbach, and L. Y. M. Gicquel. Massively parallel conjugate heat transfer methods relying on large eddy simulation applied to an aeronautical combustor. *Computational Science & Discovery*, 6(1):015008, 2013. *Cité page 93*
- [89] B. Johnson, K. Zhang, W. Tian, and H. Hu. An experimental study of film cooling effectiveness by using piv and psp techniques. In *51st AIAA Aerospace Sciences Meeting*, 2013. *Cité page 20*
- [90] B. A. Kader. Temperature and concentration profiles in fully turbulent boundary layers. *Int. J. Heat and Mass Transfer*, 24(9):1541–1544, 1981. *Cité page 39*
- [91] V. U. Kakade, S. J. Thorpe, and M. Gerendás. Effusion-cooling performance at gas turbine combustor representative flow conditions. In *ASME Turbo Expo 2012: Turbine Technical Conference and Exposition*, pages 857–869. American Society of Mechanical Engineers, 2012. *Cité page 20*
- [92] R. W. Kaszeta. *Measurements in Film Cooling Flows with Lateral Injection*. Phd thesis, University of Minnesota, 1998. *Cité page 16*
- [93] R. W. Kaszeta, T. W. Simon, R. A. Oke, and S. W. Burd. Flow measurements in film cooling flows with lateral injection. 1996. *Cité page 16*
- [94] R. M. Kelso, T. T. Lim, and A. E. Perry. An experimental study of round jets in cross-flow. *J. Fluid Mech.*, 306:111–144, 1996. *Cité page 27*
- [95] C. Koren, R. Vicquelin, and O. Gicquel. High-fidelity multiphysics simulation of a confined premixed swirling flame combining large-eddy simulation, wall heat conduction and radiative energy transfer. In *ASME Turbo Expo 2017: Turbomachinery Technical Conference and Exposition*, pages V05CT17A010–V05CT17A010. American Society of Mechanical Engineers, 2017. *Cité page 112*

- [96] C. Koupper, G. Cacioli, L. Gicquel, F. Duchaine, G. Bonneau, L. Tarchi, and B. Facchini. Development of an engine representative combustor simulator dedicated to hot streak generation. *Journal of Turbomachinery*, 136(11):111007, 2014. *Cité page 85*
- [97] C. Koupper, L. Gicquel, F. Duchaine, and G. Bonneau. Advanced combustor exit plane temperature diagnostics based on large eddy simulations. *Flow, Turbulence and Combustion*, 95(1):79–96, 2015. *Cité page 47*
- [98] L. Labarrère. *Etude théorique et numérique de la combustion à volume constant appliquée à la propulsion*. Phd thesis, Université de Toulouse - Ecole doctorale MEGeP, 3 2016. *Cité page 3*
- [99] L. Labarrère, T. Poinsot, A. Dauplain, F. Duchaine, M. Bellenoue, and B. Boust. Experimental and numerical study of cyclic variations in a constant volume combustion chamber. *Combustion and Flame*, 172(October 2016):49–61, 2016. *Cité page 3*
- [100] D. Lahbib. *Modélisation aérodynamique et thermique des multi-perforations en LES*. Phd thesis, Université de Montpellier - Ecole doctorale: Information, Structures et Systèmes (I2S), 12 2015. *7 citations pages 21, 29, 37, 47, 91, 93, et 102*
- [101] D. Lahbib, A. Dauplain, F. Duchaine, and F. Nicoud. Large eddy simulation of conjugate heat transfer around a multi-perforated plate with deviation. In *ASME Turbo Expo 2016: Turbomachinery Technical Conference and Exposition*, pages V05AT10A002–V05AT10A002. American Society of Mechanical Engineers, 2016. *4 citations pages 16, 42, 52, et 91*
- [102] B. Lakshminarayana. *Fluid dynamics and heat transfer of turbomachinery*. John Wiley & Sons, 1995. *Cité page 6*
- [103] N. Lamarque. *Schémas numériques et conditions limites pour la simulation aux grandes échelles de la combustion diphasique dans les foyers d’hélicoptère*. Phd thesis, INP Toulouse, 2007. *Cité page 56*
- [104] H. Latzko. Heat transfer in a turbulent liquid or gas stream. 1944. *Cité page 39*
- [105] P. Lax and B. Wendroff. Systems of conservation laws. *Communications on Pure and Applied mathematics*, 13(2):217–237, 1960. *Cité page 56*
- [106] P. D. Lax and B. Wendroff. Systems of conservation laws. *Commun. Pure Appl. Math.* , 13:217–237, 1960. *Cité page 82*
- [107] P. D. Lax and B. Wendroff. Difference schemes for hyperbolic equations with high order of accuracy. *Commun. Pure Appl. Math.* , 17:381–398, 1964. *Cité page 56*

- 
- [108] E. Le Grivès, J.-J. Nicolas, and J. Génot. Internal aerodynamics and heat transfer problems associated to film cooling of gas turbines. In *ASME 1979 International Gas Turbine Conference and Exhibit and Solar Energy Conference*, pages V01AT01A057–V01AT01A057. American Society of Mechanical Engineers, 1979. *Cité page 39*
- [109] P. V. LeBrocq, B. E. Launder, and C. H. Priddin. Discrete hole injection as a means of transpiration cooling; an experimental study. *Proc. Instn. Mech. Engrs.* , 187(17):149–157, 1973. *2 citations pages 6 et 15*
- [110] A. H. Lefebvre. *Gas Turbines Combustion*. Taylor & Francis, 1999. *2 citations pages 7 et 8*
- [111] B. Leger, P. Miron, and J. M. Emidio. Geometric and aero-thermal influences on multiholed plate temperature: application on combustor wall. *International Journal of Heat and Mass Transfer*, 46(7):1215–1222, 2003. *Cité page 20*
- [112] M. Lesieur, O. Métais, and P. Comte. *Large-Eddy Simulations of Turbulence*. Cambridge University Press, 2005. *Cité page 11*
- [113] J. H. Leylek and R. D. Zerkle. Discrete-jet film cooling: A comparison of computational results with experiments. *J. Turbomach.* , 116:358–368, 1994. *2 citations pages 25 et 26*
- [114] D. G. MacManus and J. A. Eaton. Flow physics of discrete boundary layer suction - measurements and predictions. *J. Fluid Mech.* , 417:47–75, 2000. *Cité page 22*
- [115] F. D. Mare, W. P. Jones, and K. Menzies. Large eddy simulation of a model gas turbine combustor. *Combust. Flame* , 137:278–295, 2004. *Cité page 11*
- [116] R. J. Margason. The path of a jet directed at large angles to a subsonic free stream. TN D-4919, NASA, 1968. *Cité page 29*
- [117] R. J. Margason. Fifty years of jet in crossflow research. In U. Winchester, editor, *Computational and Experimental Assessment of Jets in Crossflow*, volume AGARD-CP-534, pages 1–41, 1993. *Cité page 29*
- [118] M. Martiny, A. Schulz, and S. Wittig. Full-coverage film cooling investigations: adiabatic wall temperatures and flow visualization. *ASME paper*, (95-WA), 1995. *Cité page 20*
- [119] M. Martiny, A. Schulz, and S. Wittig. Mathematical model describing the coupled heat transfer in effusion cooled combustor walls. In *ASME 1997 International Gas Turbine and Aeroengine Congress and Exhibition*, pages V003T09A065–V003T09A065. American Society of Mechanical Engineers, 1997. *Cité page 39*

- [120] J. D. Mattingly. *Elements of gas turbine propulsion*, volume 1. McGraw-Hill Science, Engineering & Mathematics, 1996. *Cité page 18*
- [121] R. E. Mayle and F. J. Camarata. Multihole cooling effectiveness and heat transfer. *J. Heat Trans.* , 97:534–538, 1975. *Cité page 16*
- [122] L. Mazzei, A. Andreini, and B. Facchini. Assessment of modelling strategies for film cooling. *International Journal of Numerical Methods for Heat & Fluid Flow*, 27(5):1118–1127, 2017. *3 citations pages 33, 138, et 139*
- [123] L. Mazzei, A. Andreini, B. Facchini, and L. Bellocchi. A 3d coupled approach for the thermal design of aero-engine combustor liners. In *ASME Turbo Expo 2016: Turbomachinery Technical Conference and Exposition*, pages V05BT17A009–V05BT17A009. American Society of Mechanical Engineers, 2016. *Cité page 43*
- [124] S. Mendez. *Simulation numérique et modélisation de l'écoulement autour des parois multi-perforées - th/cfd/07/104*. PhD thesis, Université Montpellier II - DOCTORALE ISS - Spécialité Mathématiques et Modélisation, 2007. *Cité page 29*
- [125] S. Mendez and F. Nicoud. Adiabatic homogeneous model for flow around a multiperforated plate. *AIAA Journal* , 46(10):2623–2633, 2008. *21 citations pages 22, 23, 24, 25, 27, 29, 36, 43, 47, 48, 49, 63, 69, 74, 83, 85, 100, 103, 106,*
- [126] S. Mendez and F. Nicoud. Large-eddy simulation of a bi-periodic turbulent flow with effusion. *J. Fluid Mech.* , 598:27–65, 2008. *7 citations pages 20, 32, 35, 36, 47, 48, et 50*
- [127] D. E. Metzger, D. I. Takeuchi, and P. A. Kuenstler. Effectiveness and heat transfer with full-coverage film-cooling. *ASME Paper 73-GT-18*, 1973. *Cité page 15*
- [128] B. Michel, P. Gajan, A. Strzelecki, A. Kourta, and H. Boisson. Simulation numérique d'une zone d'injection pariétale pour une chambre de combustion de turbomachine. In *18ème Congrès Français de Mécanique. Grenoble, août 2007*, 2007. *2 citations pages 16 et 20*
- [129] B. Michel, P. Gajan, A. Strzelecki, N. Savary, A. Kourta, and H.-C. Boisson. Full coverage film cooling using compound angle. *Comptes Rendus Mécanique*, 337(6-7):562–572, 2009. *Cité page 70*
- [130] A. Mills. Experimental investigation of turbulent heat transfer in the entrance region of a circular conduit. *Journal of Mechanical Engineering Science*, 4(1):63–77, 1962. *Cité page 39*

- 
- [131] P. Miron. *Étude expérimentale des lois de parois et du film de refroidissement produit par une zone multiperforée sur une paroi plane*. Phd thesis, Université de Pau et des Pays de l'Adour, 2005. *Cité page 116*
- [132] P. Miron, C. Bérat, and V. Sabelnikov. Effect of blowing rate on the film cooling coverage on a multi-holed plate: application on combustor walls. In *Eighth International Conference on Heat Transfer. Lisbon, Portugal, 2004*. *3 citations pages 20, 21, et 52*
- [133] A. Most, N. Savary, and C. Bérat. Reactive flow modelling of a combustion chamber with a multiperforated liner. *AIAA Paper*, (2007-5003), 2007. *2 citations pages 20 et 47*
- [134] V. Moureau, P. Domingo, and L. Vervisch. Design of a massively parallel cfd code for complex geometries. *Comptes Rendus Mécanique*, 339(2):141–148, 2011. *Cité page 57*
- [135] V. Moureau, G. Lartigue, Y. Sommerer, C. Angelberger, O. Colin, and T. Poinsot. Numerical methods for unsteady compressible multi-component reacting flows on fixed and moving grids. *J. Comput. Phys.*, 202(2):710–736, 2005. *Cité page 56*
- [136] S. Muppidi and K. Mahesh. Study of trajectories of jets in crossflow using direct numerical simulations. *J. Fluid Mech.*, 530:81–100, 2005. *Cité page 27*
- [137] S. Muppidi and K. Mahesh. Two-dimensional model problem to explain counter-rotating vortex pair formation in a transverse jet. *Phys. Fluids*, 18(8), 2006. *Cité page 27*
- [138] S. Muppidi and K. Mahesh. Direct numerical simulation of round turbulent jets in crossflow. *J. Fluid Mech.*, 574:59–84, 2007. *Cité page 27*
- [139] T. New, T. Lim, and S. Luo. Elliptic jets in cross-flow. *Journal of fluid mechanics*, 494:119–140, 2003. *2 citations pages 27 et 28*
- [140] I. Nezu and A. Tominaga. Law of the wall lin/log diagram. *Asakura Shoten, pp.130-133*, 2000. *Cité page 14*
- [141] F. Nicoud and F. Ducros. Subgrid-scale stress modelling based on the square of the velocity gradient tensor. *Flow, turbulence and Combustion*, 62(3):183–200, 1999. *Cité page 57*
- [142] F. Nicoud, H. Toda, O. Cabrit, S. Bose, and J. Lee. Using singular values to build a subgrid-scale model for large eddy simulations. *Physics of Fluids*, 23(8):085106, 2011. *Cité page 57*
- [143] Y. V. Peet. *Film cooling from inclined cylindrical holes using Large-Eddy Simulations*. Phd thesis, Stanford University, 2006. *4 citations pages 22, 23, 26, et 28*

- [144] S. D. Peterson and M. W. Plesniak. Short-hole jet-in-crossflow velocity field and its relationship to film-cooling performance. *Exp. Fluids* , 33:889–898, 2002. *Cité page 24*
- [145] S. D. Peterson and M. W. Plesniak. Evolution of jets emanating from short holes into crossflow. *J. Fluid Mech.* , 503:57–91, 2004. *2 citations pages 24 et 28*
- [146] B. Petre. *Étude des échanges convectifs en espace confiné le long d’une paroi multiperforée*. Phd thesis, Université de Poitiers. ENSMA, 2001. *2 citations pages 17 et 19*
- [147] B. Petre, E. Dorignac, and J. J. Vullierme. Study of the influence of the number of holes rows on the convective heat transfer in the case of full coverage film cooling. *Int. J. Heat and Mass Transfer* , 2003. *2 citations pages 52 et 116*
- [148] J. Pietrzyk, D. Bogard, and M. Crawford. Effects of density ratio on the hydrodynamics of film cooling. In *ASME 1989 International Gas Turbine and Aero-engine Congress and Exposition*, pages V004T08A018–V004T08A018. American Society of Mechanical Engineers, 1989. *Cité page 22*
- [149] J. R. Pietrzyk, D. G. Bogard, and M. E. Crawford. Hydrodynamic measurements of jets in crossflow for gas turbine film cooling applications. *J. Turbomach.* , 111:139–145, 1989. *2 citations pages 16 et 22*
- [150] T. Poinso and D. Veynante. *Theoretical and Numerical Combustion*. Third Edition (www.cerfacs.fr/elearning), 2011. *3 citations pages 8, 11, et 12*
- [151] S. B. Pope. *Turbulent flows*. Cambridge University Press, 2000. *Cité page 11*
- [152] R. Poprawe, I. Kelbassa, K. Walther, M. Witty, D. Bohn, and R. Krewinkel. Optimising and manufacturing a laser-drilled cooling hole geometry for effusion-cooled multi-layer plates. *Proc. of ISROMAC-12, Paper*, (20091), 2008. *2 citations pages 8 et 71*
- [153] C. Priere, L. Gicquel, P. Kaufmann, W. Krebs, and T. Poinso. Large eddy simulation predictions of mixing enhancement for jets in cross-flows. *Journal of Turbulence*, 5(005):1–24, 2004. *2 citations pages 17 et 56*
- [154] A. Refloch, B. Courbet, A. Murrone, P. Villedieu, C. Laurent, P. Gilbank, J. Troyes, L. Tessé, G. Chaineray, J. Dargaud, E. Quémerais, and F. Vuillot. Cfd platforms and coupling - cedre software. *The Onera Journal Aerospace Lab*, (2), 2011. *2 citations pages 91 et 92*
- [155] S. Rida, R. Reynolds, S. Chakravotry, and K. Gupta. Imprinted effusion modeling and dynamic cd calculation in gas turbine combustors. *ASME*, 2012. *3 citations pages 31, 32, et 34*

- 
- [156] N. Rizk and H. Mongia. Low NOx rich-lean combustion concept application. *AIAA paper*, (91-1962), 1991. *Cité page 8*
- [157] M. C. Rochoux, S. Ricci, D. Lucor, B. Cuenot, and A. Trouvé. Towards predictive data-driven simulations of wildfire spread—part i: Reduced-cost ensemble kalman filter based on a polynomial chaos surrogate model for parameter estimation. *Natural Hazards and Earth System Sciences*, 14(11):2951–2973, 2014. *Cité page 91*
- [158] S. Rouvreau. *Etude expérimentale de la structure moyenne et instantanée d'un film produit par une zone multiperforée sur une paroi plane*. Phd thesis, ENSMA, 2001. *Cité page 30*
- [159] M. Rudgyard and T. Schönfeld. Steady and unsteady flow simulations using the hybrid flow solver avbp. *AIAA journal*, 37(11):1378–1385, 1999. *Cité page 56*
- [160] P. Sagaut. *Introduction à la simulation des grandes échelles*. Springer, mathématiques & applications edition, 1998. *Cité page 13*
- [161] P. Sagaut. *Large eddy simulation for incompressible flows*. Springer, 2002. *Cité page 11*
- [162] N. Savary, B. Michel, and P. Gajan. Validation and benefits of a homogeneous effusion cooling model for combustor rans simulations. In *47th AIAA Aerospace Sciences Meeting including The New Horizons Forum and Aerospace Exposition*, page 1377, 2009. *Cité page 36*
- [163] A. Schulz. Combustor liner cooling technology in scope of reduced pollutant formation and rising thermal efficiencies. *Annals of the New York Academy of Sciences*, 934(1):135–146, 2001. *Cité page 8*
- [164] J. J. Scrittore, K. A. Thole, and S. W. Burd. Investigation of velocity profiles for effusion cooling of a combustor liner. *J. Turbomach.* , 129:518–526, 2007. *Cité page 20*
- [165] A. K. Sinha, D. G. Bogard, and M. E. Crawford. Film-cooling effectiveness downstream of a single row of holes with variable density ratio. *J. Turbomach.* , 113:442–449, 1991. *Cité page 16*
- [166] J. Smagorinsky. General circulation experiments with the primitive equations: 1. the basic experiment. *Mon. Weather Rev.* , 91:99–164, 1963. *Cité page 82*
- [167] P. R. Spalart. Comments on the feasibility of les for wings, and on a hybrid rans/les approach. In *Proceedings of first AFOSR international conference on DNS/LES*. Greyden Press, 1997. *Cité page 12*

- [168] P. R. Spalart, S. Deck, M. L. Shur, K. D. Squires, M. K. Strelets, and A. Travin. A new version of detached-eddy simulation, resistant to ambiguous grid densities. *Theoretical and computational fluid dynamics*, 20(3):181, 2006. *Cité page 12*
- [169] B. Tartinville and C. Hirsch. Modelling of film cooling for turbine blade design. In *ASME Turbo Expo 2008: Power for Land, Sea, and Air*, pages 2219–2228. American Society of Mechanical Engineers, 2008. *Cité page 32*
- [170] M. Thomas, A. Dauplain, F. Duchaine, L. Gicquel, C. Koupper, and F. Nicoud. Comparison of heterogeneous and homogeneous coolant injection models for large eddy simulation of multiperforated liners present in a combustion simulator. In *ASME Turbo Expo 2017: Turbomachinery Technical Conference and Exposition*, pages V02BT41A038–V02BT41A038. American Society of Mechanical Engineers, 2017. *2 citations pages 84 et 85*
- [171] H. B. Toda, O. Cabrit, K. Truffin, G. Bruneaux, and F. Nicoud. Assessment of subgrid-scale models with a large-eddy simulation-dedicated experimental database: The pulsatile impinging jet in turbulent cross-flow. *Phys. Fluids* , 26(7):075108, 2014. *Cité page 56*
- [172] M. Tyagi and S. Acharya. Large eddy simulation of film cooling flow from an inclined cylindrical jet. *J. Turbomach.* , 125:734–742, 2003. *2 citations pages 27 et 29*
- [173] S. Voigt, B. Noll, and M. Aigner. Development of a macroscopic CFD model for effusion cooling applications. *ASME Paper No. GT2012-68251*, 2012. *3 citations pages 32, 33, et 41*
- [174] D. K. Walters and J. H. Leylek. A detailed analysis of film-cooling physics: Part 1- streamwise injection with cylindrical holes. *J. Turbomach.* , 122:102–112, 2000. *2 citations pages 24 et 26*
- [175] P. Wolf, G. Staffelbach, L. Gicquel, J.-D. Muller, and T. Poinso. Acoustic and large eddy simulation studies of azimuthal modes in annular combustion chambers. *Combust. Flame* , 159(11):3398–3413, Nov. 2012. *Cité page 11*
- [176] F. Zhong and G. Brown. Experimental study of multi-hole cooling for integrally-woven, ceramic matrix composite walls for gas turbine applications. *Int. J. Heat and Mass Transfer* , 52(3):971–985, 2009. *2 citations pages 20 et 22*
- [177] F. Zhong and G. L. Brown. A 3-dimensional, coupled, dns, heat transfer model and solution for multi-hole cooling. *Int. J. Heat and Mass Transfer* , 50:1328–1343, 2007. *2 citations pages 20 et 22*